ABSTRACT

This report contains information pertaining to the measurement and estimation of reflected and emitted components of the radiation balance. It includes information about reflectance and transmittance of solar radiation from and through the leaves of some grass and forb prairie species, it discusses bidirectional reflectance from a prairie canopy and describes measured and estimated fluxes of incoming and outgoing longwave and shortwave radiation.

Results of the study showed only very small differences in reflectances and transmittances for the adaxial and abaxial surfaces of grass species in the visible and infrared wavebands, but some differences in the infrared wavebands were noted for the forbs. Since leaf optical property measurements indicate that grasses are not dependent on the leaf surface, measurements could be made on either surface; for forbs it is necessary to make optical measurements on both surfaces. There were sufficient differences between optical properties among the grass species and among the forb species to necessitate making optical measurements on each species.

Reflectance from the prairie canopy changed as a function of solar and view zenith angles in the solar principal plane with definite asymmetry about nadir. Lowest reflectances were observed at or near nadir, highest reflectances were observed in the backscatter direction, especially at oblique angles.

The surface temperature of prairie canopies was found to vary by as much as 5°C depending on view zenith and azimuth position and on the solar azimuth. Temperature measurements made at a view

zenith angle of about 40° closely approximated the surface temperatures calculated from outgoing radiation measured by pyrgeometers while temperatures measured at view zenith angles of 0° and 20° were about 1.5°C warmer. Those measured at a view zenith angle of 60° were about 2°C cooler.

Aerodynamic temperature calculated from measured sensible heat fluxes ranged from 0 to 3°C higher than nadir-viewed temperatures. Further research is required to establish relationships between aerodynamic and measured surface temperatures.

Models were developed to estimate incoming and reflected shortwave radiation from data collected with a Barnes Modular Multiband Radiometer. Estimates of incoming shortwave radiation were compared to measured values and found to be within 40 Wm^{-2} in 1987 and within 10 Wm^{-2} in 1988. Albedos were estimated to within 4% (absolute) of the measured values in both 1987 and 1988. Statistical analysis revealed a large systematic error which suggests a modeling problem or a problem with the measurement of hemispheric albedo. Use of the albedo algorithm developed in this study is cautioned due to the large systematic error encountered until such time as the relatively large discrepancies between the measured and estimated values are accounted for.

Several algorithms for estimating incoming longwave radiation were evaluated and compared to actual measures of that parameter. Two of these algorithms (the Brunt model and the modified Deacon equation) produced very reasonable estimates of incoming longwave radiation on a consistent basis. Emitted longwave radiation was calculated with the Stefan-Boltzmann Law from data collected by thermal remote sensing instruments.

Net radiation was calculated using the estimated components of the shortwave radiation streams, determined from the algorithms developed in this study, and from the longwave radiation streams provided by the Brunt, modified Deacon, and the Stefan-Boltzmann models. Estimates of net radiation were compared to measured values and found to be within the measurement error of the net radiometers used in the study.
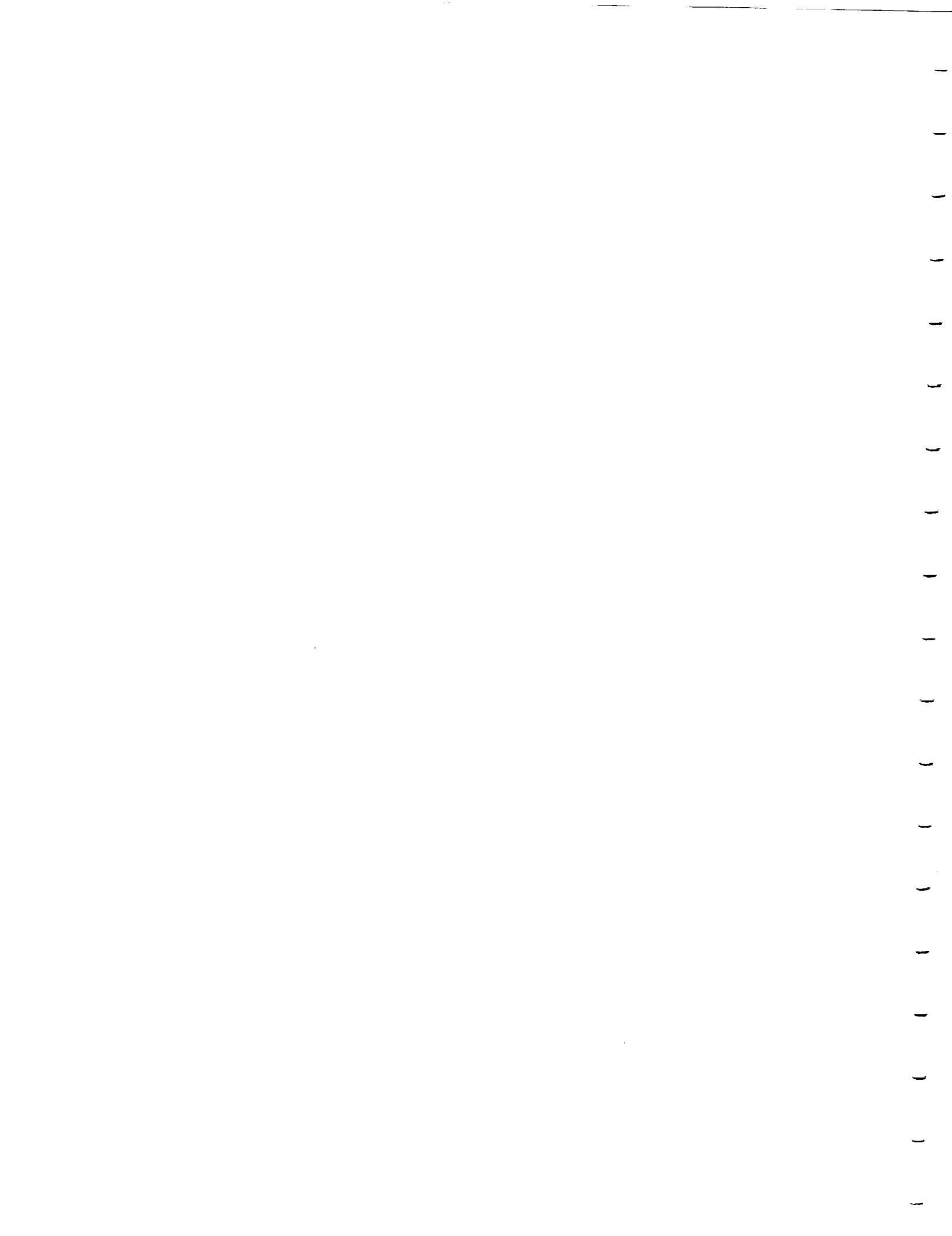
1. INTRODUCTION

The main objective of the International Land Surface Climatology Project (ISLSCP) has been stated as "the development of techniques that may be applied to satellite observations of the radiation reflected and emitted from the Earth to yield quantitative information concerning land surface climatological conditions." To accomplish this objective, a major field study called FIFE--the First ISLSCP Field Experiment--was conducted in 1987-89. Four intensive field campaigns (IFCs) were carried out in 1987 and one in 1989. We participated in all of the field campaigns and also collected additional data in 1988 as well as before, between or after some of the IFCs.

Although analysis of data collected in the 1987-1989 period will continue, this report presents findings and results obtained during the period from April 15, 1987 through May 31, 1990. The report focuses on four major areas:

1. an examination of the optical properties of leaves of some of the dominant prairie grass and forb species;

2. determination of bidirectional reflectance of the prairie canopy;

3. evaluation of canopy temperature measurements for estimating emitted longwave radiation and sensible heat flux; and

4. estimation of radiation balance components using remotely sensed data.

Other topics will be reported later as analysis of the data continues.

2. LEAF OPTICAL PROPERTIES

2.1 Introduction

Leaves are the principal units that scatter radiation in and from a vegetative canopy. Radiation incident upon a leaf may be reflected from the leaf surface, transmitted through the leaf or absorbed within the leaf. The partitioning of incident radiation into the three components is a function of the wavelengths of radiation incident upon the leaf (Gausman et al., 1970; Gausman, 1982; Maas and Dunlap, 1989), the leaf cellular structure (Gates et al., 1965; Gausman et al., 1970; Woolley, 1971), leaf coatings and roughness (Gausman, 1977; Grant et al., 1987) and morphological and physiological parameters (Gausman et al., 1971a, b; Gausman and Allen, 1973).

To model radiation reflected from canopies in the wavebands monitored by various near surface, airborne and satellite-mounted instruments, one must have knowledge of the leaf optical properties in the appropriate wavebands. Walter-Shea et al., 1989 and 1990a have reported on the optical properties of corn and soybean leaves. Walter-Shea et al., 1988 and 1990b reported that adaxial (top) and abaxial (bottom) transmittances of several grass species were almost identical, but that adaxial reflectances were slightly lower than abaxial reflectances on some species, especially in the visible wavebands. Adaxial and abaxial reflectances were generally quite different for forb species. This report will describe leaf properties of the dominant grass and forb species growing on the FIFE site in 1987, 1988 and 1989.

2.2 Material and Methods

Optical properties of individual leaves of dominant grass and forb species were measured at selected sites using the Nebraska Multiband Leaf Radiometer (NMLR) mounted with a LI-COR LI-1800-12 Integrating Sphere during IFC1 in 1987, and in 1988 and 1989. The NMLR measures in seven optical wavebands similar to those of the Barnes Model 12-1000 Modular Multiband Radiometer (MMR) (see p. 14 for bandpass limits). Details on the instrument and the methodology used in collecting and analyzing the data are given in Walter-Shea et al., 1990a. Additional leaf spectral data were collected before and during IFC4 in 1987 with a SE-590 spectro-radiometer and in 1988 with a LI-1800 spectroradiometer mounted to a LI-COR Integrating Sphere.

Leaf optical properties were collected on individual leaves of Big bluestem (Andropogon gerardii Vitman), Switchgrass (Panicum virgatum L.), Indiangrass (Sorghastrum nutans (L) Nash) and selected forb species. Reflectances and transmittances were measured from and through adaxial and abaxial leaf surfaces. During 1988 and 1989 leaf water potentials were obtained on the leaves used for the optical measurements using a Scholander-type pressure chamber.

2.3 Results and Discussion

2.3.1 Prairie Grasses

Leaf reflectances and transmittances from and through adaxial and abaxial surfaces of Big bluestem, Indiangrass and Switchgrass are shown in Fig. 2.1. These curves are characteristic of green healthy monocot leaves. Reflectances and transmittances were
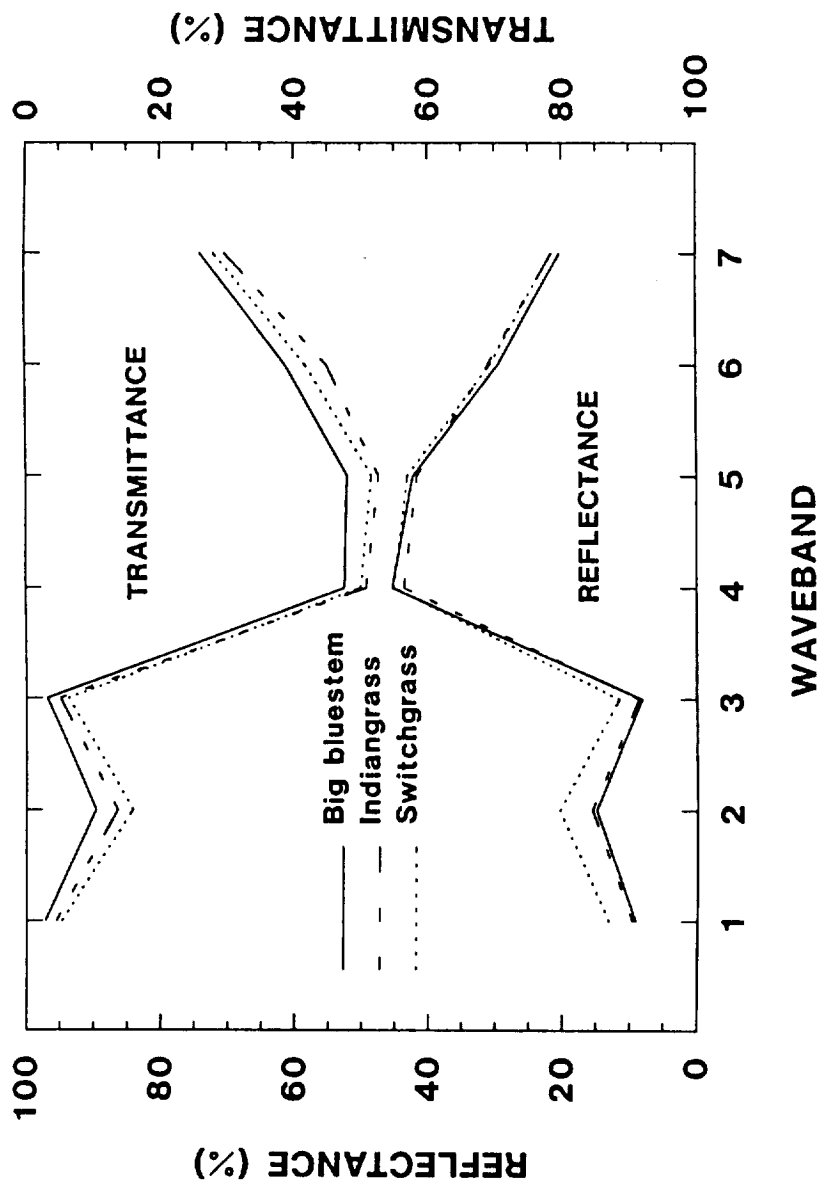
3

Fig. 2.1 Hemispherical reflectance and transmittance (in %) of the three dominant grass species: Big Bluestem (*Andropogon gerardii* Vitman), Indiangrass (*Sorghastrum nutans* (L.) Nash) and Switchgrass (*Panicum virgatum* L.). Data points are an average of four values from the morning of DOY 209 (July 28, 1989) at Site 916 as measured with the NMLR and LI-1800-12 Integrating Sphere.

4

characteristically low in the photosynthetically active radiation (PAR) wavebands with the highest reflectances and transmittances in the green region (band 2). Transmittance values are greater than reflectance values in the near and mid-IR wavebands with peak reflectances in band 4 and peak transmittances in band 5 although differences in the values between bands 4 and 5 are small. The patterns observed in 1989 were similar to those observed for recently expanded leaves in 1987 and 1988 (Fig. 2.1).

There are some small differences in reflectances from the adaxial and abaxial leaf surfaces in the visible portion of the spectrum as illustrated by data for Big bluestem (Fig. 2.2) and for Indiangrass (Fig. 2.3). There was essentially no difference in the transmittance values between the top and bottom of leaves of either grass in the visible wavebands nor for the IR wavebands of the Big bluestem leaves. However, a small, but distinct difference between transmittances through the two surfaces was observed for the Indiangrass leaf in the IR waveband. Reflectances from adaxial or abaxial leaf surfaces of both species were almost identical in the IR wavebands. Data for the healthy grass leaves obtained in 1987, 1988 and 1989 showed similar patterns to those given by the two examples. The results suggest that a transmittance measurement on either side of the leaf should be adequate and that differences are probably small enough to permit measurement of leaf optical properties from only one leaf surface. Differences between reflectance and transmittance values are sufficiently great that both measurements must be made. There is also sufficient difference between values for the different grass species that spectral curves are needed for each species.
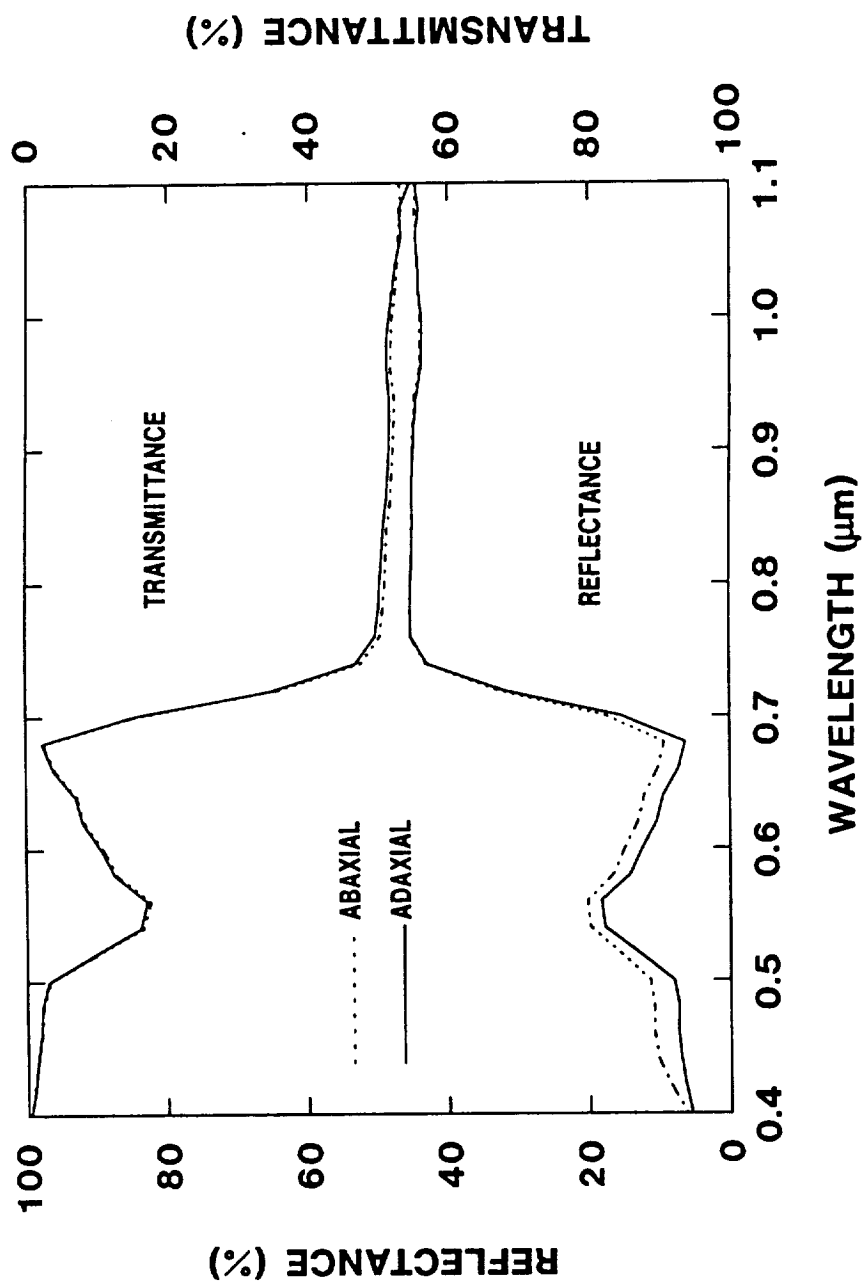
Fig. 2.2 Average abaxial and adaxial spectral hemispherical reflectance and transmittance (in %) of two individual Big bluestem leaves as measured with the LI-1800 Portable Spectroradiometer and LI-1800-12 Integrating Sphere on DOY 153 (June 2, 1988) at Site 16.
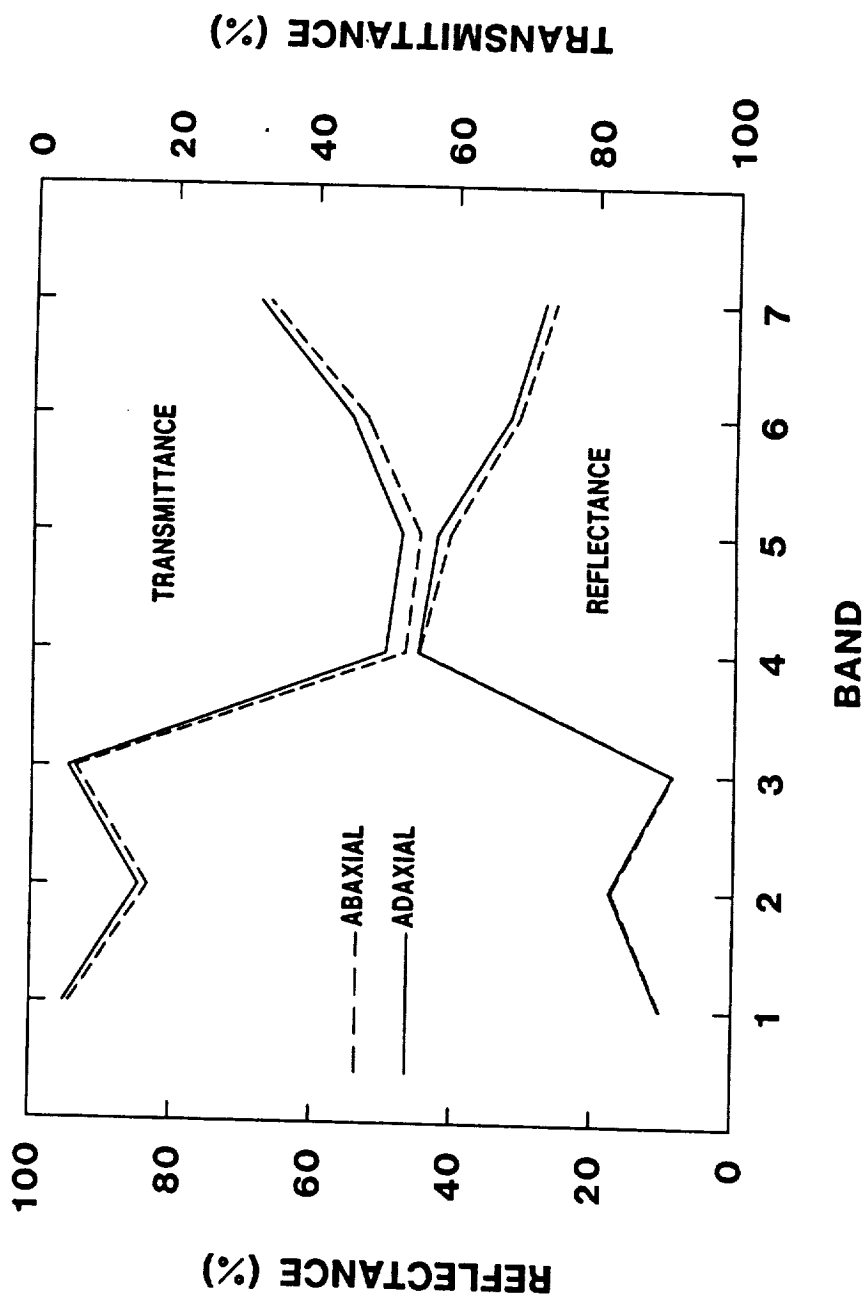
Fig. 2.3 Hemispherical reflectance and transmittance (in %) from the adaxial and abaxial surfaces of an Indiangrass leaf measured with the NMLR on DOY 163 (June 12, 1987) at Site 16.

Leaf optical properties of leaves on the same Switchgrass plant varied with leaf position, an indication of leaf age (Fig. 2.4). Visible reflectance and transmittance decreased with leaf age which represents an increase in visible absorptance as leaves age. The yellow leaf (included for comparison) indicates that the absorptance by a senescing leaf will eventually decrease. Near- and mid-IR reflectance increases with age while the IR transmittance decreases indicating little change in absorptance. Changes in NIR properties are attributed to changes in leaf cellular structure.

Measurements made over a range of leaf water potentials indicate that optical properties in the visible (band 3), near-IR (band 4) nor mid-IR (band 6) wavebands varied little over the range of -0.5 through -3.0 MPa at site 16 during the 1988 and 1989 experimental periods (Fig. 2.5). We believe that values will change at lower leaf water potentials but research to document that supposition is needed.

2.3.2 Prairie Forbs

Reflectance and transmittances from adaxial and abaxial surfaces of Leadplant (Amorpha canescens (Nutt Pursch) and Western Ragweed (Ambrosia psilostachya DC) are shown in Fig. 2.6. Reflectances and transmittances are similar from both sides of the leaves in the visible wavebands for both forb species, but there are notable differences in the magnitudes in the IR wavebands for Western Ragweed. Differences are small for the Leadplant. The patterns of the two species also differ. Maximum reflection from Leadplant leaves occurred in band 4 and the maximum transmittance
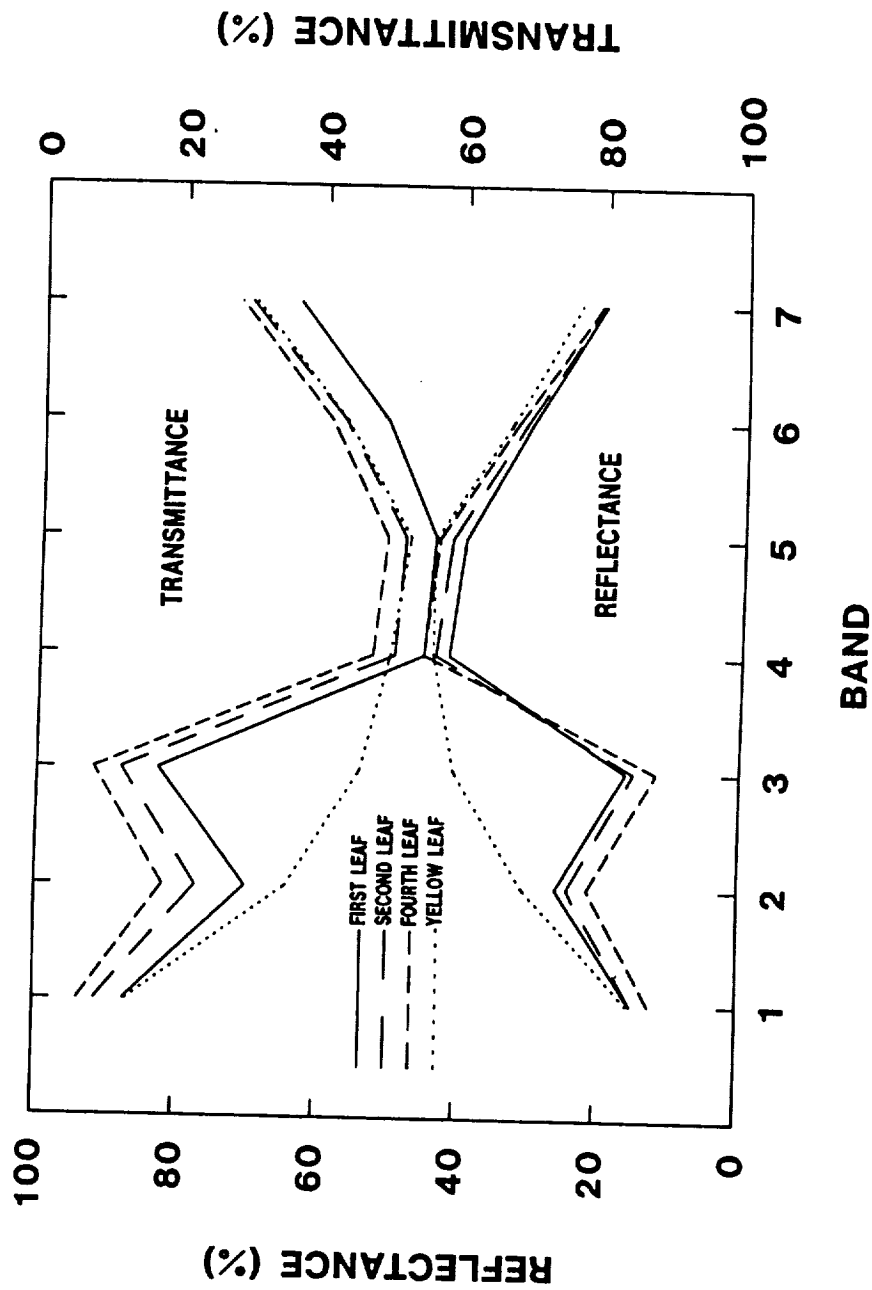
8

Fig. 2.4 Hemispherical reflectance and transmittance (in %) from adaxial Switchgrass leaf surfaces at nodes 1, 2 and 4 from the top of the plant. The optical properties from a yellow Switchgrass leaf is included for comparison. Measurements were made with the NMLR on DOY 224 (August 11, 1988).
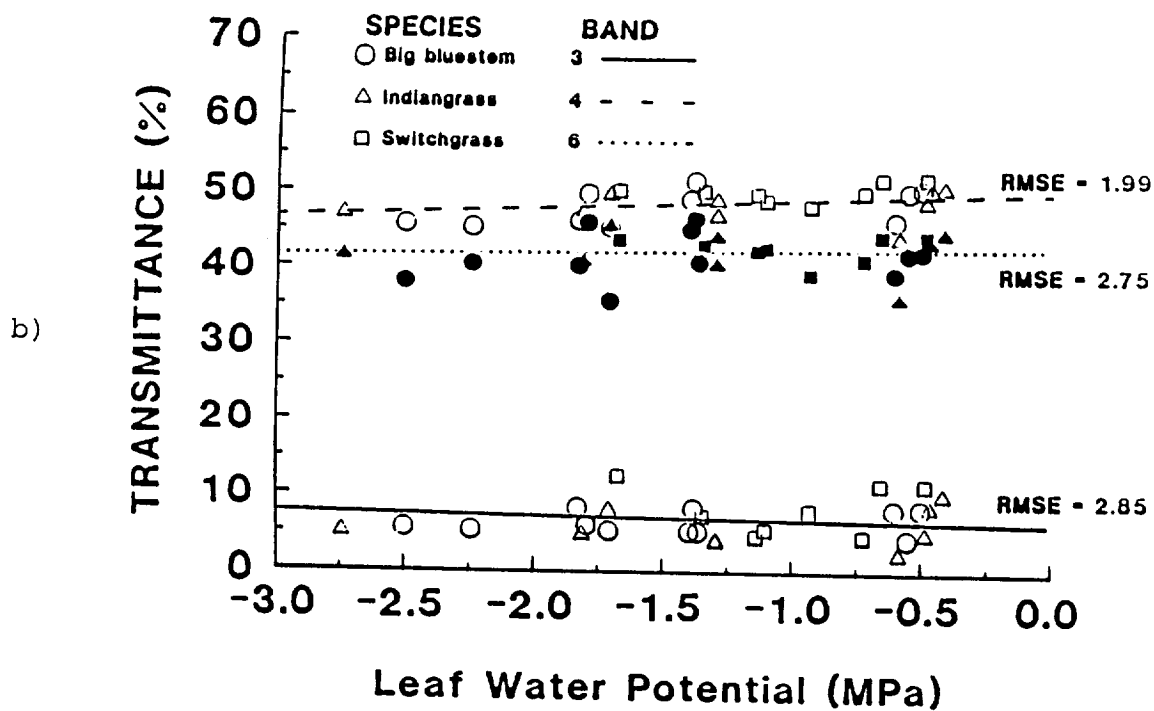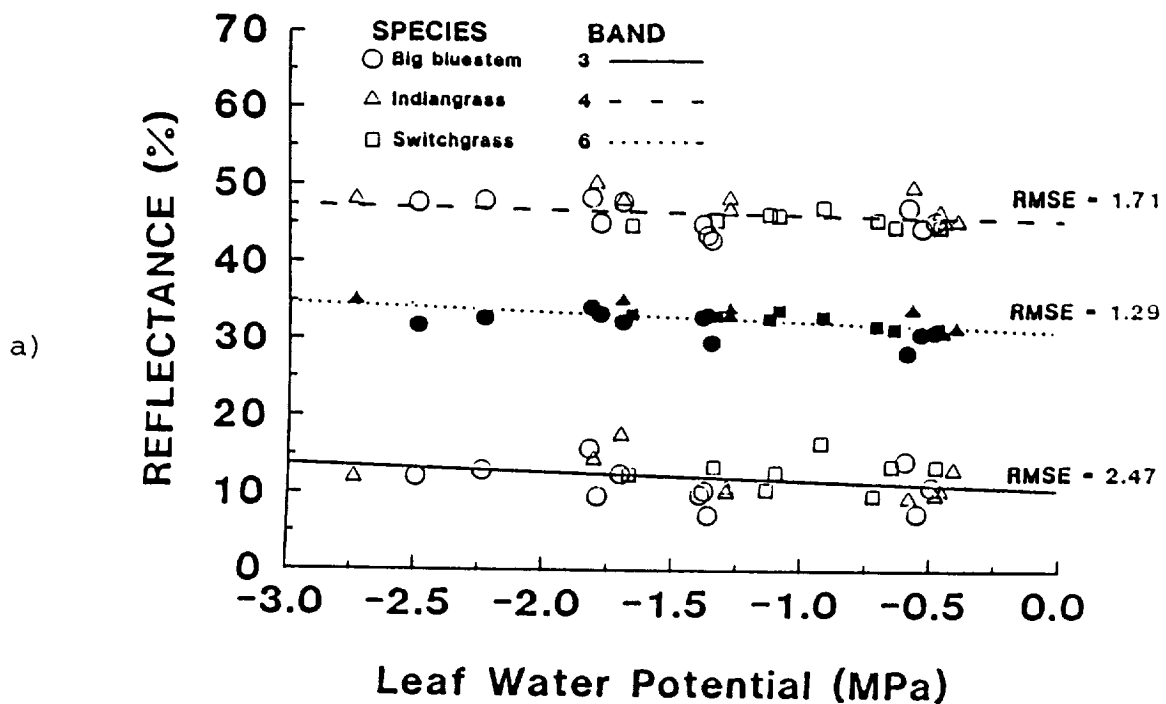
9

a)

b)

Fig. 2.5 Hemispherical reflectance and transmittance (in %) of individual leaves of Big Bluestem, Indiangrass, and Switchgrass for band 3 (0.63-0.69 µm), band 4 (0.76-0.90 µm) and band 6 (1.55-1.75 µm) of the NMLR as a function of leaf water potential for 1988 (a,b) and 1989 (c,d).
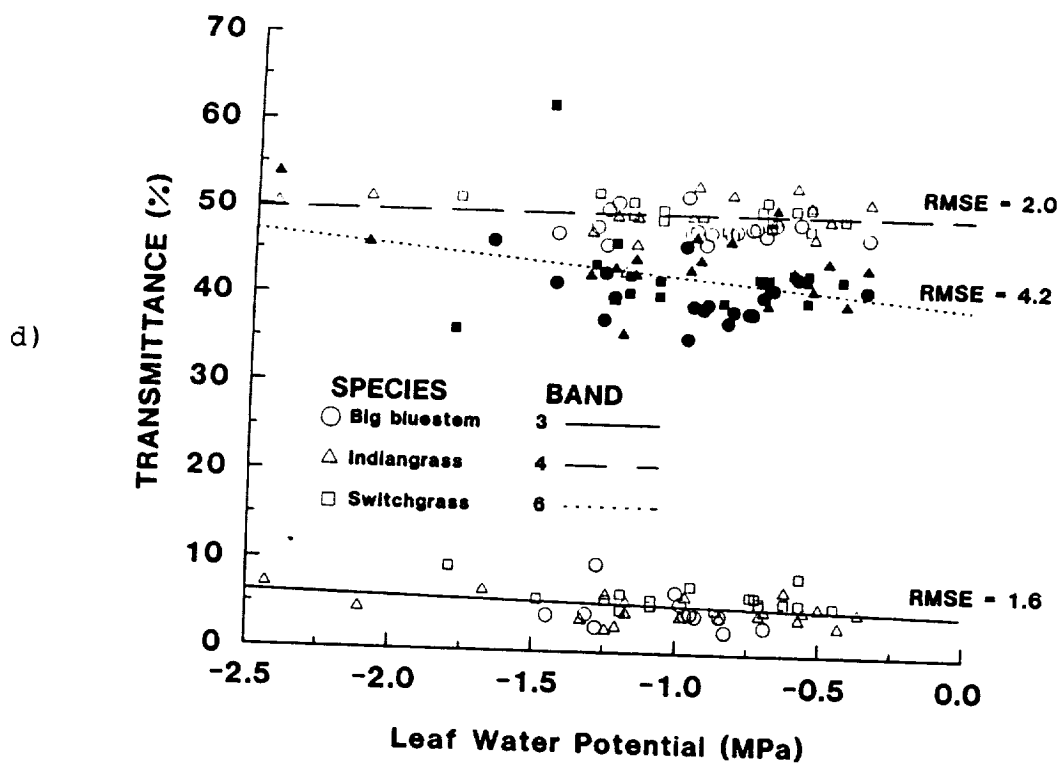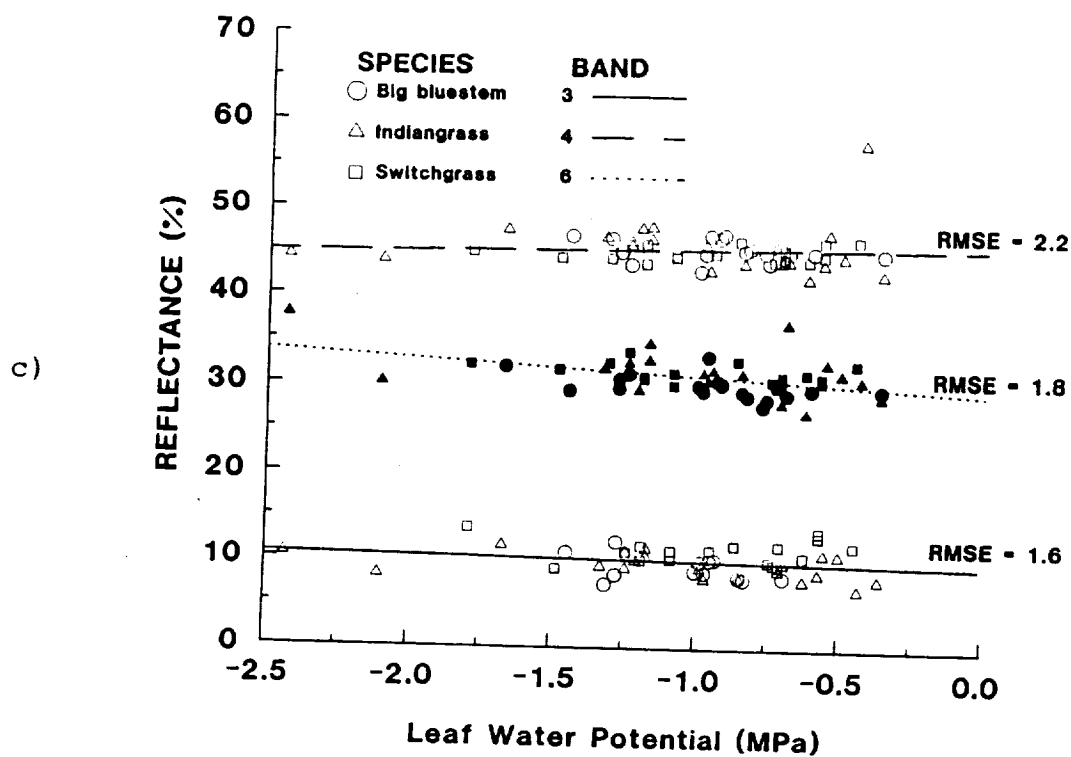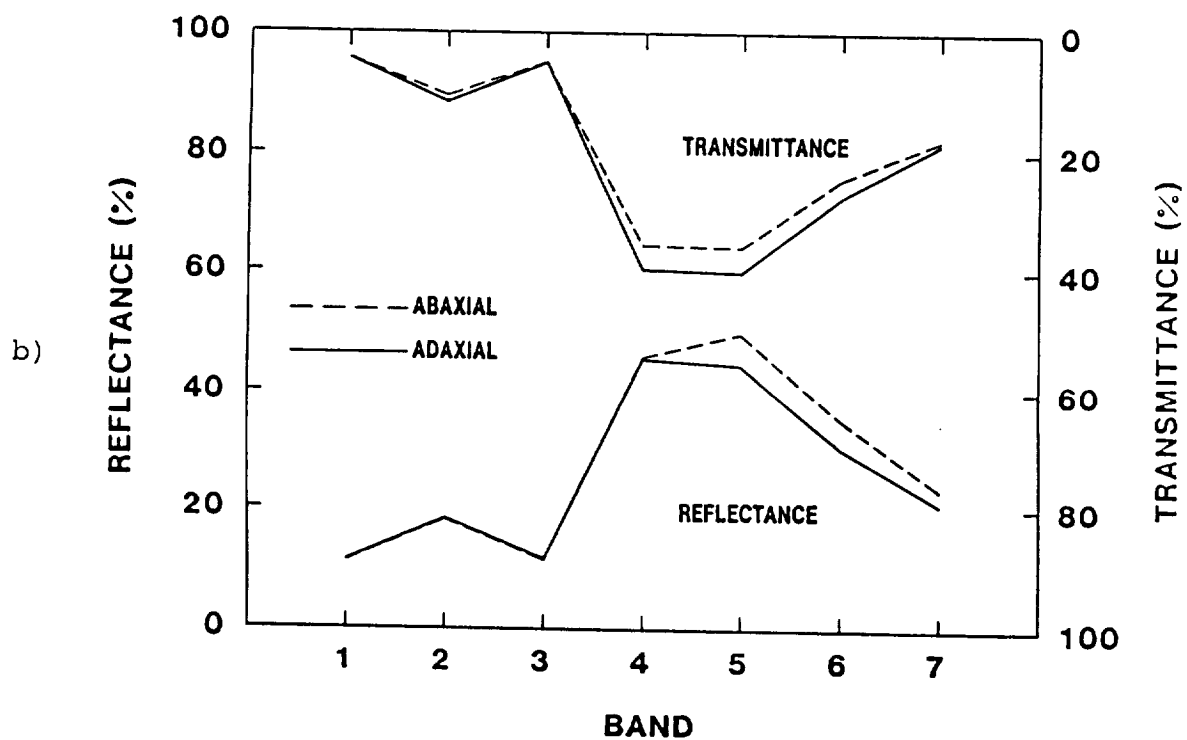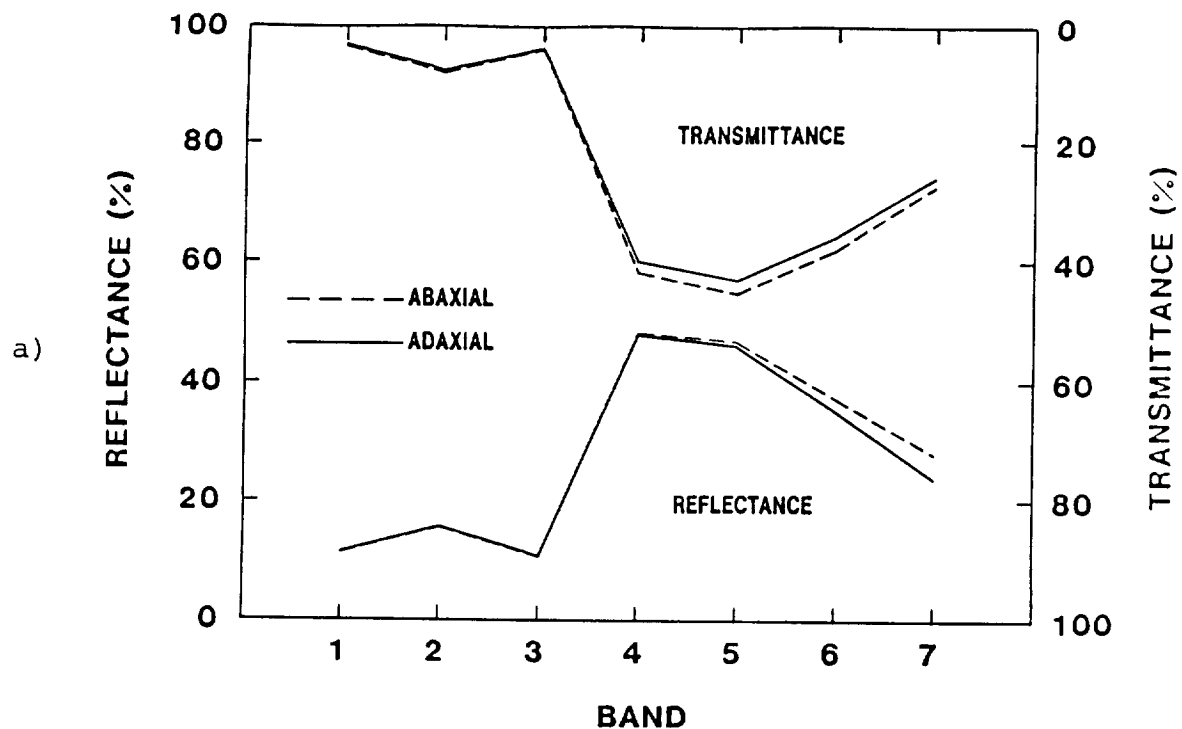
c)

d)

Fig. 2.5 continued.

Fig. 2.6 Hemispherical reflectance and transmittance (in %) from adaxial and abaxial leaf surfaces of Leadplant (a) and Western Ragweed (b) as measured with the NMLR on DOY 224 (August 11, 1988).

in band 5. For Western Ragweed the maximum reflection occurred in band 4 for the top surface, but in band 5 for the bottom surface. The magnitudes of the transmittances were almost identical for bands 4 and 5 for Western Ragweed. For both species, reflectances were greater than transmittances in the visible and IR portions of the spectrum. These differ from the patterns observed for grasses where transmittances were higher than reflectances in the IR part of the spectrum.

The data collected for the forb species suggest that measurements should be made on both adaxial and abaxial for some forb leaf surfaces. Also, because of the observed differences between species, it is necessary to measure each species.

2.4 Summary and Conclusions

Reflectances and transmittance of prairie grasses and forbs were characteristic of green healthy leaves. There were only very small differences in reflectances and essentially no difference in transmittance between the adaxial and abaxial surfaces of the grass species in the visible and IR wavebands, but relatively larger differences were observed for some forb species in the IR wavebands. For grass leaves differences in leaf optical properties do not appear to be dependent on leaf surface, but for some forb species reflectance and transmittance measurements should be made on both leaf surfaces. There is sufficient difference in optical properties among the grass species and among the forb species to necessitate making optical properties measurements on each species.

The range of leaf water potentials over which we made leaf optical measurements did not indicate any major influence of lower

leaf water potential on leaf optical properties. We believe, however, that changes in optical properties will occur at lower water potentials than experienced in this study. We recommend that research be conducted to investigate the dependency of leaf optical properties on leaf water potential or other water stress indicators.

3. CANOPY REFLECTANCE

3.1 Introduction

Vegetative surfaces are known to exhibit anisotropy (Salomonson and Marlatt, 1971; Kriebel, 1978; Kimes, 1983). In order to make accurate estimates of surface albedo, it is necessary to have knowledge of the characteristics of the surface bidirectional reflectance (Middleton, et al., 1987; Diner et al., 1989). There is, therefore, a great need to characterize the reflectance of radiation from vegetative surfaces as a function of solar and sensor viewing angles, spectral wavelengths and biophysical characteristics of the surface. Walter-Shea et al. (1990b) and Deering and Middleton (1990) have reported on some of the bidirectional reflectance characteristics of prairie canopies at the FIFE site. This report will focus on bidirectional reflectance results obtained at various FIFE sites in 1987-1989.

3.2 Materials and Methods

A good discussion of approaches to making bidirectional reflectance measurements is given by Deering (1989). Canopy reflectances were measured with a Barnes model 12-1000 Modular Multiband Radiometer (MMR) in 1987, 1988 and 1989. The MMR measures reflected shortwave radiation in the following wavebands: 0.45-0.52 μm, 0.52-0.60 μm, 0.63-0.69 μm, 0.76-0.90 μm, 1.15-1.30 μm, 1.55-1.75 μm, and 2.08-2.35 μm and emitted radiation in the 10.4-12.5 μm waveband. A LI-COR LI-1800 Spectroradiometer was used in addition to the MMR in 1988, while a Spectron Engineering SE590 Spectroradiometer was used in 1989. Both spectroradiometers measure the spectral region from 0.40 μm to 1.10 μm. The LI-1800

Spectroradiometer sampling interval was set at 10 nm while that for the SE590 Spectroradiometer was approximately 3 nm. The instruments were mounted on a portable mast which maintained the instruments 3.1 m from the soil surface. All radiometers were set with a 15° field-of-view (FOV). Measurements over vegetative plots usually were made in the solar principal plane from seven different view zenith angles: nadir and 20°, 35°, and 50° either side of nadir. Occasionally, measurements were aligned in the azimuthal plane perpendicular to the solar principal plane and in the SPOT satellite azimuthal plane. In 1989, measurements were also made over bare soil plots.

Data were collected primarily from eight sites near selected super automated meteorological stations (AMS) or flux stations (sites 5, 8, 18, 26, 28, 32, 40, and 42) in 1987. Special slope studies were conducted at sites 5 and 42. Data were collected from eight to eleven different plots surrounding the AMS or flux stations. Incident radiation was estimated from measurements made with the MMR over a painted barium sulfate ($BaSO_4$) panel approximately every 30 minutes. The majority of the canopy reflectance data was collected to coincide with a satellite overpass and with concurrent coverage by the C-130 and the NASA helicopter.

In 1988 diurnal spectral data were collected at FIFE site 16 over four plots with the MMR and the LI-1800 on May 27 (Day of Year 148), July 13 (DOY 195) and August 11 (DOY 224) using the same techniques employed in 1987. Incoming radiation were obtained over a molded Labsphere Halon 1.3 by 1.3 m panel instead of the $BaSO_4$ panel.

In 1989 canopy reflectances were measured at five vegetative plots and one bare soil plot on a diurnal basis at FIFE sites 906 and 916 in conjunction with other Surface Radiation and Biology scientific teams and aircraft and satellite overpasses. The bare soil plots were covered with a removable plastic mulch in an attempt to maintain soil moisture conditions as under a vegetative cover. The mulch was removed on the day of measurement.

The fraction of diurnal absorbed photosynthetically active radiation (APAR) was measured using a LI-COR 196-SA Line Quantum Sensor for each vegetative plot on the same days as canopy reflectance measurements. Soil moisture, pre-dawn and daytime leaf water potential and plant phytomass and LAI data were taken on selected days in 1988 and 1989.

3.3 Results and Discussion

3.3.1 Canopy Bidirectional Reflectance

Bidirectional reflectance increased with increasing view zenith angle. The highest reflectance occurred at oblique view angles in the backscatter direction. The lowest visible reflectance occurred in the forward scatter direction and in the NIR at nadir or 20° off-nadir (Figs. 3.1 and 3.2). Nadir-viewed reflectance varied slightly as a function of solar zenith angle; visible and mid-IR reflectances increased and NIR reflectance varied as a function of solar zenith angle. Variations in nadir-viewed canopy reflectance can be attributed to the changing proportion of shaded area in the total target area. The least amount of shaded material in a nadir-viewed surface (both vegetation and substrate) occurs at solar noon when a minimum

17

Fig. 3.1 3-d surface fit to MMR solar principal plane canopy bidirectional reflectance factors (in %). Data are presented as a function of view zenith angle and time of day (GMT) for days 148 (May 28) and 224 (August 12) in 1988 for wavebands a) 3 (0.63-0.69 μm), b) 4 (0.76-0.90 μm) and c) 6 (1.55-1.75 μm).
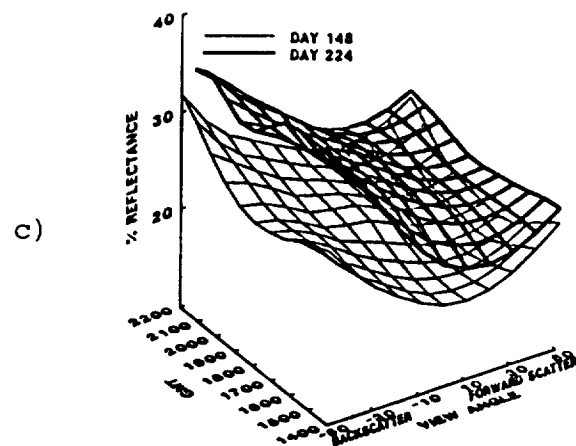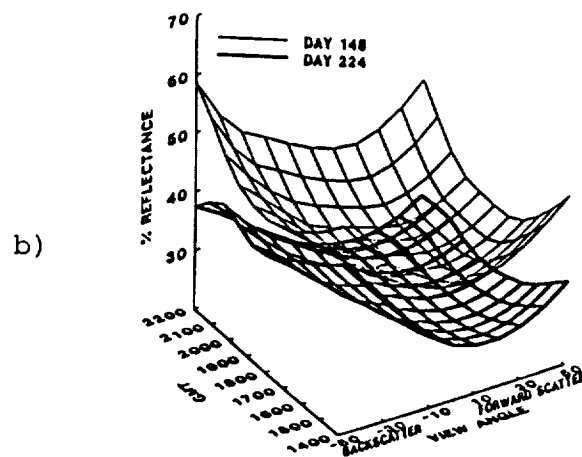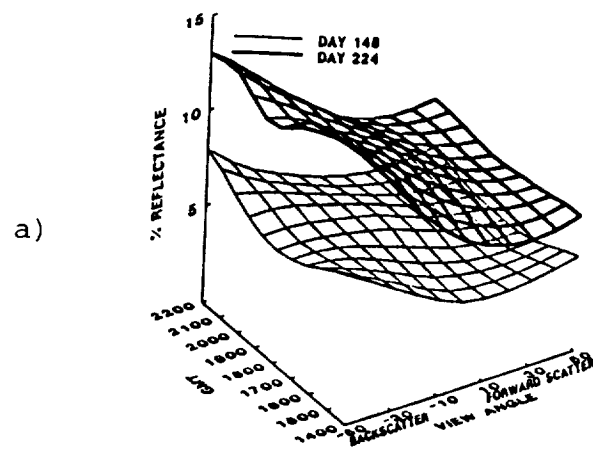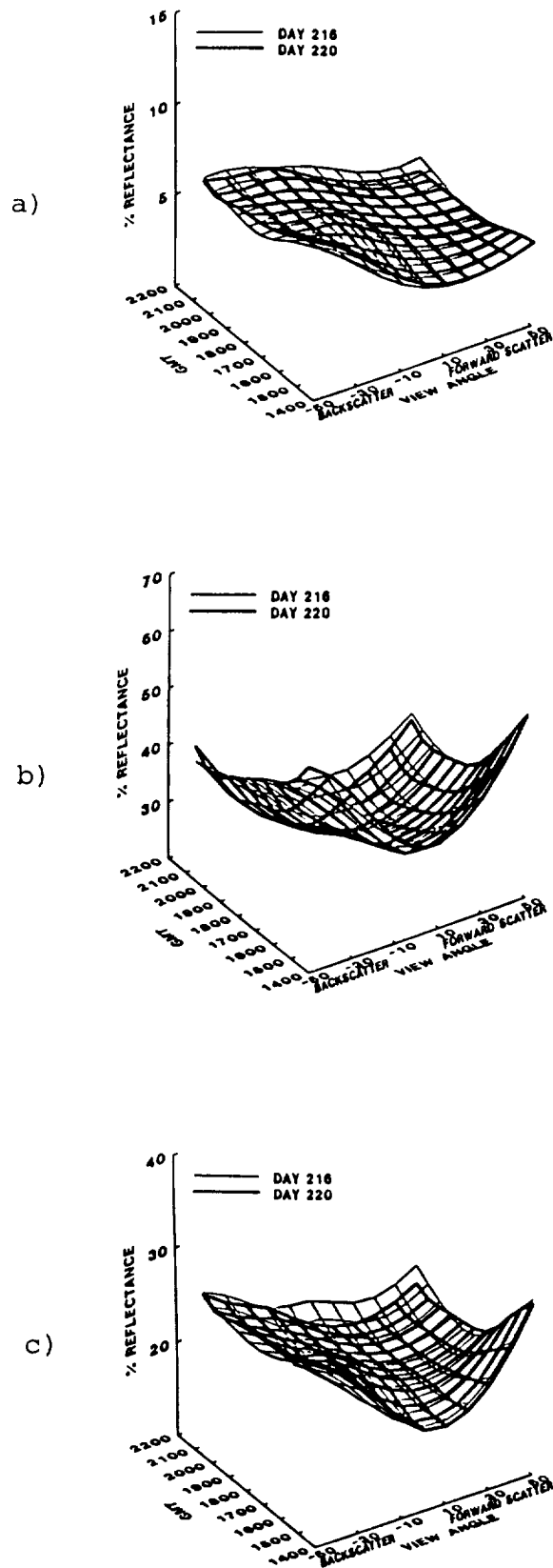
Fig. 3.2   3-d surface fit to MMR solar principal plane canopy
bidirectional reflectance factors (in %).   Data are presented
as a function of view zenith angle and time of day (GMT) for
days 216 (August 4) and 220 (August 8) in 1989 for wavebands
a) 3 (0.63-0.69 µm), b) 4 (0.76-0.90 µm) and c) 6 (1.55-1.75 µm).

shadow is cast from the vegetative components. The shading effect is more pronounced in the visible spectral region than in the NIR region. Multiple scattering of NIR by leaves decreases the contrast between sunlit and shaded areas within the canopy. The contribution of sunlit portions of vegetation, leaf litter and soil changes with time. Since the reflectance properties of soil and vegetative surfaces differ (Fig. 3.3), the resulting signal from the canopy changes with time.

Severe water stress was experienced at Site 16 in 1988 early in the growing season (Fig. 3.4a). Water available to plants was approximately 25% for 20 days (DOY 160 through 180) and at times close to that at the wilting point. Changing stress conditions undoubtedly affected the diurnal reflectance throughout the experiment. Visible and mid-IR reflectance (bands 3 and 6, respectively) increased as the brown vegetative component increased while NIR decreased (Fig. 3.1).

Drying soil conditions were observed in 1989 (Fig. 3.4b), however, conditions under which reflectance data were taken indicated the short duration of stress had little effect on the diurnal reflectance magnitude and pattern (Fig. 3.2).

3.3.2 Azimuthal Plane Perpendicular to the Solar Principal Plane

Canopy reflectance measurements were made in the solar principal plane and the azimuthal plane perpendicular to the solar principal plane at Site 16 near solar noon with an approximate 16° solar zenith angle (Fig. 3.5). There were subtle differences in average reflectances between azimuthal planes but these
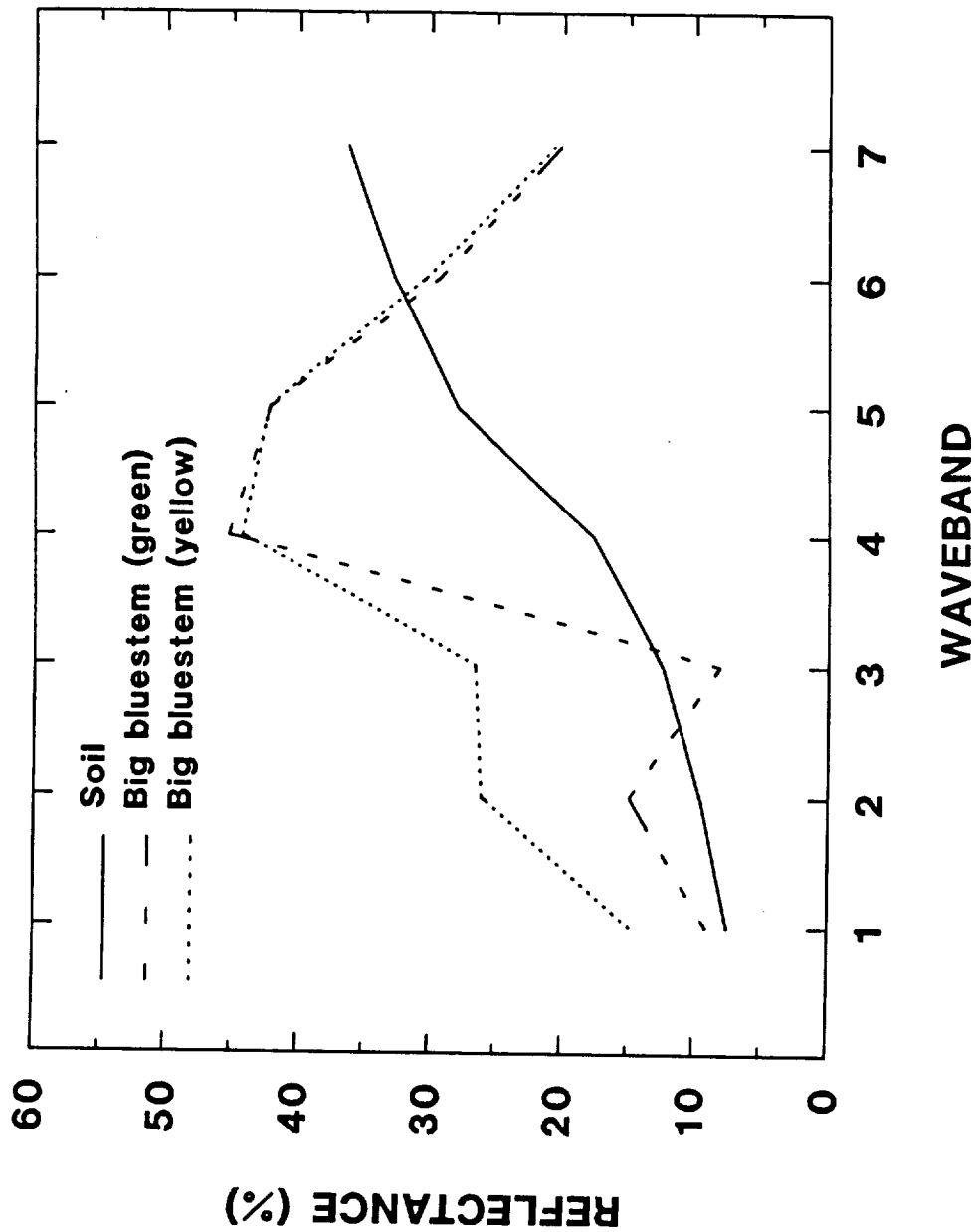
Fig. 3.3 Comparison among reflective properties of prairie vegetative canopy components: soil, green healthy Big Bluestem leaf and yellowing Big Bluestem leaf. Soil reflectance was measured with a nadir-looking MMR at approximately solar noon. Leaf reflectances were measured with the NMLR and LI-1800-12 Integrating Sphere.
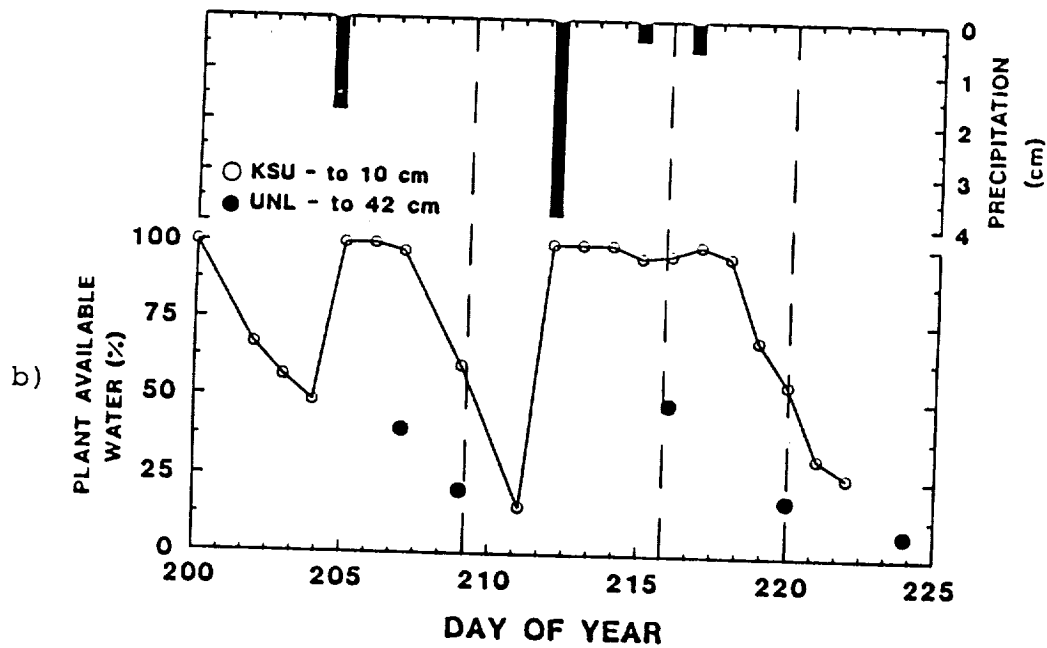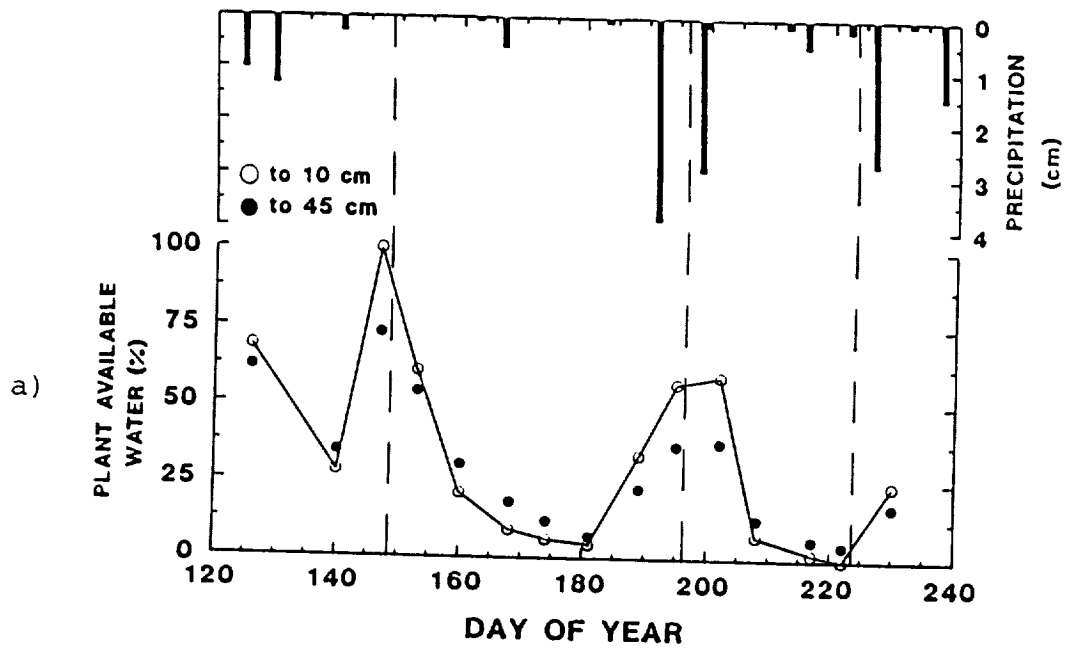
Fig. 3.4 Precipitation and estimated plant available water at Site 16 over the experimental periods in a) 1988 and b) 1989. Vertical dashed lines indicate days on which canopy reflectances were measured.

OFF-NADIR VIEW ZENITH ANGLE

REFLECTANCE FACTOR (%)

Fig. 3.5 Comparison between mean bidirectional reflectance values measurements aligned in the solar principal plane and in the azimuthal plane perpendicular to the solar principal plane at Site 16 on DOY 177 (June 26, 1987). Average solar zenith angle for the time of measurements is 15.8°. Relative azimuth of 0 is the solar azimuth. Azimuths of 0 and 180° represent backscattering and forward scattering, respectively. - and + off-nadir view zenith angles represent sensor orientation in 0 or 90° azimuthal direction and 180 or 270° azimuthal direction, respectively. Error bars represent $\pm$ 1 standard deviation.

differences, except in the NIR backscatter direction, lie within one standard deviation. The trend in the data is for the solar principal plane backscatter reflectance to be greater than that reflected at similar view angles in the azimuthal plane perpendicular to the solar principal plane. The trend is also for the solar principal plane forward scatter to be less than that reflected at similar view angles in the azimuthal plane perpendicular to the solar principal plane. The lower reflectance values in the backscatter direction at 20° is due to shadowing by the radiometer. The relatively high reflectance values at -20° in the solar principal plane is attributed to the high reflectance from the unshaded "hot spot" area in the sensor's FOV.

3.3.3 Azimuthal Plane of the SPOT Satellite

Trends described above are more obvious in comparing measurements aligned in the solar principal plane to those measured in the azimuthal plane of SPOT (Fig. 3.6). Data were taken near solar noon with an approximate 28° solar zenith angle. The lower sun angle (thus more shadows) may account for the greater difference between azimuthal planes observed with these data than was described for Fig. 3.5. Note the radiometer shadow effect occurs at the 30° backscatter direction which is in the vicinity of the hot spot for this particular day and time.

3.3.4 Soil Bidirectional Reflectance

In contrast to the diurnal canopy bidirectional reflectance results (Fig. 3.2), soil reflectance measured in 1989 differed between DOY 216 and 220 (Fig. 3.7). Soil moisture measurements

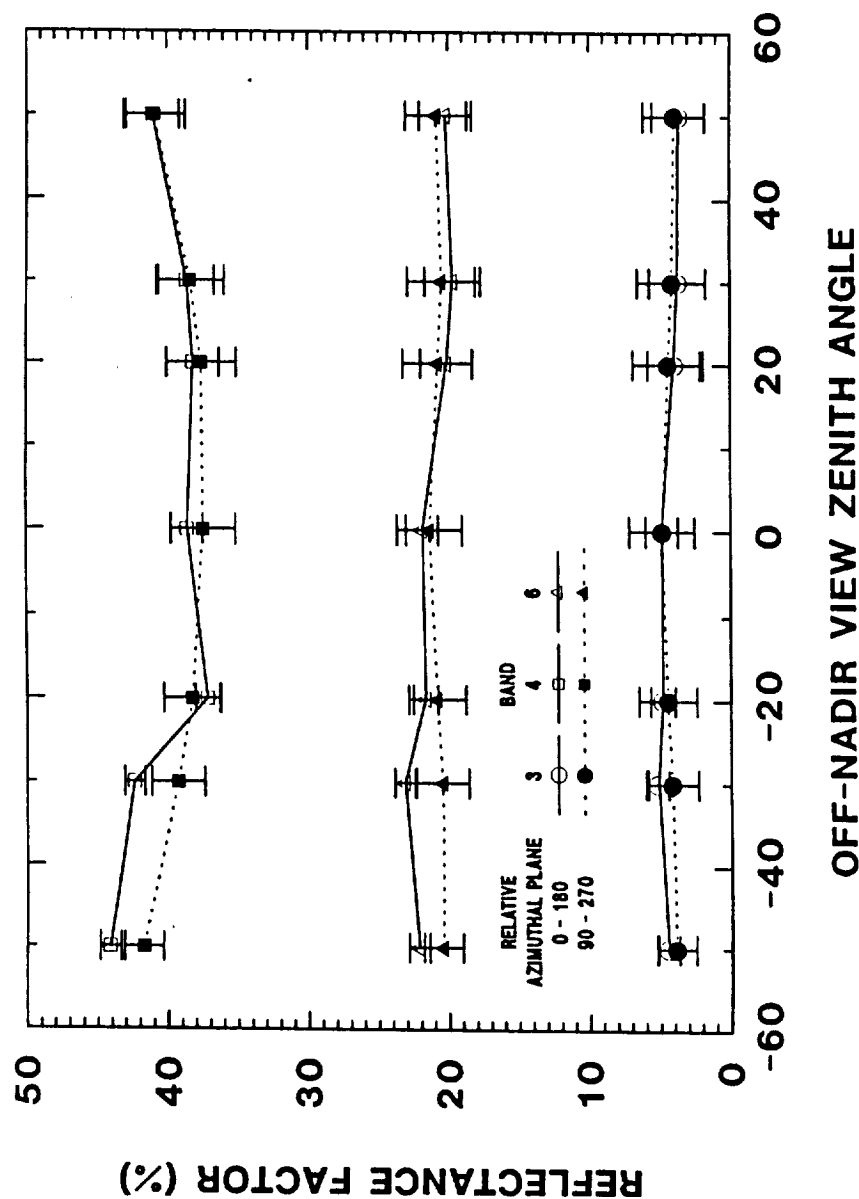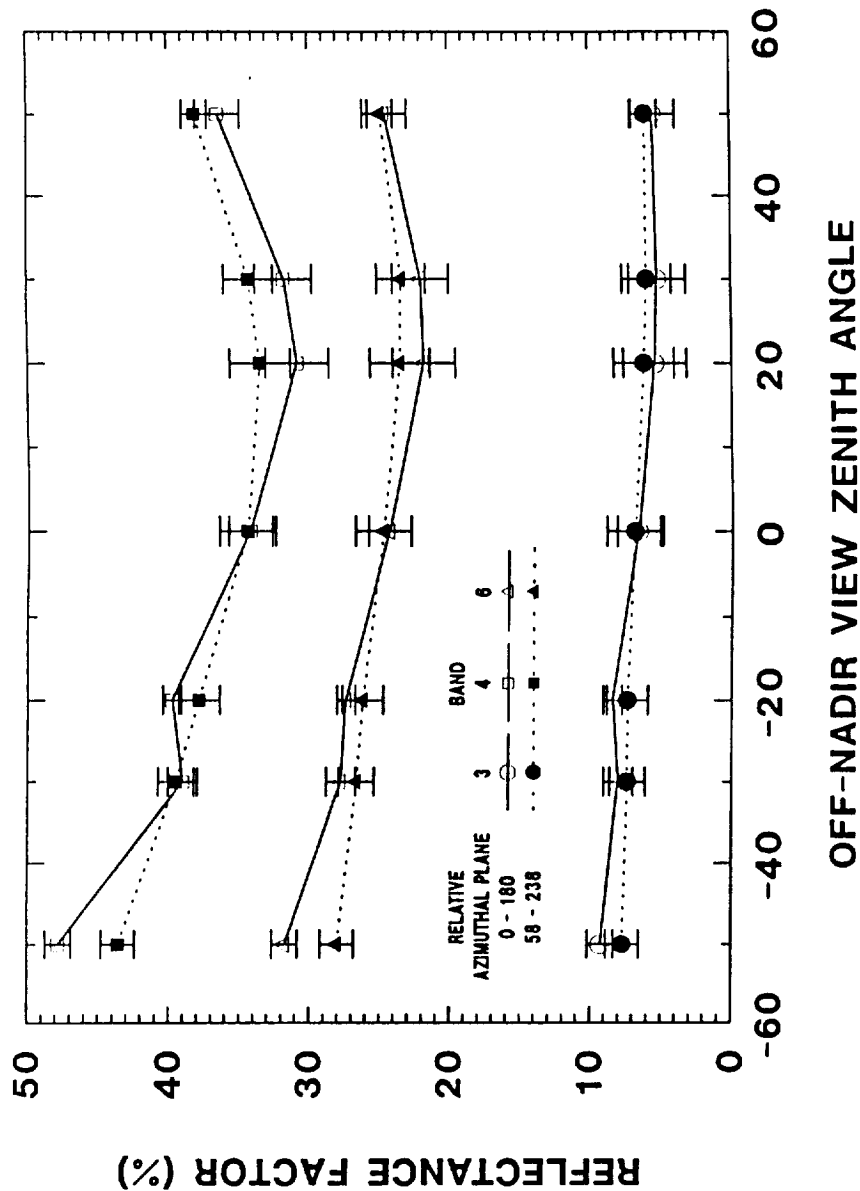Fig. 3.6 Comparison between mean bidirectional reflectance values measurements aligned in the solar principal plane and in the SPOT azimuthal plane at Site 16 on DOY 229 (August 17, 1987). Average solar zenith angle for the time of measurements is 28°. Relative azimuth of 0 is the solar azimuth. Azimuths of 0 and 180° represent back-scattering and forward scattering, respectively. – and + off-nadir view zenith angles represent sensor orientation in 0 or 58° azimuthal direction and 180 or 238° azimuthal direction, respectively. Error bars represent ± 1 standard deviation.
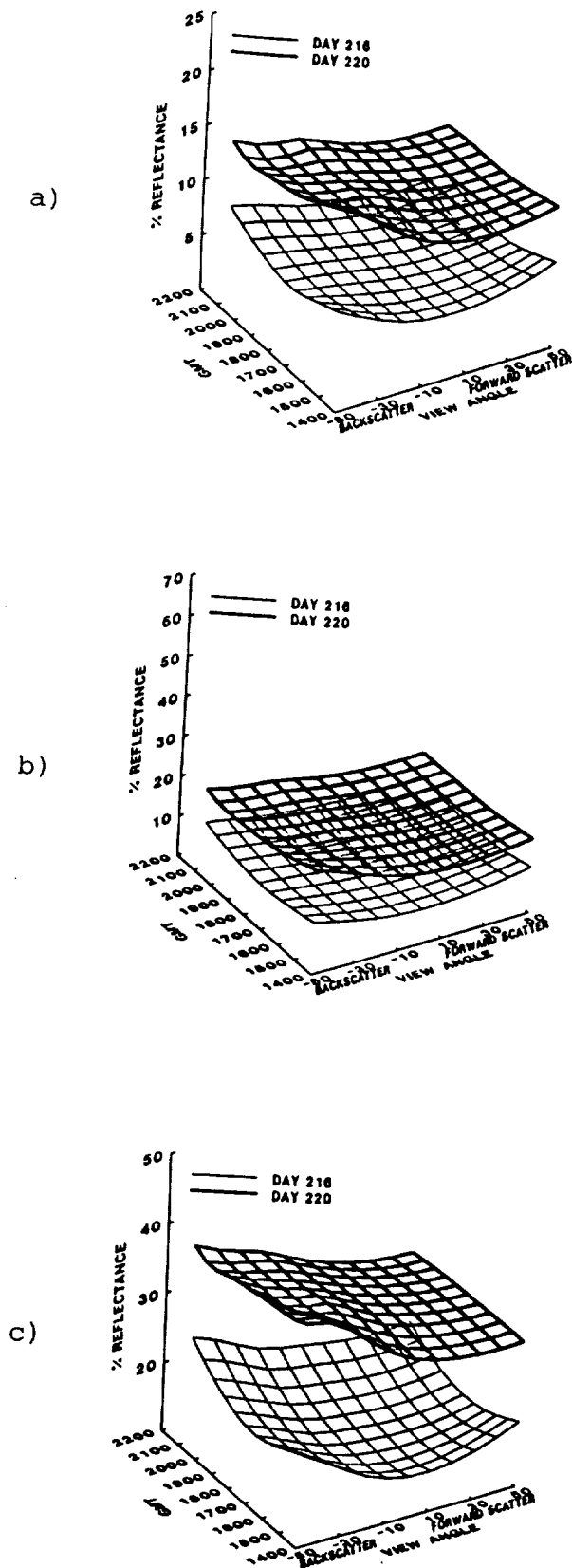
Fig. 3.7 3-d surface fit to MMR solar principal plane bare soil bidirectional reflectance factors (in %). Data are presented as a function of view zenith angle and time of day (GMT) for days 216 (August 4) and 220 (August 8) in 1989 for wavebands a) 3 (0.63-0.69 μm), b) 4 (0.76-0.90 μm) and c) 6 (1.55-1.75 μm).

from vegetative and soil plots indicate that soil moisture decreased in that time. There was a greater decrease in soil moisture in the vegetative plots (attributed to soil moisture consumption by plant transpiration) (Table 3.1). Photographs of the plot indicate that the soil surface dried, changing in tone from dark to light. This surface drying was manifested in the reflectance measurements. Reflectance increased in all wavebands. The diurnal and bidirectional variation from the soil was not as great as for the vegetative plots, probably due to the relatively smooth soil surface as compared to the rough vegetative surface.

Table 3.1. Volumetric soil moisture in the top 15 cm of soil as measured with the IRAMS Soil Moisture Meter.

	Volumetric Soil Moisture (%)	
Day	Canopy	Bare Soil
216	29.7	33.5
220	18.4	26.5

3.3.5 Absorbed Photosynthetically Active Radiation

The fraction of absorbed PAR (APAR) varied as a function of solar zenith angle (Fig. 3.8). The fraction of APAR increased with increasing solar zenith angle. The standard deviation bars indicate the variability of APAR within Site 916.

3.4 Summary and Conclusions

The largest variation in reflectance as a function of solar and view zenith angles in the principal plane was observed at large solar zenith angles for all wavebands. There was a definite asymmetry about nadir for all wavebands. The lowest reflectance

27
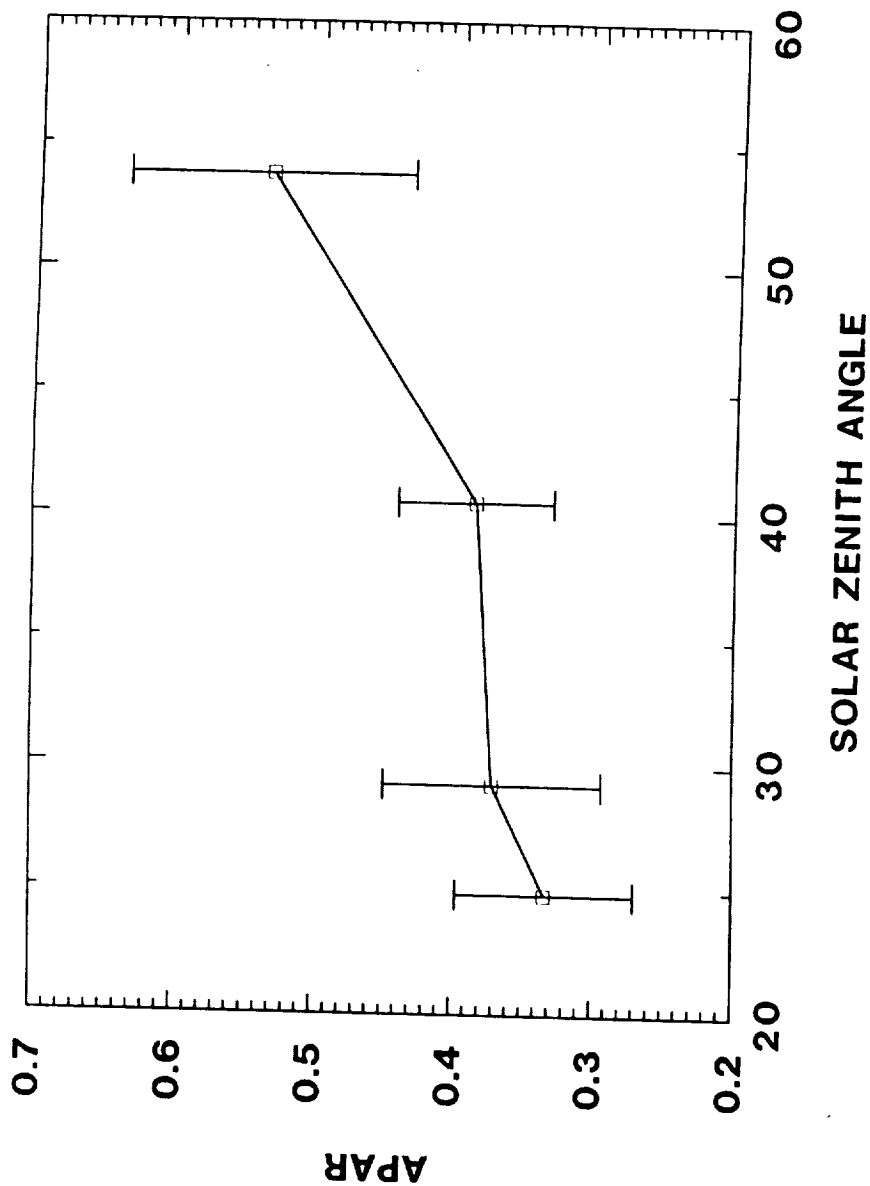
Fig. 3.8 Fraction of absorbed photosynthetically active radiation using a LI-COR Line Quantum Sensor for DOY 209 (July 28, 1989) at Site 916 as a function of solar zenith angle. Average LAI for the site is 1.4. The bars indicate $\pm$ 1 standard deviation from an average of 4 to 5 plots for which data were acquired.

28

was observed at or near nadir in the forward scatter direction. The highest reflectance value was observed in the backscatter direction at oblique angles. Reflectance generally decreased with decreasing view angles in both forward and backscatter directions. An exception occurred in the visible forward scatter direction where the minimum was at oblique off-nadir angles.

There is need for additional research on bidirectional reflectance, particularly in obtaining data with high spectral resolution instruments. Development of relationships between bidirectional reflectance and vegetative indices and APAR/IPAR relationships is also required.

4. SURFACE TEMPERATURE MEASUREMENTS FOR ESTIMATING EMITTED RADIATION AND SENSIBLE HEAT FLUX

4.1 Introduction

Previous researchers have investigated the variation of canopy temperatures at varying view angles and changing solar position. Fuchs et al. (1967) found that temperatures of crops with continuous uniform canopies were not related to view and solar angles, while surface temperatures of bare, smoothed soil did not vary with view angle. In uneven cover, such as that found with row crops, the sunlit side of the row was found to be 1-3°C higher than the shaded side of the row. Later research done by Kimes et al. (1980) over a wheat canopy, found that the radiant temperature measured by a thermal infrared sensor varied by as much as 13°C with changing view angles.

Researchers have attributed variation in canopy temperature to vegetation canopy geometry, the vertical distribution of the temperature of canopy components, and to the view angle of the sensor. Huband and Monteith (1986), studied canopy temperature variation of wheat as a function of view zenith angle in the solar principal plane. They compared off-nadir measured surface temperatures to those measured at nadir and found that canopy temperatures were as much as 1°C higher than and up to 0.9°C lower than the nadir-viewed temperatures when viewing the sunlit and shaded portion of the wheat canopy, respectively.

Hall et al., 1989 showed that the radiometric temperature varied as a function of view angle over prairie vegetation at the FIFE site. They suggested that there is a difference between the radiometric temperature viewed from nadir and the aerodynamic

30

temperature used to calculate sensible heat flux in the air. They concluded that the canopy temperature should be near the aerodynamic temperature while the nadir-viewed radiometric temperature which includes both canopy and soil background radiation would be higher than the aerodynamic temperature.

As part of the FIFE/Surface Radiance and Biology group, we have made measurements of surface canopy temperatures over prairie grassland vegetation using remote sensing methods. We have remotely measured off-nadir apparent surface temperatures with three goals in mind: 1) evaluation of the variation in remotely sensed surface temperatures with changes in the instrument view azimuth and zenith angles and with changing solar position; 2) comparison of off-nadir sensed surface temperatures with radiative temperatures calculated from outgoing longwave radiation measurements made with an inverted pyrgeometer to determine appropriate viewing angles for calculating emitted longwave radiation; and 3) comparison of off-nadir sensed surface temperatures to aerodynamic temperatures calculated from sensible heat flux data to help establish appropriate procedures for measuring canopy temperatures needed to estimate sensible heat flux from a surface.

4.2 Materials and Methods

To remotely measure apparent surface temperatures at different view angles, a mast was devised on which were mounted four Everest 4000 Temperature Transducer-Multiplexer infrared thermometers (IRTs). The IRTs were calibrated before and after the field experiment in controlled ambient conditions with a blackbody source

of varying output temperature. The transducers were mounted at view zenith angles of 0, 20, 40, and 60°. The arm on which the transducers were mounted was hinged to a support frame so that it could swing through a full 360° azimuth arc. This apparatus allowed for measurement of surface temperature at four view zenith angles and at selected view azimuth angles. We used azimuth angles that were multiples of 45°. An entire set of measurements could be made in less than five minutes. All data were recorded on Omnidata Polycorders and later transferred to microcomputers for analysis. Data were collected during periods when clouds did not obscure the sun to eliminate fluctuating surface temperatures. Surface temperatures were measured on several days in 1989 at sites 916, 906 and at a slope site near site 906.

To measure outgoing longwave radiation, an Eppley PIR pyrgeometer was inverted over the canopy at a height of about 1 meter. This allowed outgoing longwave measurements to be taken simultaneously with the surface temperature measurements. The measured outgoing longwave radiation was converted to surface temperatures using the Stefan-Boltzmann Law

$$E = \sigma T^4 . \qquad (4.1)$$

To emulate the pyrgeometer measurements, a composite (IRT) temperature was obtained by integrating the temperatures from all view angles using a numerical approximation of the equation

$$\int_{0}^{2\pi} \int_{0}^{\frac{\pi}{2}} T(\theta, \phi) \cos\theta \, \sin\theta \, d\theta \, d\phi \, , \qquad (4.2)$$

where $T(\theta, \phi)$ is the surface temperature observed at specific view zenith (θ) and view azimuth (ϕ) angles.

Another goal of this study was to compare the apparent surface temperatures measured at different view zenith angles to those calculated from the outgoing longwave data measured by the pyrgeometer. The average differences between the pyrgeometer and IRT measured temperatures were calculated for each view zenith angle (over all view azimuth angles).

A third portion of this study focused on the estimation of sensible heat flux (H) from remotely sensed surface temperature and meteorological data. Sensible heat flux can be calculated using the equation

$$H = \rho_a \, C_p \, \frac{T_a - T_s}{r_a} \qquad (4.3)$$

where ρ_a is air density, C_p is specific heat of air, T_a is air temperature, T_s is surface temperature, and r_a is aerodynamic resistance to heat flow.

To calculate r_a, the following model was used:

$$r_a = \frac{\ln\left[(z-d)/z_o\right]}{k \, u_*} - \frac{\ln(z_o/z_h)}{k \, u_*} \qquad (4.4)$$

33

where z is the height of windspeed measurement, d is the zero plane displacement, z_o is the roughness height for momentum transfer, z_h is the roughness height for heat transfer, k is von Karman's constant (0.04) and u_* is the friction velocity.

The friction velocity u_* was estimated by

$$u_* = \frac{u_z \, \ln(z/z_o)}{k} \qquad (4.5)$$

where u_z is the windspeed at height z. The equations used to estimate d, z_o and z_h in meters were derived from relationships given by Huband and Monteith (1986) and Choudhury et al. (1986):

$$d = 2/3 \, h \qquad (4.6)$$

$$z_o = h/8 \qquad (4.7)$$

$$z_h = z_o/7 \qquad (4.8)$$

where h is the canopy height in meters.

Sensible heat flux values from one-half hour eddy correlation measurements taken at the FIFE site were used in Eq. (4.3). With air temperature, air pressure, windspeed and canopy height included in the model, T_s, the surface temperature, was calculated using Eqs. (4.3) to (4.8). These aerodynamic surface temperatures (calculated from sensible heat flux data) were compared to the multiangle surface temperature values measured with the IRTs.

4.3 Results and Discussion

Variations in apparent surface temperatures with changing view angles at 0902 solar time on DOY 218 (August 6, 1989) are shown in Fig. 4.1. The view azimuth angle indicates the azimuthal direction the infrared thermometers were facing when the measurements were taken. The dashed vertical line indicates the positioning of the sun at the observer's back. For instance, at 0902 solar time, the solar azimuth was 107° (north is 0°). Therefore, the sun was at the observer's back when the observer was facing 287°, that is in a westerly (270°) to northwesterly (315°) direction. The viewed temperatures were highest for each off-nadir view zenith angle at the azimuth view angle of 315°, i.e., on the sunlit side of the canopy. The lowest temperatures occurred at the view azimuth of 135°, i.e., on the shaded side. This pattern repeated itself near solar noon and mid-afternoon (Figs. 4.2 and 4.3), that is, the warmest part of the canopy was that facing the sun and the coolest part was that on the opposite side.

The temperatures tended to decrease with increasing view zenith angle: that is, the 0° and 20° view zenith angles measured the highest temperatures, followed by the 40° and 60° angles, respectively. When viewing the sunlit portion of the canopy, the surface temperature at the view zenith angle of 20° was about 1°K higher than at the nadir position. Since the sunlit side of the canopy had a higher radiation load than the shaded side, it was not surprising that surface temperatures were higher on the sunlit side of the vegetation. At low view zenith angles, the IRTs view a combination of vegetation and soil, while at higher view zenith

35

Fig. 4.1 Dependence of apparent surface temperature on view zenith and view azimuth angles and solar position. Day 218 (6 August 1989) 0902 Solar Time. Vertical dashed line represents azimuth observer faced with sun at the observer's back.
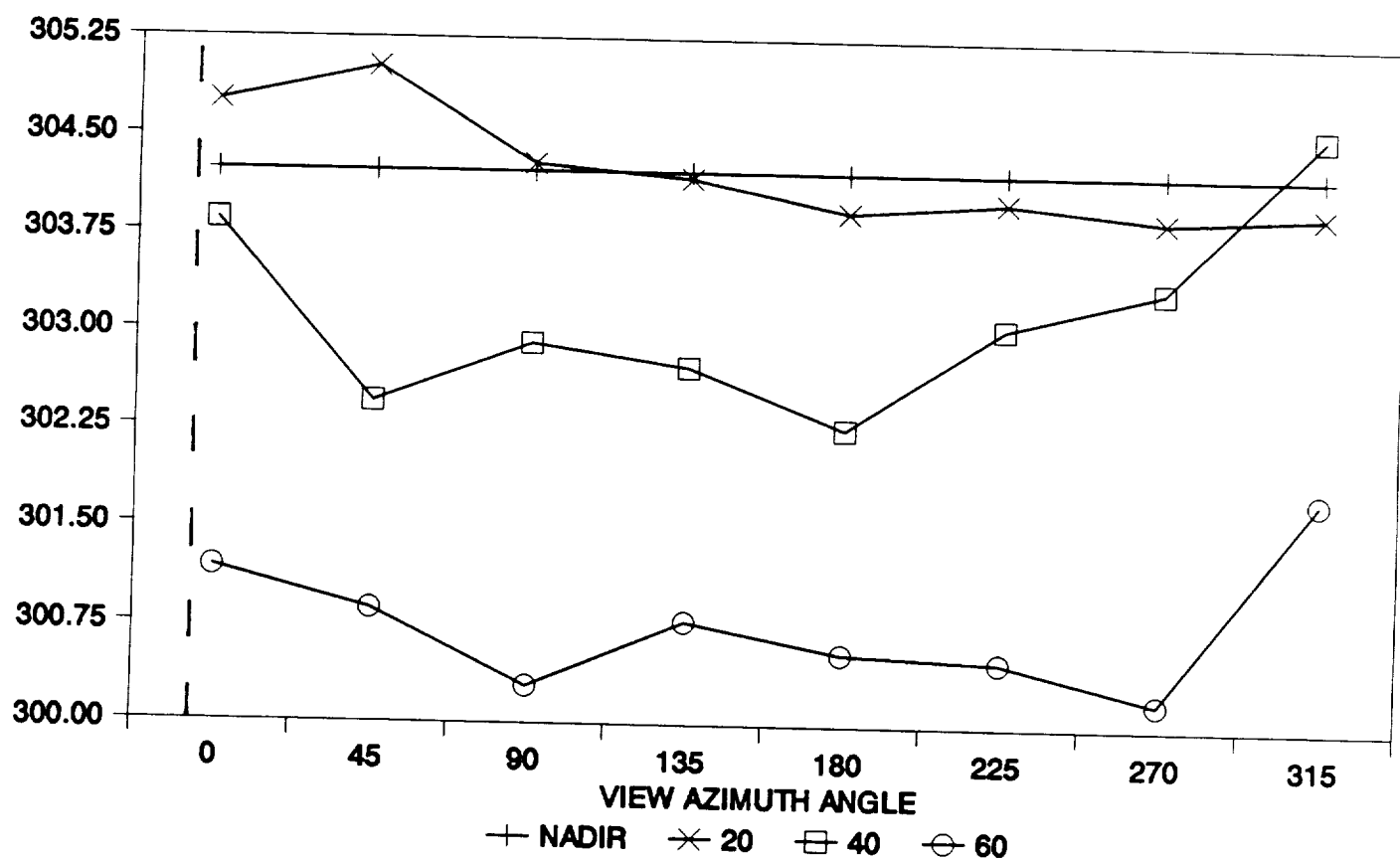
Fig. 4.2 Dependence of apparent surface temperature on view zenith and view azimuth angles and solar position. Day 218 (6 August 1989) 1148 Solar Time. Vertical dashed line represents azimuth observer faced with sun at the observer's back.
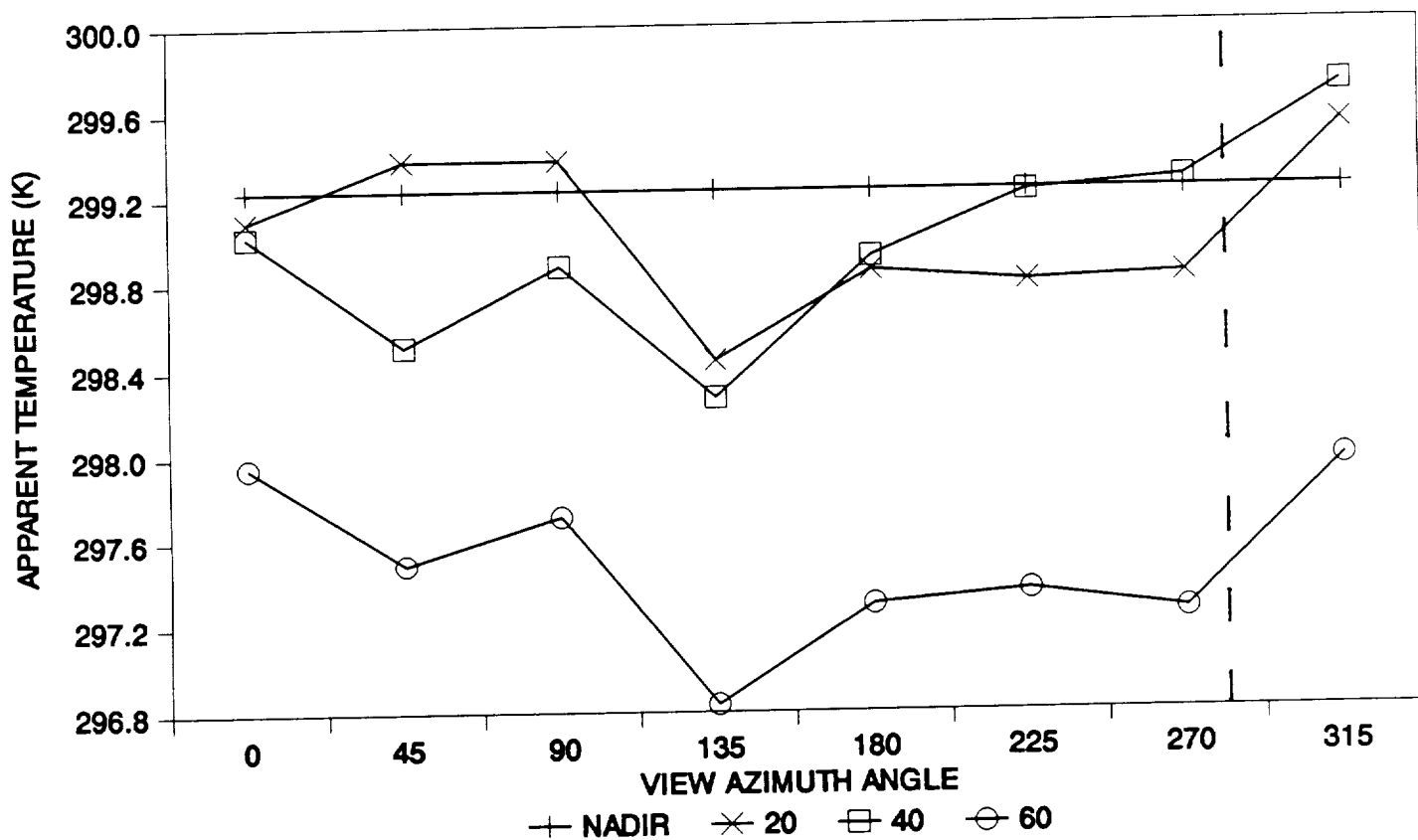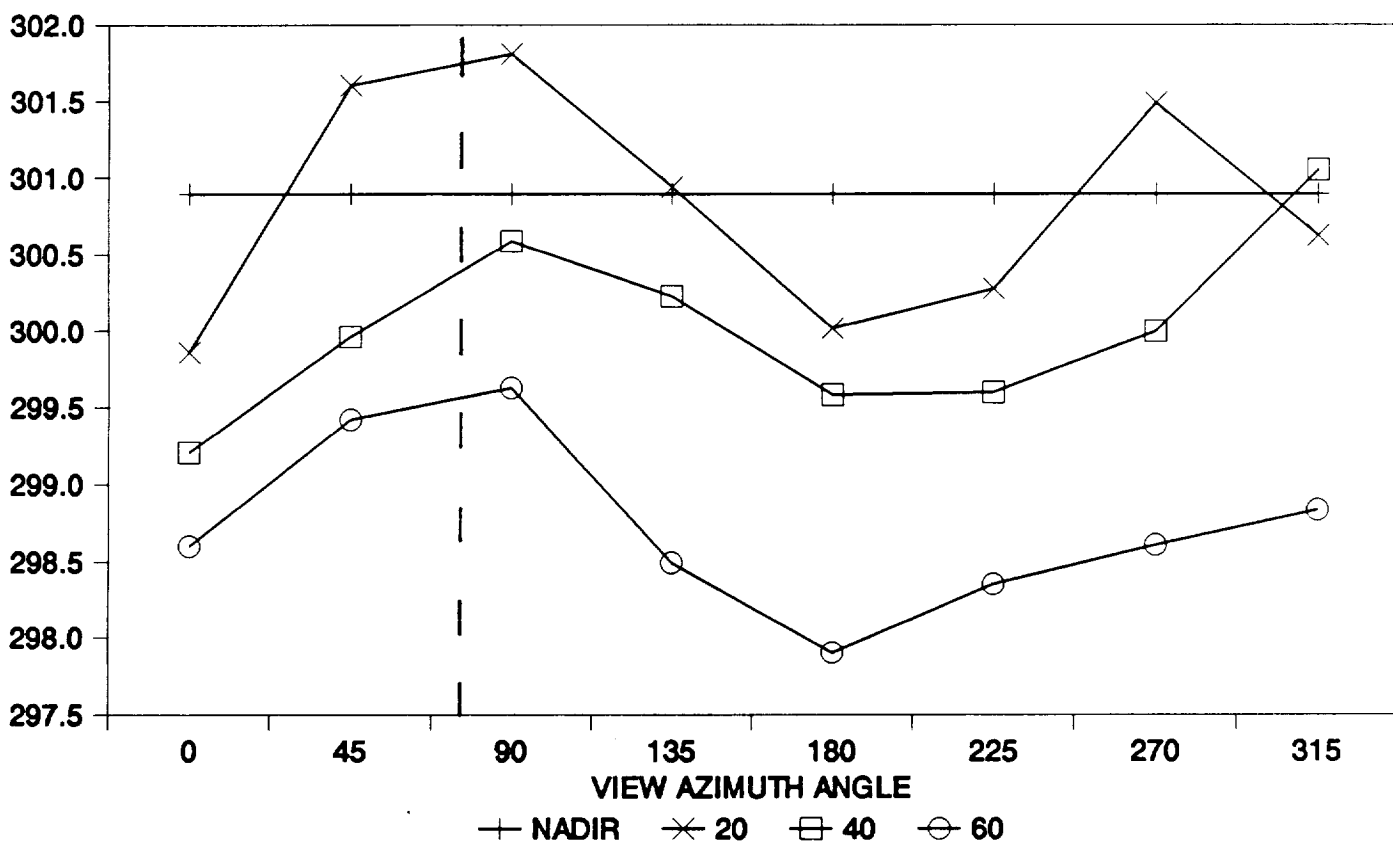
Fig. 4.3 Dependence of apparent surface temperature on view zenith and view azimuth angles and solar position. Day 218 (6 August 1989) 1520 Solar Time. Vertical dashed line represents azimuth observer faced with sun at the observer's back.

angles mostly vegetation is seen. Thus, it is expected that higher surface temperatures would be recorded when radiation from the warm soil contributed more strongly to the emitted radiation stream. Hemispherically averaged temperatures and nadir temperatures are compared to temperatures calculated from the pyrgeometer data in Fig. 4.4. The diagonal line is the 1:1 line, i.e., surface temperatures estimated from the multiangle data perfectly match those calculated from the pyrgeometer data. The nadir-derived temperatures tended to overestimate the temperatures found from the pyrgeometer data, while the hemispherical temperatures under-estimated the pyrgeometer-derived surface temperature.

Visual observation of the dataset suggested that the temperatures measured by the IRTs when facing the sun more closely approximated the temperatures calculated from the pyrgeometer data. Thus, average differences between pyrgeometer and IRT measured surface temperatures were calculated using only the IRT measured temperatures taken with view azimuth angles more than ± 90 degrees away from the solar azimuth angle, denoted as the sun facing IRTs. For example, if the sun is due south, i.e., a solar azimuth of 180°, the sun-facing IRT average is the average of the three readings taken when the observer is facing 135°, 180° and 215°. Results are shown in Table 4.1. From examination of data in the table, several observations can be made. Temperatures measured at the nadir and 20° view zenith angles averaged more than 1°K higher than those calculated from pyrgeometer data. The average difference between the pyrgeometer data and the readings from the 60° view zenith angle underestimated the pyrgeometer derived temperature by nearly 2°K. The temperatures measured at the 40°
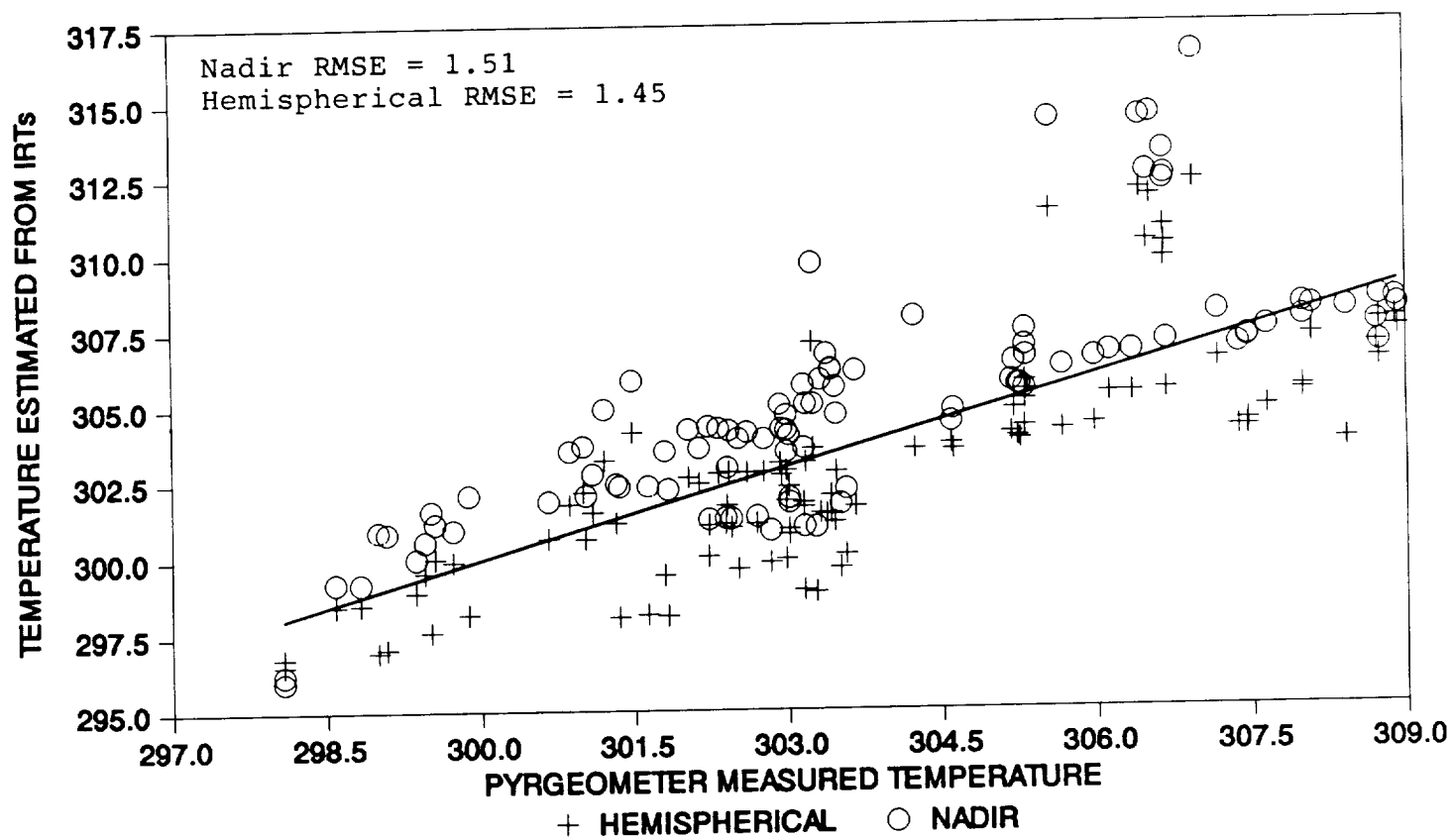
Fig. 4.4 Comparison of surface temperatures from nadir view and hemispherical integration with surface temperatures derived from pyrgeometer measurements.

40

view zenith angle underestimated the pyrgeometer derived surface temperature by only 0.09°K and were not affected very much by considering surface temperatures measured only on the shaded side of the canopy (0.16°K). From this we conclude that temperatures obtained from a view zenith angle of 40° should provide a good estimate of emitted longwave radiation from a grassland canopy.

Table 4.1. Differences in temperatures calculated from pyrgeometer (PIR) data and those obtained with an infrared thermometer (IRT). IRT average is the average temperature of eight readings taken at view azimuth angles in 45° increments. The sun-facing IRT average is the average of readings from the three azimuth angles facing towards the sun.

Zenith View Angle	PIR - IRT Average	PIR - Sun Facing IRT Average
Hemispherical	0.72 °K	
Nadir	-1.38	
20	-1.29	-1.16 °K
40	0.09	0.16
60	1.99	2.21

Comparisons of the calculated aerodynamic temperatures and the remotely sensed apparent surface temperatures on two days are shown in Figs. 4.5 and 4.6. The seemingly large instantaneous jumps in temperatures shown in the graphs actually represent a break in the data collection period. For instance, in Fig. 4.5, the large increase in the sensed temperature at 0945 hours represents a time interval where no surface temperature data were collected. The x-axis (time) is not continuous; it simply denotes times during the day when data were collected. The jagged lines represent the
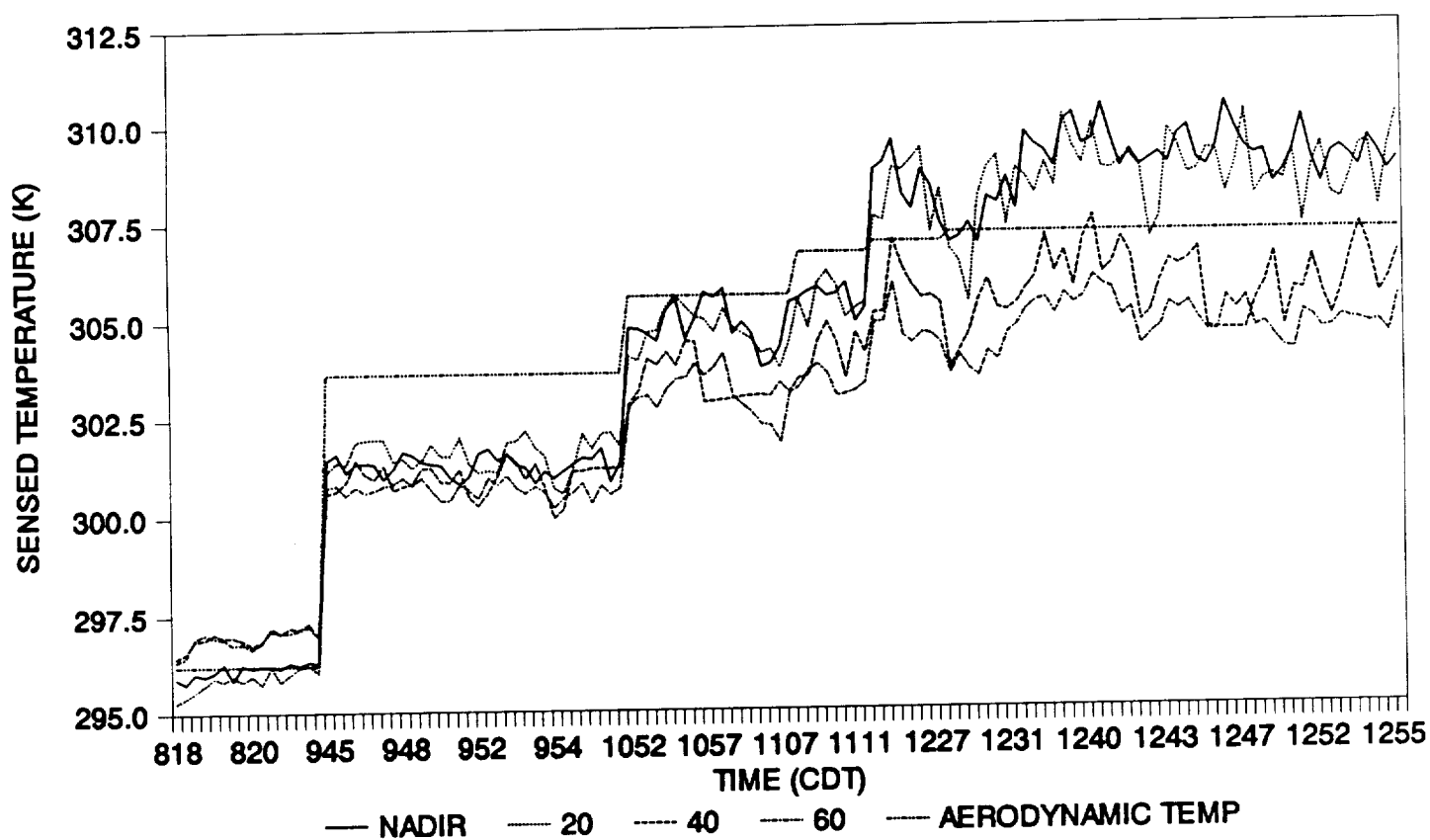
Fig. 4.5 Comparison of surface temperatures measured at four view zenith angles and associated aerodynamic temperatures calculated from sensible heat flux data. Day 209 (28 July 1989).
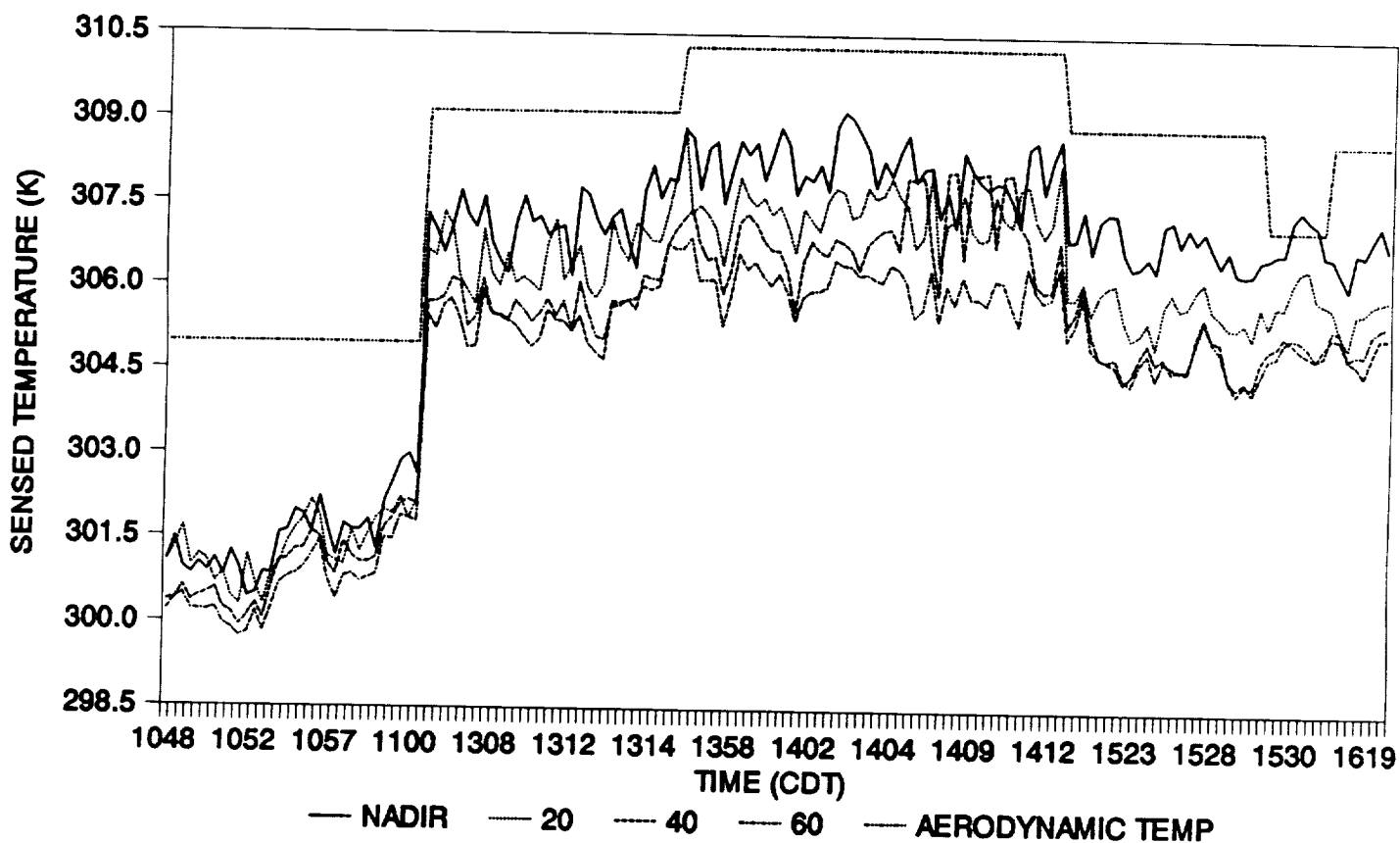
Fig. 4.6 Comparison of surface temperatures measured at four view zenith angles and associated aerodynamic temperatures calculated from sensible heat flux data. Day 216 (4 August 1989).

apparent surface temperatures at each of the four view zenith angles over all of the view azimuth angles. The jagged nature of these curves is due to the variation in the apparent surface temperature with changing view azimuth angles for each view zenith angle. The straighter, nonvariable line represents the aerodynamic temperatures calculated from Eq. (4.3).

On day 209 (Fig. 4.5), with the exception of one time period, the aerodynamic temperatures fall within a range between the highest and lowest sensed apparent surface temperature. On day 216 (Fig. 4.6), the aerodynamic temperatures remained higher over almost the entire collection period, ranging 1.5 to 3°K higher than the highest apparent surface temperature.

Differences in agreement between aerodynamic temperature and surface temperature on the two days could have been influenced by factors which changed between day 209 and day 216. Windspeed was greater on day 216. Advection of sensible heat may have contributed to the overall sensible heat flux on this day and raised the calculated aerodynamic temperatures. The equation used to estimate the friction velocity requires the assumption of a neutral atmosphere so error could be induced into the model when violating this assumption. Data on day 216 were taken under conditions more unstable than those on day 209.

4.4 Summary and Conclusions

Several preliminary conclusions can be drawn from this work:

1) Apparent surface temperatures of prairie grassland canopies can vary by as much as 5°K depending on view zenith and azimuth angles and solar position.

44

2) The average of apparent temperature readings taken at a 40° view zenith angle, either the average of several azimuth readings or readings taken when facing the sun, closely approximated the surface temperature calculated from outgoing longwave radiation data collected by an inverted pyrgeometer.

3) Aerodynamic temperatures ranged from 0 to 3°K higher than nadir-viewed apparent surface temperatures. These results are comparable to those of Huband and Monteith (1986) who found that aerodynamic temperatures were consistently 1°K higher than the apparent surface temperatures when measured at a view zenith angle of 55°.

Further studies are required to investigate relationships between aerodynamic temperature and measured surface temperatures and to define conditions which influence the agreement. Better models for calculating aerodynamic temperatures are needed.

5. ESTIMATION OF SHORTWAVE RADIATION COMPONENTS

5.1 Introduction

Albedo, also referred to as shortwave hemispherical reflectance, is defined as the ratio of reflected solar radiation from a surface to that incident upon it. Albedo should be differentiated from the term spectral reflectivity ($r[\lambda]$), which properly refers to the ratio of reflected energy at a particular wavelength to the total radiant energy incident upon a surface at that wavelength (Huschke, 1959). The albedo determines how much incoming shortwave remains at the surface, and how much is reflected back into the atmosphere.

Albedo is an important parameter in the radiation balance. Kung et al. (1964), asserted the importance of albedo when they stated that the portion of solar radiation remaining at the earth's surface is responsible for the differential heating of the lower atmosphere and that albedo is extremely important in the study of the atmospheric heat budget with its connection to problems of general circulation, air mass modification, and regional climate. Others have commented upon the importance of albedo in arid environments. Otterman (1974) observed a marked difference between the albedos of the Egyptian Sinai and the Israeli Negev deserts. He postulated that the increased albedo of the Sinai would lead to a decrease in convective cloud formation, which would decrease the potential for precipitation thereby intensifying the desertification process. Charney et al. (1977) utilized numerical simulations to observe the effects of changing albedo on rainfall in semi-arid regions. They noted that increased albedo led to a reduction in absorbed solar radiation at the surface which caused a reduction in

46

the amount of sensible and latent heat transferred to the atmosphere. Incoming longwave radiation was also reduced. The overall result was diminished net absorption of radiation at the surface. Consequently, drought conditions were perpetuated. Mintz (1984) reviewed several numerical climate simulation experiments and concluded that changes in available soil moisture or in the albedo produced large changes in the computer-simulated climates. Accurate determination of albedo is, therefore, an important step in understanding climate. It was identified as an important parameter to be determined by remote means in the FIFE study (Sellers and Hall, 1987).

Albedos are typically measured with two pyranometers--one in the upright position recording the incident solar radiation and the other inverted over a surface to record the reflected solar radiation. For fairly large, homogeneous surfaces point measurements of albedo may be extended to represent larger areas. However, large regions rarely exhibit homogeneity either in topography or vegetative characteristics, thereby, limiting the utility of point measurements. Jackson et al. (1985) noted that the area over which a point measurement of incoming shortwave, as measured by a pyranometer, could be extended is governed by the areal uniformity of the scattering and absorbing characteristics of the atmosphere. The expense of procuring the required number of pyranometers, and attendant data logging equipment, to adequately describe large, nonhomogeneous areas becomes quite prohibitive.

Noting the importance of albedo in climate studies, its variability over large regions, and the problems of extending point measurements to larger areas some investigators have attempted to

use pyranometers mounted to aircraft to measure albedo. Bauer and Dutton (1962) mounted pyranometers on light aircraft to evaluate deviations of albedo along several transects in south-central Wisconsin. Kung et al. (1964) performed similar experiments in the northern United States and Canada, and Barry and Chambers (1966) made similar attempts in England and Wales.

Whereas airplanes outfitted with pyranometers present an improvement in measuring albedos over large areas, they do not yield synoptic regional views required for many large-scale experiments. In recent years, efforts at using data from modern remote sensing systems to estimate albedo, as well as incoming solar radiation at the surface, have been made.

5.1.1 Albedo Formulations

Pease and Pease (1972) appraised the use of photography in developing algorithms to estimate albedo. Their work was done with a view towards use of data obtained from the Earth Resources Technology Satellites (ERTS), now known as the LANDSAT series. As an example, one of two multispectral algorithms (equation 5.1) will serve to elucidate their approach. Equation (5.1) makes use of two types of film (panchromatic and infrared).

$$\text{Albedo} = 0.335(R_1) + 0.265(R_2) + 0.4(R_{ir}) \qquad (5.1)$$

R_1 is the average reflectance for the $0.5\mu m$ to $0.6\mu m$ region (panchromatic film), R2 is the average reflectance from $0.6\mu m$ to $0.7\mu m$ (panchromatic film), and R_{ir} is the average reflectance from $0.7\mu m$ to $0.9\mu m$ of the infrared film. The panchromatic film was divided into the two separate wavebands by use of filters. The weighting coefficients of 0.335, 0.265, and 0.4 mean that 33.5%,

26.5%, and 40% of the incident solar energy at the earth's surface is located in the regions represented by R_1, R_2, and R_{ir}, respectively. Densitometry (see Lillesand and Kieffer, 1979, pp. 338-350) of the film negatives produces reflectance values of the targets of interest which are linearly related to "spectral albedo." Spectral albedo refers to the albedo of a specific waveband, and is the same as the term average reflectance used above. For any given frame of film at least one target of known albedo must be present to provide a reference from which albedos could be determined for other targets in the frame. Pease et al. (1976) and Pease and Nichols (1976) used this same approach except that film transparencies were produced from data obtained from airborne electro-optical scanners.

Gillespie and Kahle (1977) assumed that albedo could be expressed as a linear function of digital numbers (DNs) which are produced by multispectral scanners and recorded on magnetic tape. Using a ten channel airborne scanner, their algorithm was written as

$$Albedo - \sum_{n=2}^{10} W_n \ (DN_n) \qquad (5.2)$$

The weighting coefficient (W_n) is an average value based upon ground calibration from a portable spectrometer for several varying sites, the filter function for each channel (n) of the spectrometer, and the average solar radiation in each channel of the airborne multispectral scanner.

Robinove et al. (1981) presented algorithms whereby the pixel brightness values (DNs) of the LANDSAT series of satellites 1 through 3 can be used to estimate albedo. Four assumptions were necessary in order to develop the equations: i) the terrain is a Lambertian reflector, ii) average terrain slope is zero, iii) atmospheric scattering is only additive, and iv) the sun angle contribution to the scene brightness is uniform over the entire scene. In generic form, their algorithm is

$$Albedo - \sum_{j=4}^{7} \frac{(B_j - B_{jmin})}{(C1_j) \ (sin\alpha) \ (C2_j)} \tag{5.3}$$

where

B_j = digital number of pixel in band j
B_{jmin} = minimum DN in the scene in band j
$C1_j$ = sensor and band specific constant
α = solar elevation
$C2_j$ = sensor and band specific constant

The term B_{jmin} in the numerator is an atmospheric correction. This correction is based upon the assumption that the lowest brightness value in a scene represents the atmospheric scattering contribution to the measured brightness value of each pixel. $C1_j$ represents the average irradiance at the top of the atmosphere, $C2_j$ converts the pixel DNs into radiances, and $sin\alpha$ is a correction factor which allows calculation of albedo as if the sun were at nadir. Because the above equation does not attempt to cover the entire shortwave spectrum the albedo estimated equation (5.3) is really a spectral albedo. It was termed "LANDSAT albedo" by the authors.

An alternative method of albedo calculation from LANDSAT data was presented by Robinove et al. (1981):

$$\text{Albedo} = (\pi/I \; \sin\alpha) * \Sigma \, (B_j/G_j) \tag{5.4}$$

where

$$
\begin{aligned}
I &= \text{total solar irradiance in the four} \\
&\quad \text{channels (j)} \\
\alpha &= \text{solar elevation} \\
B_j &= \text{DN of pixel} \\
G_j &= \text{gain in DN per unit radiance}
\end{aligned}
$$

Brest (1987) and Brest and Goward (1987) presented a simple algorithm from which albedo can be estimated from LANDSAT data using only channels 4 and 7. For a vegetated surface their formulation was written as

$$\text{Albedo} = 0.526(B4) + 0.362(B7) + 0.112([0.5(B7)]) \tag{5.5}$$

where B4 and B7 equal the percent reflectance in the respective band. The values of 0.526, 0.362, and 0.112 are weighting coefficients used to make the LANDSAT data account for the whole solar spectrum, thereby providing an estimate of the total shortwave albedo. Because the LANDSAT multispectral scanner (MSS) does not have a channel in the mid-infrared, a surrogate was created by multiplying the near-infrared value (B7) by 0.5. This is because the mid-infrared yields a response approximately one-half that of the near-infrared. Brest's technique involved calibration of the satellite data by measuring certain calibration targets at the surface with a camera-based radiometer. A gray vinyl reference panel was used as a field standard. Voltages recorded from the radiometer were directly proportional to the irradiance incident on the detector, and because the reference panel reflectance was known, the target reflectance was easily calculated (Brest, 1987). Calibration then proceeded by linearly regressing the satellite data to the field-measured reflectance of the targets.

51

The above mentioned albedo algorithms all assume a Lambertian surface. Only data obtained at nadir were utilized in the formulations. Effects of surface anisotropic reflectance, solar zenith angle, and view angle were not assessed. All equations, except those presented by Robinove et al. (1981), required field calibration to produce an estimate of albedo. Except for the work of Gillespie and Kahle (1977) no simultaneous independent measures of albedo were taken to verify the accuracy of the estimates, and no author reported on the performance of their models in regards to actual albedo measurements.

5.1.2 Anisotropy

When an incident beam of radiation strikes a surface, one of several things may happen if it is reflected. If the incident beam is completely reflected at an angle equal to the angle of incidence it is termed specular reflectance (Fig. 5.1). Near-perfect specular reflectance occurs when the incident beam is reflected in a diffuse manner with the angles of reflectance close to that of the incidence angle. A near-perfect diffuse reflector is one in which the incident beam is reflected nearly equal in all directions. An isotropic reflector is also known as an ideal diffuse reflector or a Lambertian surface. Lambert's cosine law states that the flux per unit solid angle in any direction from a perfectly diffuse plane surface varies as the cosine of the angle between that angle and the normal to the surface (Slater, 1980). The key to understanding of the cosine law of Lambert is the phrase "per unit solid angle." According to Monteith (1973), when a radiometer's view angle of the radiator's surface changes the

amount of radiation being sensed by the radiometer will appear to be the same. Therefore, radiation coming from a surface element and the intensity of that radiation must both be independent of the angle γ. However, the flux per unit solid angle divided by the true area viewed by the sensor will be proportional to cos γ. A Lambertian surface, then, is one in which a beam of radiation is reflected from it equally in all directions. Anisotropic diffuse reflectance is characterized by the incident beam being reflected unequally. In this case the incoming solar beam is diffused but exhibits a series of preferred angles of reflection and in a preferred direction (Fig. 5.2). Most natural surfaces, such as vegetation and soil, are anisotropic diffusers of radiation.

5.1.3 Bidirectional Reflectance

Assuming that a surface exhibits Lambertian properties is a necessary step towards estimating albedo from data obtained from nadir-looking sensors. Smith et al. (1980) suggested that under certain circumstances the Lambertian assumption for LANDSAT data may be valid. However, other investigators have shown that fairly significant errors may occur if anisotropy is not considered (Salomonson and Marlatt, 1971; Eaton and Dirmhirn, 1979).

As Colwell (1974) and Kimes et al. (1980) point out, there are many parameters that influence the anisotropy of vegetated surfaces. These parameters include the optical properties of individual leaves, canopy architecture, characteristics of the underlying soil and leaf litter, solar zenith and azimuth, sensor view zenith and azimuth, atmospheric effects, leaf area index, and
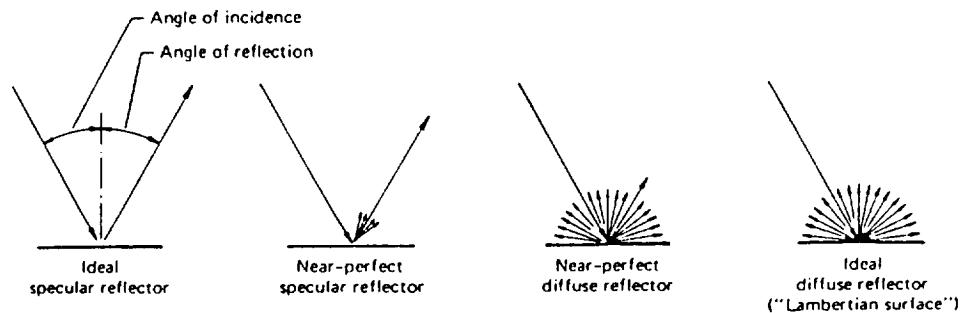
Figure 5.1 Specular versus diffuse reflectance. (Adapted from Lillesand and Kieffer, 1979.)
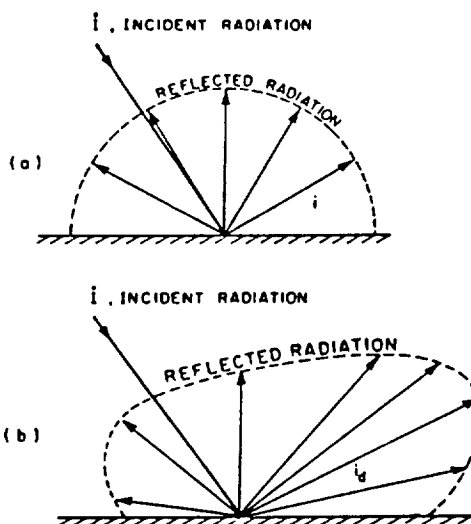
Figure 5.2 Isotropic diffuse reflection (a) and anisotropic diffuse reflection (b). (Adapted from Iqbal, 1983.)

54

optical properties of the canopy. Considerable effort has been exerted towards quantifying and understanding the effects of solar and view angles on surface reflectance (Bartlett et al., 1986; Duggin, 1977; Egbert and Ulaby, 1972; Holben and Fraser, 1984; Jackson et al., 1979; Kimes et al., 1980, 1984; Pinter et al., 1983; Ranson et al., 1986; Slater and Jackson, 1982).

There are many factors that influence anisotropic reflectance suggesting that a nadir view does not necessarily yield enough information to effectively quantify some important surface characteristics. There are two angles used to characterize the anisotropy of natural surfaces--the angle of incidence of the solar beam and the angle from which the reflection is being viewed. The bidirectional reflectance distribution function (BRDF) is a mathematical description of anisotropic reflectance (in a hemisphere) from a surface and may be written as

$$\text{BRDF} = I_r(\theta_i, \phi_i; \theta_r, \phi_r) / I_o(\theta_i, \phi_i; \theta_r, \phi_r) \tag{5.6}$$

where

I_o = incident radiation
I_r = reflected radiation
θ = azimuth angle
ϕ = zenith angle
i = incident beam
r = reflected beam

In practice, the BRDF can never be measured directly because it is a ratio of infinitesimals (Nicodemus et al., 1977); however, it can be approximated. Further elaboration and derivation of the BRDF is provided by Nicodemus et al. (1977), Swain and Davis (1978), and Slater (1980). The importance of the bidirection concept is discussed in the following papers: Suits (1972), Kimes et al.

(1985,1987), Otterman et al. (1987), Ross and Marshak (1988), Norman et al. (1985), and Kimes and Sellers (1985).

In an attempt to account for the BRDF, Kriebel (1979) developed an equation that utilized biconical reflectance factors obtained from an eight channel airborne radiometer. His equation is

$$\text{Albedo} = \Sigma_{\Delta\lambda} \; A(\lambda)(E\lambda)(\Delta\lambda)/\Sigma_{\Delta\lambda} \; (E\lambda)(\Delta\lambda) \qquad (5.7)$$

The quantity $A(\lambda)$ is a spectral albedo that is obtained by using the biconical reflectance factors as inputs to a radiative transfer model. Incoming flux density $(E\lambda)$ is averaged over the spectral interval $\Delta\lambda$. Results from equation (5.7) appear to be reasonable and may be found in Kriebel (1976, 1978, 1979).

5.1.4 Incoming Shortwave

The incoming solar radiation component of the net radiation balance is typically measured with an upright pyranometer. Point measurements of incoming solar radiation may be extended to a much larger area if the atmospheric scattering and absorbing properties can be assumed to be uniform over the region (Jackson et al., 1985). In order to overcome some of the problems that large regions introduce, modelers and those working in the field of remote sensing have developed procedures to produce reasonably accurate estimates of incident shortwave radiation.

Dave et al. (1975) and Kneizys et al. (1980) constructed large and complex radiative transfer models for the estimation of solar irradiance at the earth's surface, given that certain atmospheric parameters are known or can be obtained. Bird and Riordan (1984)

developed a simple computer algorithm for this estimation. Other examples of modeling attempts include Temps and Coulson (1977), Klucher (1979), El-Adawi et al. (1986), Isard (1986), Kamada and Flocchini (1986), Skartveit and Olseth (1986), and Perez et al. (1986).

Some investigators have evaluated the use of satellite data to produce estimates of incoming shortwave at the spatial resolution of the sensor. Hanson (1971) used Nimbus 2 data to obtain monthly averages of solar irradiance at the earth's surface. Tarpley (1979) utilized data from the Visible and Infrared Spin Scan Radiometer (VISSR) on board a GOES satellite. His hourly estimates of incident solar radiation were summed to yield daily total insolation, which were within ten percent of measured values. Gautier et al. (1980) and Diak and Gautier (1983) developed a model that utilized data from a GOES satellite to calculate the solar irradiance for both cloudy and clear skies. For the clear sky case, a standard error of five percent was observed, for the completely overcast case a standard error of 14 percent occurred. For all cases daily insolation was estimated to within nine percent of the measured mean.

5.1.5 The Method of Jackson (1984)

Of special interest to the present research is the procedure that Jackson (1984) used in calculating the total solar radiation incident upon and reflected from a surface. Using an eight-band Barnes MMR and a four-band Exotech radiometer, reflectance data were collected over a barium sulfate field reference panel, bare soil plots, and wheat canopies exhibiting a range of leaf area

indices (LAIs). All reflectance data were obtained from a nadir position.

A radiative transfer model was used to determine the quantity and spectral distribution of solar radiation at the surface of the earth as the level of atmospheric scattering, precipitable water, and solar zenith angle were varied. Once the total amount of incident solar energy (T) is known, the amount sensed by the remote sensing instruments (P) can be computed. This is done by integrating the area under the solar irradiance curve between the wavelengths of each channel of the instruments, then summing the energy in the channels for each instrument. When the ratio P/T is calculated, the resulting number represents the percentage of the total incoming solar energy sensed by the instrument.

Jackson determined total incoming solar radiation by converting the voltage data from the instruments, obtained over the field reference panel, into energy terms, summing the energy in the instrument channels, and dividing by the P/T ratio. When compared to pyranometer values, the calculated values were found to be within 5.5 percent.

Computation of the solar radiation reflected from the bare soil and wheat canopy plots required the use of spectral reflectance curves (0.4μm - 2.5μm) for both of the surface types. The P/T ratios were calculated by first multiplying the spectral reflectance curves by the various solar irradiance curves produced by the radiative transfer model. The total energy (T) is then calculated by integration of the curves produced by the multiplication process, and the partial spectrum (P) energy is determined from these new curves in the same manner reported above. Voltages

obtained over the bare soil and wheat plots, in each channel, were converted into energy terms, summed, and divided by the appropriate P/T ratio. Calculated values of total reflected solar radiation compared well to values recorded by an inverted pyranometer.

Our procedure, reported below, was developed independent from Jackson's (1984) approach; but the two methods are quite similar. One important difference between the two approaches is that Jackson's method used only nadir values, whereas our approach incorporates bidirectional data obtained from several view zenith angles. Other differences between the two techniques will be noted below.

5.2 Materials and Methods

5.2.1 Instrumentation

A Barnes Multiband Modular Radiometer (MMR) 12-1000 (Robinson et al., 1982) was used to collect bidirectional reflectance data over prairie vegetation on the FIFE site. The MMR has eight channels (Page 14). Only the channels measuring reflected radiation (1-7) are used in this portion of the study. Channels 1 through 4 of the MMR emulate thematic mapper (TM) bands 1 through 4; MMR 7 emulates TM 6; MMR 8 emulates TM 6; and MMR 7 is equivalent to TM 7. A 15 degree field-of-view (FOV) was used.

A specially designed portable mast (Fig. 5.3) held the MMR approximately three meters above the soil surface, producing a view spot size of 0.8 meters. Measurements were made from seven view angles located in or near the principal plane of the sun. These angles were nadir and 20°, 35°, and 50° to either side of nadir. Norman and Walthall (1985) suggested that most bidirectional
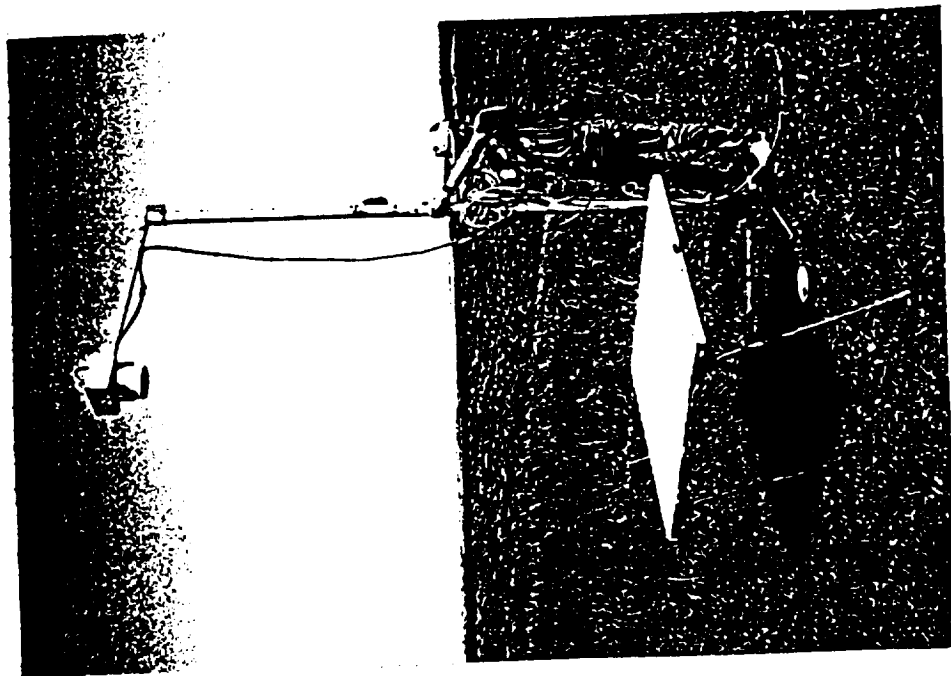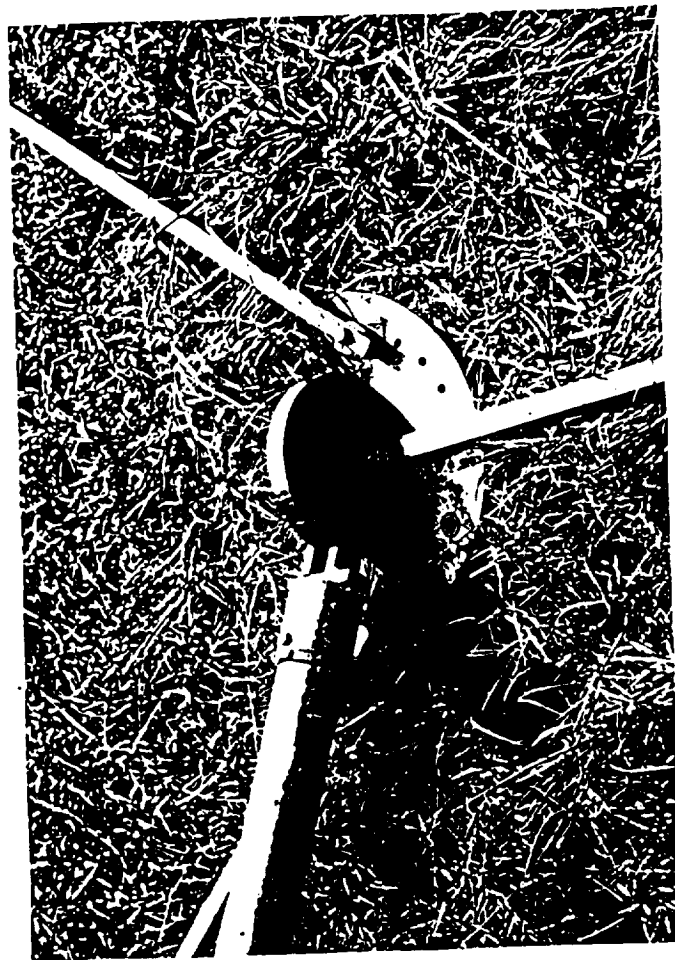
Figure 5.3 (a) The eight-channel Barnes MMR mounted on the 3.4m tall portable mast. Here the MMR is recording data over the field reference panel. (b) The base of mast designed to view a particular spot on the surface from various view zenith angles.

(a)

(b)

information for vegetative and soil surfaces is found in the principal plane of the sun and within viewing angles (view zeniths) out to approximately 50 degrees either side of nadir.

During 1987 a portable A-frame was fitted with a net radiometer and an Eppley PSP mounted to measure reflected solar radiation. The same PSP was rotated to the upright position to record the incoming solar radiation. In 1988 two PSPs, one to measure incoming solar radiation and the other to measure reflected solar radiation, and two net radiometers were mounted on the A-frame.

Data from a barium sulfate ($BaSO_4$) reference panel were used in 1987 to calculate the incoming solar component, and to calculate reflectance factors (Robinson and Biehl, 1979). During 1988 a molded halon reference panel was used. Both reference panels are near-Lambertian and highly reflective (near 100 percent) of incident solar radiation.

Reflectance factors are calculated as the ratio of the canopy radiance (CR) in a particular band (j) to the panel radiance (PR) in the same band

$$RF_j = (CR_j / PR_j)*100 \tag{5.8}$$

The units of CR and PR are (Wm^{-2} μm^{-1} sr^{-1}).

5.2.2 Instrument Calibration

Robinson and Biehl (1979) and Kimes and Kirchner (1982) noted that reference panels are not perfectly Lambertian, and, therefore, must be calibrated to account for their non-Lambertian charac-teristics. Reference panels used in this study were calibrated using the procedure outlined in Jackson et al. (1987).

61

Radiometric calibration of the reflective channels (1-7) of the MMR was performed at the NASA Goddard Space Flight Center in Greenbelt, Maryland through the cooperative efforts of Frank Wood and Brian Markham of NASA, Dr. Elizabeth Walter-Shea of the University of Nebraska-Lincoln, and Janet Kileen of Kansas State University. The calibration procedures are outlined in Markham et al. (1988). The infrared channels (5-7) of the MMR have a lead sulfide detector which is sensitive to temperature (Jackson and Robinson, 1985) so the thermal stability of these channels was also evaluated (Jackson et al., 1983a).

Eppley PSPs were calibrated using a shading technique as described in Iqbal (1983, pp. 360-362). However, the values derived from this calibration technique did not deviate more than two percent from the factory supplied constants, so the factory values were used.

5.2.3 Experimental Procedures

At the beginning of measurement at a site the MMR was mounted over the field reference panel in a nadir position and data obtained. The MMR sensors were then covered in order to obtain a "dark" reading to define the electronic noise level. After taking the calibration readings the MMR was moved into a plot, placed in the principal plane of the sun, and data gathered at each of the seven view zeniths. Once the bidirectional data were obtained the MMR was removed from the plot and the A-frame instrumentation was placed over the MMR-viewed area. This procedure was followed for each plot over which the MMR obtained data, and only required four to five minutes to perform. Every twenty to twenty five minutes

62

the MMR was returned to the reference panel for the calibration readings.

5.2.4 Computational Methods--Albedo

The defining equation for albedo as measured from a hemispherical sensor, such as a pyranometer, may be written as

$$\rho(\theta_i) = \frac{\int_{\lambda_L}^{\lambda_u} E(\lambda,\theta_i) \int_0^{2\pi} \int_0^{\pi/2} \rho(\lambda;\theta_i,\theta_v,\phi_v)\cos\theta_v\sin\theta_v\,d\theta_v\,d\phi_v\,d\lambda}{\int_{\lambda_L}^{\lambda_u} E(\lambda,\theta_i) \int_0^{2\pi} \int_0^{\pi/2} \cos\theta_v\sin\theta_v\,d\theta_v\,d\phi_v\,d_\lambda} \qquad (5.9)$$

where

$\rho(\theta_i)$ = hemispherical reflectance as a function of the source incidence angle (θ_i)

λ_L = lower wavelength of instrument sensitivity

λ_u = upper wavelength of instrument sensitivity

$\rho(\lambda;\theta_i,\theta_v,\phi_v)$ = reflected radiation as a function of view zenith (θ_v), view azimuth (ϕ_v), source incidence angle (θ_i), and wavelength (λ)

$E(\lambda,\theta_i)$ = flux density of incident solar radiation as a function of wavelength and source incidence angle.

Albedo is the ratio of reflected solar radiation, integrated over wavelength and hemisphere of view (the numerator), to the radiation incident upon the surface identically integrated (the denominator). Performing integration over the limits of θ_v and ϕ_v yields

$$\rho(\theta_i) = \frac{\int_{\lambda_L}^{\lambda_u} \rho_H(\lambda,\theta_i)E(\lambda,\theta_i)\,d\lambda}{\int_{\lambda_L}^{\lambda_u} E(\lambda,\theta_i)\,d\lambda} \qquad (5.10)$$

which defines albedo in terms of hemispherical spectral reflectance, $\rho(\lambda,\theta_i)$, and total incident radiation.

Equation (5.10) can be rewritten in the following equivalent way

$$\rho(\theta_i) = \int_{\lambda L}^{\lambda u} \rho_H(\lambda, \theta_i) \frac{E(\lambda, \theta_i)}{\int_{\lambda L}^{\lambda u} E(\lambda, \theta_i) d\lambda} d\lambda \qquad (5.11)$$

which can partitioned according to discrete wavebands. For a broadband sensor like the MMR, equation (5.11) can be written as:

$$\rho_{BB}(\theta_i) - \sum_{j=1}^{7} \rho_H(\lambda, \theta_i)_j \int_{L_j}^{U_j} \frac{E(\lambda, \theta_i)}{\int_{0.3}^{4.0} E(\lambda, \theta_i) d\lambda} d\lambda \qquad (5.12)$$

where

$\rho_{BB}(\theta_i)$ = albedo calculated from a broad-band sensor data
j = waveband designation
L_j = lower wavelength for MMR channel j
U_j = upper wavelength for MMR channel j

The values of 0.3 and 4.0 are the approximate lower and upper wavelength limits for the solar spectrum, respectively. The term

$$\int_{L_j}^{U_j} E(\lambda, \theta_i) \, d\lambda / \int_{0.3}^{4.0} E(\lambda, \theta_i) \, d\lambda$$

--equations (5.11) and (5.12)--represents weighting coefficient for a particular waveband interval based upon a solar irradiance curve at the earth's surface.

Using approximations, equation (5.12) can be rewritten as:

$$\rho_{BB}(\theta_i) - \sum_{j=1}^{7} (RF_{Hj}) \, (W_j) \qquad (5.13)$$

where RF_{Hj} is a hemispherical reflectance factor for waveband j and W_j is a weighting coefficient for the respective band. Thus, it should be possible to estimate albedo from the MMR data as a function of hemispherical reflectance factors. To do that the bidirectional RFs for a given MMR waveband must be first converted into a hemispherical value and then weighting coefficients must be developed for each waveband of the MMR.

5.2.5 Hemispherical Reflectance Factors

Walthall et al. (1985) developed a simple multiple regression technique whereby bidirectional reflectance data, obtained at three or more view zenith angles, could be used to simulate hemispherical reflectance. Their model is expressed as

$$r = a\theta_v^2 + b\theta_v\cos(\phi_v - \phi_s) + c \qquad (5.14)$$

where,

    r = reflectance in a given waveband
    θ_v = view zenith angle in radians
    ϕ_v = view azimuth angle in radians
    ϕ_s = solar azimuth angle in radians
  a,b,c = coefficients derived from the multiple
             regression procedure

Recalling the experimental procedure, the MMR was aligned in the principal plane of the sun and reflectance data obtained at seven view zenith angles. Therefore, the second term on the right hand side of equation (5.14) reduces to the view zenith angle being multiplied by 1 or -1 depending upon which side of nadir the data are acquired.

Equation (5.14) is used on a band-by-band basis. That is, the seven RFs in a given band (one for each of the seven angles) are regressed against the square of the respective view zenith angles and the seven view zenith angles which have been multiplied by 1 or

65

-1. The multiple regression then supplies the coefficients a, b, and c. The coefficients "a" and "c" are used to calculate the hemispherical reflectance factor (RF_H) for the given waveband (j) from the following equation.

$$RF_{Hj} = \frac{(2.305)(a)}{\pi} + c \tag{5.15}$$

5.2.6 Weighting Coefficients

Weighting coefficients were used in the algorithms of Pease and Pease (1972), Gillespie and Kahle (1977), Kriebel (1979), and Brest (1987). These coefficients are ratios of the global solar irradiance at the earth's surface in a given sensor waveband to the total global solar irradiance at the earth's surface. Thus, if the global solar irradiance in a radiometer waveband is 200 Wm^{-2} and the total global irradiance is 1000 Wm^{-2}, the weighting coefficient for that channel is 0.20.

To determine the weighting coefficients, knowledge of the spectral distribution of the global solar radiation at the earth's surface must be adequately known. Bird and Riordan (1984, 1986) developed a simple model, SPCTRAL2, which produces such a spectral distribution if certain parameters are known. These parameters include the aerosol optical depth, precipitable water vapor in centimeters, surface pressure in millibars, site latitude and longitude, day number of the year, solar zenith angle, incidence angle, and angle of slope at the surface. This model adjusts the spectral distribution of the incident solar radiation at the top of the earth's atmosphere for absorption by ozone and water vapor, accounts for the path length that the solar beam must travel, and

takes into consideration Mie and Rayleigh scattering based upon turbidity of the atmosphere.

Rather than producing a separate solar irradiance curve for each time the MMR collected data over a plot, it was decided to use input parameters that would reflect "average conditions" for the time period over which the data were obtained. Iqbal (1983) reported values of precipitable water and aerosol optical depth for each month of the year for various locations in the United States. From these tables an average value for atmospheric water depth was determined to be 2.663 cm while that for aerosol optical depth was 0.1 (clear sky). Surface pressure observations made at the FIFE site suggest that a value of 966 millibars is representative for the measurement period during which MMR data were collected. Single values of latitude (39 degrees) and longitude (96 degrees) are representative of all plots within the FIFE study area. With these parameters remaining constant, the solar zenith angle was varied from 0° to 70° in increments of 10 degrees thereby yielding eight separate solar irradiance curves from which the weighting coefficients were calculated.

Figure 5.4 is an example of a solar irradiance curve produced by the SPCTRAL2 model. The nominal waveband limits of the MMR are depicted as the cross-hatched boxes in the lower portion of the figure. Recall that the definition of shortwave albedo requires that the whole solar spectrum be accounted for. Because the MMR samples the solar spectrum in discrete, non-contiguous wavebands, it must be "forced" to sample the whole spectrum. This is done by "extending" the upper and lower limits of each waveband where
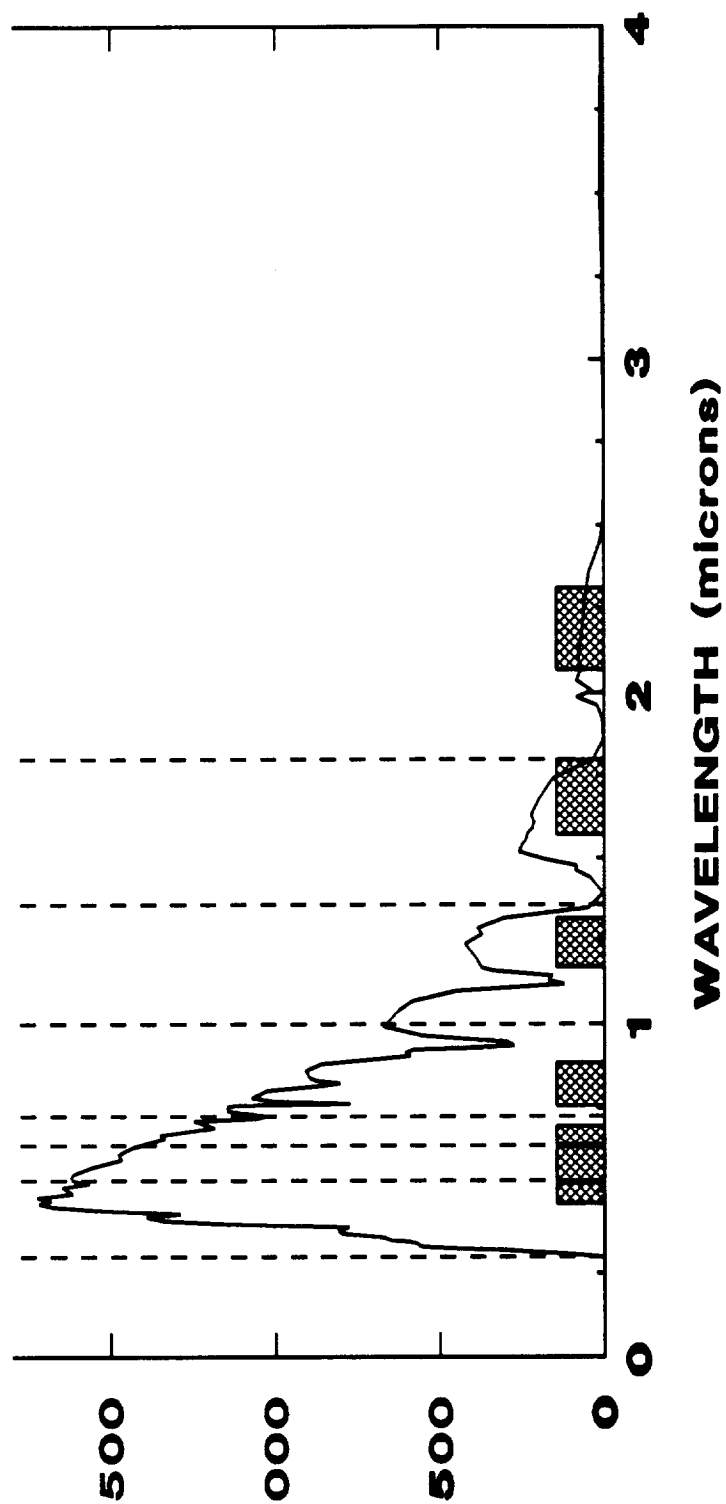
Figure 5.4 Distribution of global solar energy at the surface of the earth. Nominal MMR bandwidths indicated by the cross-hatched boxes; extended bandwidths indicated by the dashed lines.

possible. These extended waveband limits are shown as the dashed
lines (Fig. 5.4), and are listed in Table 5.1.

TABLE 5.1
Extended Waveband Limits of
the Barnes MMR

Channel Number	Extended Waveband Limits (microns)
1	0.3000 - 0.5200
2	0.5200 - 0.6150
3	0.6150 - 0.7250
4	0.7250 - 1.0000
5	1.0000 - 1.3600
6	1.3600 - 1.8000
7	1.8000 - 4.0000

Integration (trapezoidal rule) of the area under the curve for
each extended and unextended MMR waveband was performed for each of
the eight SPCTRAL2 simulations. The weighting coefficients, then,
represent the fraction of the total energy contained within a
specific MMR waveband. Summing the eight coefficients for each
band and dividing by eight yields the average values used in this
study.

Unextended weighting coefficients are denoted by the symbol
W'_j and the extended coefficients are given by the symbol W_j in the
equations that follow. When summed, the W'_j for a given MMR yield
a number comparable to the P/T ratio of Jackson (1984).

5.2.7 Computational Method--Incoming Shortwave

Experimental procedure called for acquisition of MMR data over
the field reference panel every 20 to 30 minutes. Data acquired
from the panel can be used to estimate the incoming solar radiation
with corrections for its non-Lambertian properties and sun angle
effects (Robinson and Biehl, 1979; Kimes and Kirchner, 1982;

Jackson et al., 1987). Incoming solar radiation for a given plot was linearly interpolated between the "before" and "after" reference panel readings.

Incorporating the method of Jackson (1984), the radiance data acquired over the panel were converted into estimates of incoming solar radiation by the following algorithm

$$ISW_e = \Sigma (Ref_j)/(P/T) \tag{5.16}$$

where ISW_e is the estimate of incoming solar radiation, Ref_j is the radiance reflected from the panel in channel j, and (P/T) is the fraction of the solar energy sensed by the instrument. Jackson (1984) converted his MMR voltages directly into units of $[Wm^{-2}]$ prior to use in equation (5.16). However, the NASA calibration procedures led to the voltages of MMRs used in this study to be converted into units of $[Wm^{-2}\mu m^{-1}sr^{-1}]$. Therefore, equation (5.16) takes the form

$$ISW_e = \pi \sum_{j=1}^{7} (Ref_j)\ (\Delta\lambda_j)/(P/T) \tag{5.17}$$

where $\Delta\lambda_j$ is the bandwidth of MMR channel j in $[\mu m]$. The value of π comes from the integration of $\int_0^{2\pi}\int_0^{\pi/2}\cos\theta_v\sin\theta_v d\theta_v d\phi_v$, which is the hemisphere of view and has units of [sr]. Values of (P/T) are MMR-dependent and are determined by summing the W'_j for the appropriate MMR. For MMR #103 (P/T) = 0.529 and for MMR #128 (P/T) = 0.536.

Equation 5.18 may be used to estimate incoming shortwave radiation

$$ISW_e - \pi \sum_{j=1}^{7} [Ref_j (\theta_j)] (\Delta\lambda_j) (W_j/W'_j) \qquad (5.18)$$

or more conveniently as equation (5.19)

$$ISW_e = \pi\Sigma(Ref_j)(\Delta\lambda_j)(W_j/W'_j) \qquad (5.19)$$

it is observed that the main difference between equation (5.19) and the method of Jackson (1984) is that the value of $(Ref_j)(\Delta\lambda_j)$ is adjusted by a band-specific weighting coefficient. Jackson's method treats all bands as having the same weighting coefficient.

5.3 Results and Discussion

5.3.1 Evaluation of Equation (5.13)

An initial test of equation (5.13) was performed on a data set acquired on June 4, 1987 at site 8. Data were collected on eight to twelve plots at the site at six different times during the day, resulting in 56 cases for comparison of the measured albedos to those calculated from equation (5.13). Site 8 proved to be nearly homogeneous in terms of soil, topography, and vegetative condition. The measurements and estimates of albedo are averaged for each of the six data collection periods and plotted on Figure 5.5. It is observed that both the measured albedos and estimates behave as expected; i.e., higher albedo in the morning and late afternoon than at mid-day. It is also noted that the estimates are higher than their measured counterparts, and well outside one standard deviation of the measured albedo. The average measured albedo of the plots ranges from approximately 15 percent to almost 25 percent, while the estimates range from almost 19 percent to near 29 percent. Irons et al. (1988) collected bidirectional reflectance

71
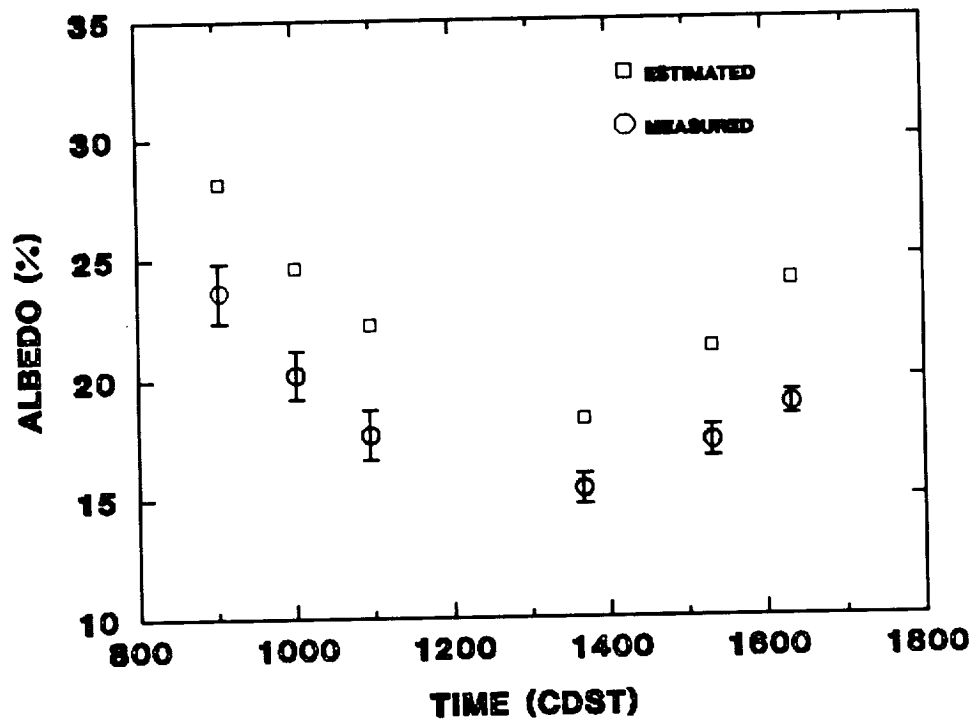
Figure 5.5 Comparison of mean measured albedo to mean albedo estimated from equation (5.13). Data acquired at Site 8 on day 155. Error bars indicate plus and minus one standard deviation.

factor data from a vegetated surface at the Konza Prairie during June 1986. Using a different calculation technique, they produced estimates of albedo that ranged from 27 percent to nearly 38 percent over the course of a day during mid June. Similar results were also obtained during early July. The results from Irons et al. (1988) are very similar to those mentioned above, but the degree of error encountered by them is not known because no actual measurements of albedo were available for comparison.

Each of the 56 estimates of albedo were plotted against their corresponding measured value (Fig. 5.6) and a linear regression was performed. Although the correlation coefficient was fairly good (r = 0.943), basic descriptive statistics revealed a mean relative error of +23 percent. The mean bias error was approximately +4 percent which indicates that equation (5.13) overestimated the actual value by 4 percent on average.

One problem associated with the use of equation (5.13) is an assumption connected with the way the weighting coefficients are determined. It will be recalled from Section 5.2.6 that the MMR channels were forced to account for the whole solar spectrum by extending the waveband limits. By doing so, the assumption is made that the reflectance in the unextended waveband adequately describes the reflectance in the extended waveband. This assumption is more nearly true in a case such as that displayed in extended waveband 6 (Fig. 5.4). However, for a case such as extended waveband 1 this is clearly not the case. Therefore, the weighting coefficients may not accurately weight the wavebands thereby leading to errors in the albedo estimation from equation (5.13).

73
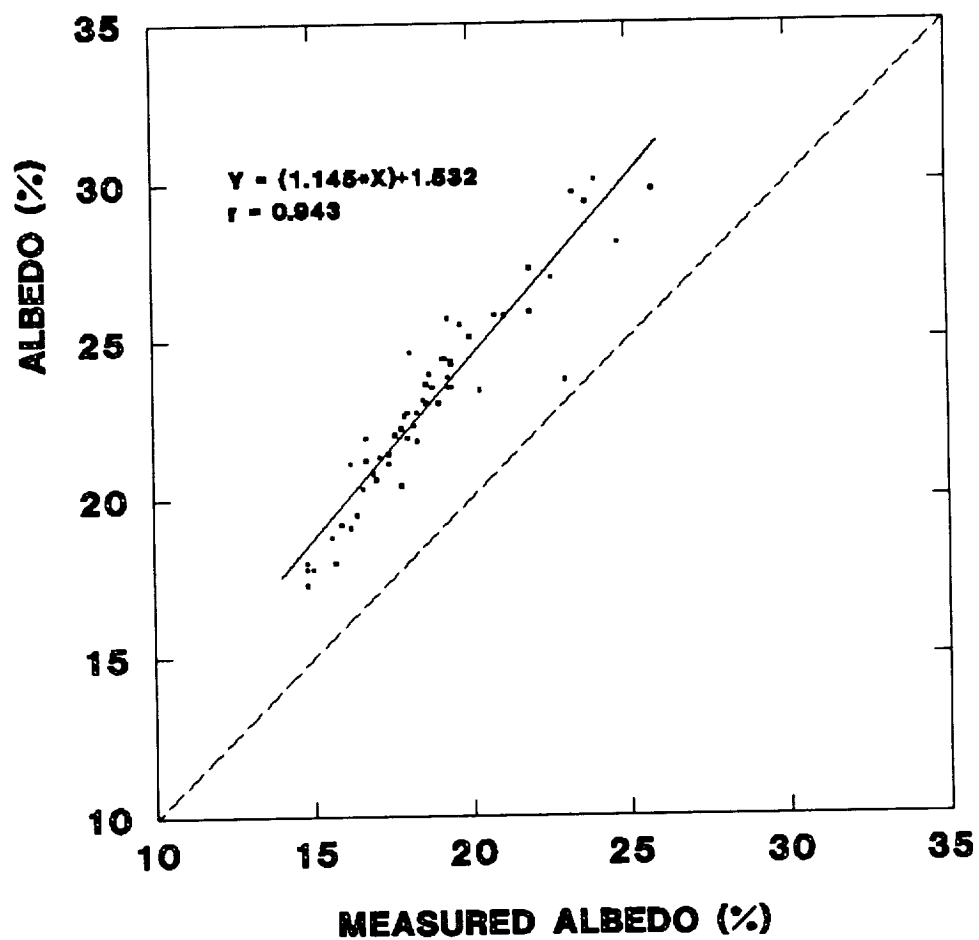
Figure 5.6 Comparison of measured albedo with albedo estimated from equation (5.13). Data acquired at Site 8 on day 155.

Due to the possible weighting coefficient problem and because the relative errors are too high for the purposes of this research, equation (5.13) was modified to include the incoming radiance as estimated from the field reference panel. This modification better describes the ratio of total solar radiation in each waveband to the total global radiation over the entire spectrum. Equation (5.13) was rewritten thusly:

$$\rho_{BB}(\theta_i) = \frac{\displaystyle\sum_{j=1}^{7} (RF_{Hj}) [Ref_j(\theta_i)] [W_j]}{\displaystyle\sum_{j=1}^{7} [Ref_j(\theta_i)] [W_j]} \tag{5.20}$$

where $Ref_j(\theta_i)$ is the reference panel radiance at nadir in MMR channel j in units of $[Wm^{-2} \mu m^{-1} sr^{-1}]$.

Recalling that a RF is the ratio of the canopy reflected radiance (RD_{Hj}) to the field reference panel reflected radiance (Ref_j) in a given channel, j, equation (5.20) reduces to

$$\rho_{BB}(\theta_i) = \frac{\pi \displaystyle\sum_{j=1}^{7} [RD_{Hj}(\theta_i)] [W_j]}{\pi \displaystyle\sum_{j=1}^{7} [Ref_j(\theta_i)] [W_j]} \tag{5.21}$$

where RD_{Hj} is a "hemispherical radiance" in units of $[Wm^{-2}\mu m^{-1}]$ and is calculated from the model of Walthall et al. (1985). The value of π is multiplied by the numerator and denominator which were originally in terms of $[Wm^{-2}\mu m^{-1}sr^{-1}]$. The model of Walthall et al. (1985)--equation (5.14)--was based upon the use of reflectance factors which has in its denominator the value of π (Swain and

75

Davis, 1978), which must be removed from equation (5.13). Attached to the value of π is the dimension of steradian [sr]. Therefore, the numerator and denominator will have the units of $[Wm^{-2}\mu m^{-1}]$.

Equation (5.21) may be more directly applicable to satellite data because, generally, satellite data are more easily converted into values of radiance than into RFs. Some work has been reported by Holm et al. (1989) in regards to converting Thematic Mapper data into RFs.

5.3.2 Evaluation of Equation (5.21)

Equation (5.21) was tested using the June 4, 1987 data set. Comparison of estimated albedo to the measured albedo proceeded in the same fashion as the comparison for equation (5.13). The average values for both the estimated and measured cases for the six data collection periods are depicted in Figure 5.7. The estimates of albedo exhibit the expected diurnal trend, but are lower than the measured values. Although the estimates made with equation (5.21) are nearer to the measured values than estimates made with equation (5.13), they are still not within one standard deviation of the measured value. The linear regression (Fig. 5.8) reveals an r of 0.965. This suggests that equation (5.21) estimates albedo fairly well.

Even though equation (5.21) appears to estimate albedo reasonably well, neither the numerator nor the denominator yield values of reflected or incoming shortwave radiation in units of Wm^{-2}. Rather, spectral flux densities $[Wm^{-2}\ \mu m^{-1}\ sr^{-1}]$ are obtained. Multiplying the hemispherical canopy radiance and field reference

76
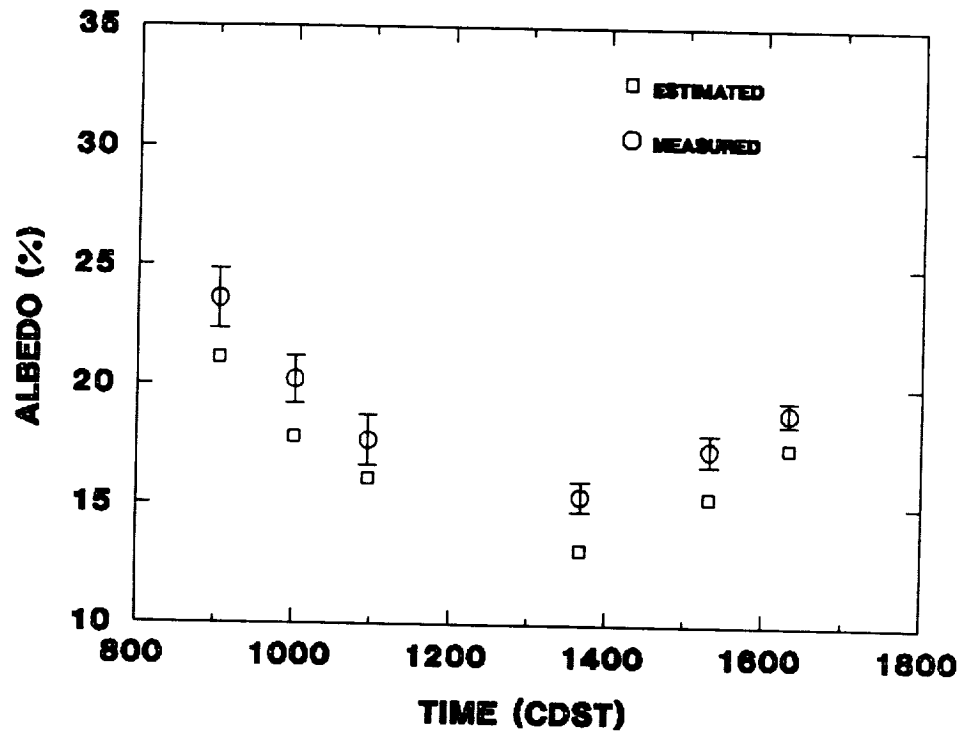
Figure 5.7 Comparison of mean measured albedo to mean albedo estimated from equation (5.21). Data acquired at Site 8 on day 155. Error bars indicate plus and minus one standard deviation.
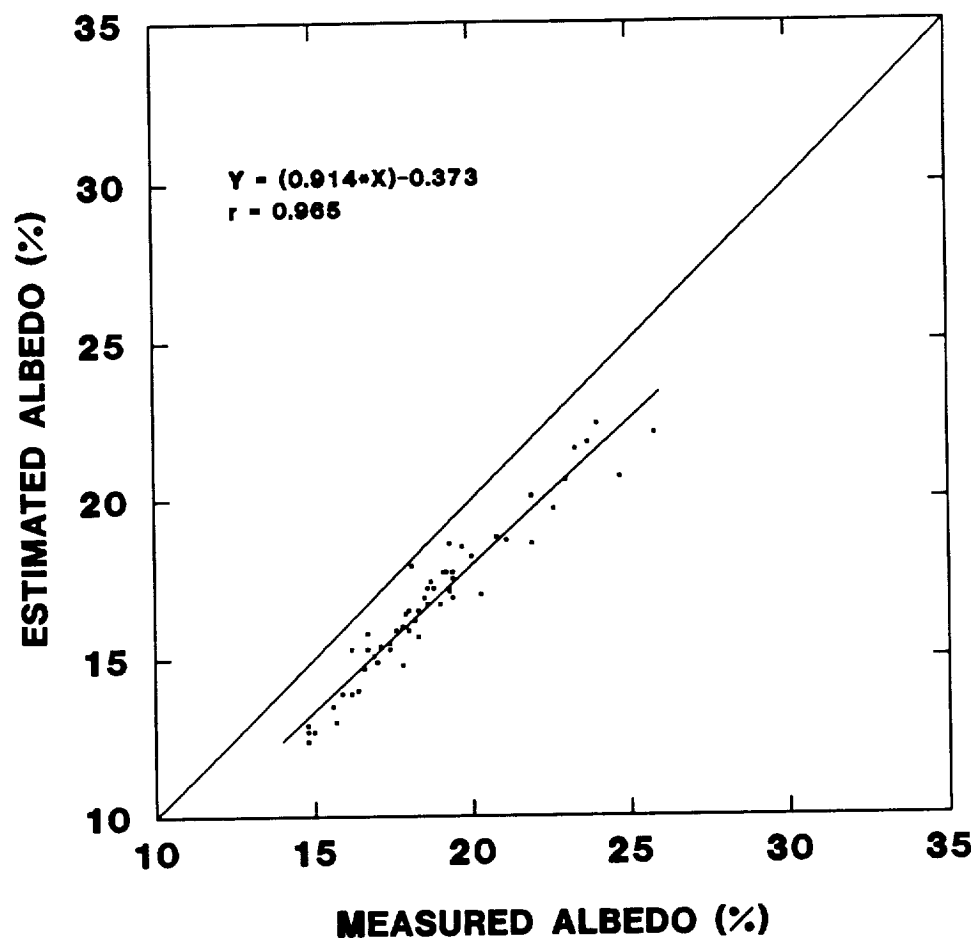
Figure 5.8 Comparison of measured albedo with albedo estimated from equation (5.21). Data acquired at Site 8 on day 155.

panel radiance by the bandwidth ($\Delta\lambda$) of the appropriate MMR channel (j) yields units in Wm^{-2}. Thus, equation (5.21) is written as

$$\rho_{BB}(\theta_i) = \frac{\pi \sum_{j=1}^{7} [RD_{Hj}(\theta_i)] [\Delta\lambda_j] [W_j/W'_j]}{\pi \sum_{j=1}^{7} [Ref_j(\theta_i)] [\Delta\lambda_j] [W_j/W'_j]} \qquad (5.22)$$

W'_j is the weighting coefficient for the unextended MMR wavebands, and this quantity compensates for the energy actually sensed by each channel for a given MMR.

5.3.3 Evaluation of Equation (5.22)

Equation (5.22) was tested with the June 4, 1987 data set. This equation produced estimates of albedo which are larger than the measured values (Figures 5.9, 5.10). In fact, the values obtained by use of equation (5.22) are almost the exact same values as those calculated from equation (5.13). Figure 5.11 is a plot of the values from equation (5.13) against those from equation (5.22). The values from both equations fall almost exactly along the 1:1 line, and the correlation coefficient is 0.982 suggesting that the two equations are very similar. These findings suggest that equations (5.13) and (5.22) may suffer from the same shortcomings.

5.3.4 Albedo Model Selection

Equations (5.21) and (5.22) will be evaluated for their ability to estimate albedo for the 1987 and 1988 data sets. Equation (5.13) will not be considered due to its similarity to the estimates from equation (5.22), and because it is generally easier

79
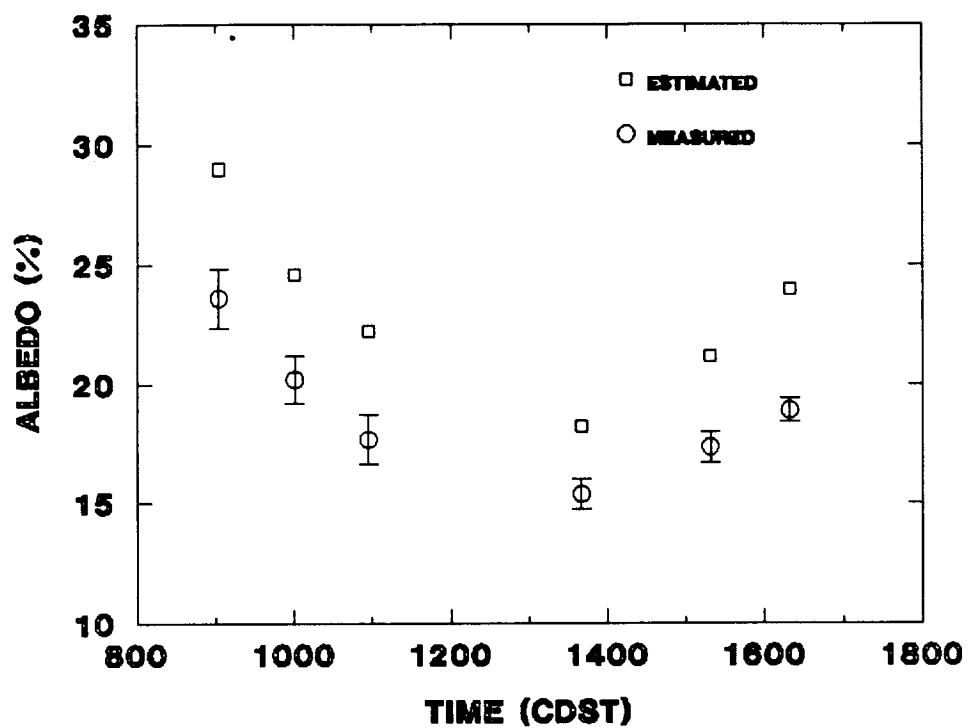
Figure 5.9 Comparison of mean measured albedo to mean albedo estimated from equation (5.22). Data acquired at Site 8 on day 155. Error bars indicate plus and minus one standard deviation.
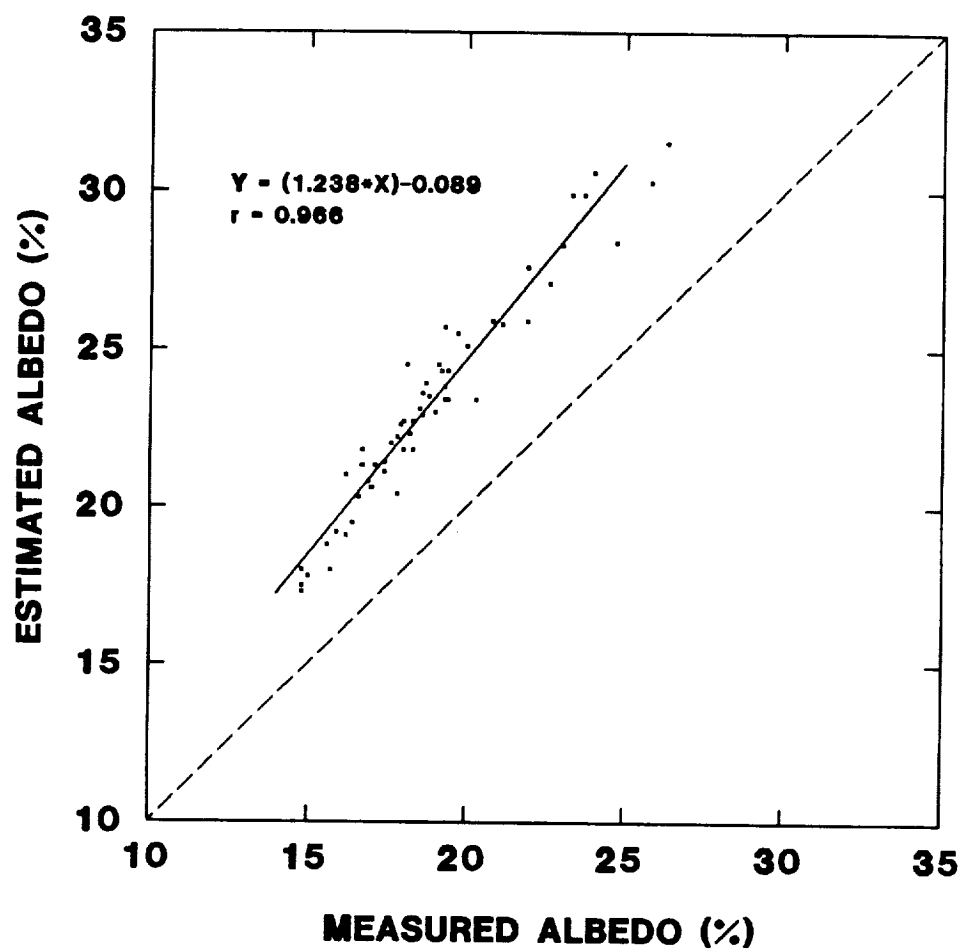
Figure 5.10 Comparison of measured albedo with albedo computed from equation (5.22). Data acquired at Site 8 on day 155.
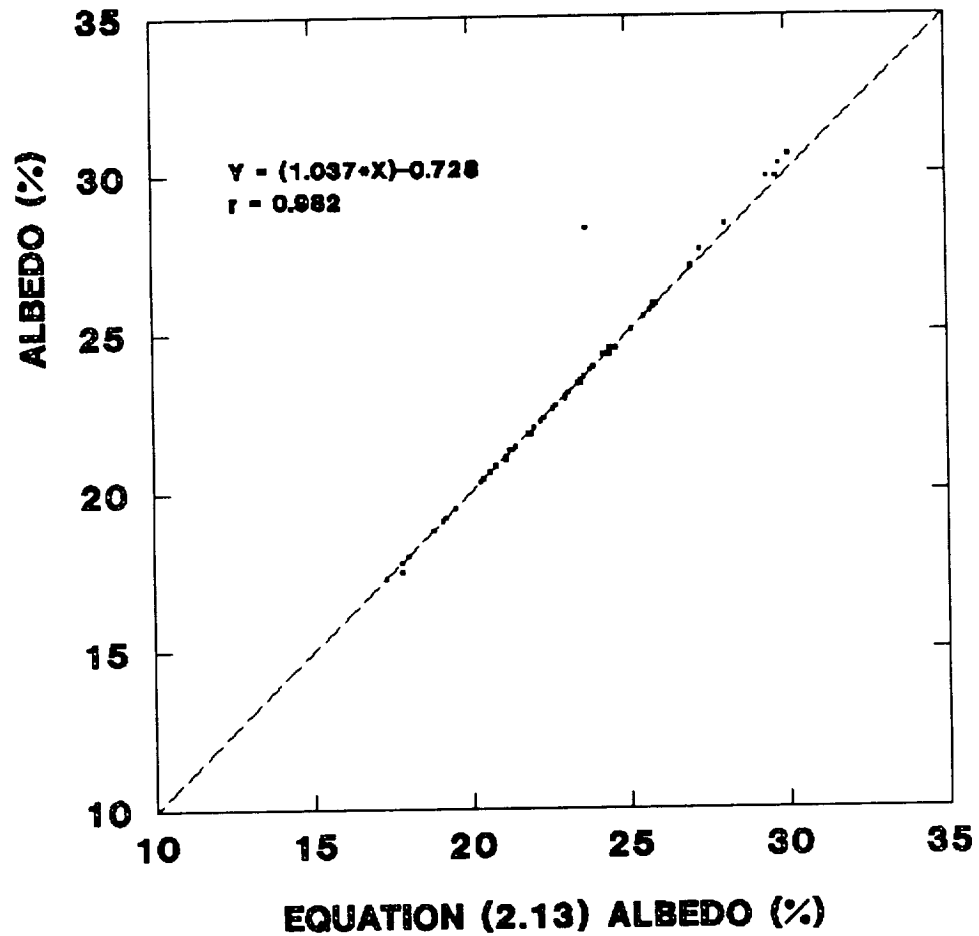
Figure 5.11 Comparison of estimated albedo computed from equation (5.13) with that computed from equation (5.22). Data acquired at Site 8 on day 155.

to convert the digital counts of satellite data to radiances than it is to reflectance factors.

5.3.5 Statistical Techniques

Typically, when estimates of a quantity are compared to actual measurements a linear regression is performed and indices such as Pearson's product-moment correlation coefficient (r) and its square, the coefficient of determination (r^2), are reported. From the least-squares regression the slope (m) and intercept (b) are determined so that a predicting equation may be written

$$P_{r\,i} = mX_i + b \qquad (5.23)$$

where X_i is the measured or observed value.

Willmott and Wicks (1980), Willmott (1981), and Willmott (1982) raised concerns about the exclusive use of r and r^2 in the context of model performance evaluation. Willmott (1981) noted that very dissimilar values of estimates and measurements can produce an r very near 1. Conversely, Willmott and Wicks (1980) stated that it was possible for small differences between the measured and estimated quantities to produce a low or even negative r. Thus, they stated that statistically significant values of r and r^2 may be misleading because they are often unrelated to the sizes of the differences between the estimates and measurements.

A relatively new statistical parameter, the "d" index of model agreement, was proposed by Willmott (1982). Used in conjunction with other common statistical measures, d aids in evaluating the performance or accuracy of models. Interpreted in much the same way as r, a d = 0 indicates complete disagreement between the estimated values and the measurements. A d = 1 indicates complete

83

agreement between the modeled values and measurements. For reference purposes d is written as

$$d = 1 - [\Sigma(E_i - M_i)^2 / \Sigma(|E_i - M| + |M_i - M|)^2] \qquad (5.24)$$

where

E_i = estimated value at time i
M_i = measured value at time i
M = mean of measured values for the data set

Equations (5.17), (5.19), (5.21), and (5.22) will be evaluated using least-squares regression, r, r^2, the root mean square error (RMSE), the mean square error (MSE), mean bias error (MBE), and the mean relative error (MRE). The MSE can be partitioned into systematic (MSE_s) and unsystematic (MSE_u) components

$$MSE = MSE_s + MSE_u \qquad (5.25)$$

where

$$MSE_s = N^{-1} \Sigma(P_{r\,i} - M_i)^2 \qquad (5.26)$$

$$MSE_u = N^{-1} \Sigma(P_{r\,i} - E_i)^2 \qquad (5.27)$$

and N is the number of data points. A RMSE, then, is simply the square root of MSE

$$RMSE = (MSE)^{0.5} \qquad (5.28)$$

and can be interpreted as the average total error in the estimating procedure. Average systematic errors (E_s) and unsystematic errors (E_u) are obtained from the square roots of MSE_s and MSE_u, respectively, and are in the same units as the measured and estimated values.

$$E_s = (MSE_s)^{0.5} \qquad (5.29)$$

$$E_u = (MSE_u)^{0.5} \qquad (5.30)$$

Unsystematic or random errors may occur because of unobserved, intermittent instrument problems, inconsistent data collection techniques, or random variations in the phenomena being measured.

84

Systematic errors may be assigned to consistent error in the experimental procedure or in the predicting equations. When E_s and E_u are summed they will not necessarily equal the RMSE. In fact, it is entirely possible that their sum may exceed the RMSE. This is due to the fact that the square root of a sum, such as the RMSE, is not necessarily equal to the sum of the square roots of the individual numbers. The unsystematic error can be visualized as a measure of clustering about a regression line drawn through a cloud of points. A large unsystematic error indicates that the data points are dispersed, whereas a small error would depict the cloud of points tightly clustered around the regression line. Systematic errors may be thought of as the distance from a one-to-one line to the regression line. If the distance is large there is a large systematic error, if the error is small the regression line will be located near the one-to-one line.

Mean bias error (MBE) describes the average error in the same units as the measurements.

$$MBE = N^{-1}\Sigma(E_i - M_i) \qquad (5.31)$$

Relative errors (RE) yield the percentage that E_i over- or under-estimates relative to M_i.

$$RE = (E_i - M_i)/M_i * 100 \qquad (5.32)$$

Mean relative error (MRE) is the average RE for a data set

$$MRE = N^{-1}\Sigma RE_i \qquad (5.33)$$

Other parameters such as the mean (Q), standard deviation (s), and coefficients of variation (cv) will also be reported. Standard deviations are calculated as

$$s = [(N-1)^{-1} \Sigma(V_i - Q)^2]^{0.5} \qquad (5.34)$$

85

where V_i is either the estimated or measured value and Q is the mean of the estimates or measurements in question. The coefficient of variation (cv) is a measure of relative variation.

$$cv = s/Q \qquad (5.35)$$

5.3.6 Model Performances (1987 Data)

Bidirectional reflectance data were obtained by the MMR on 27 days during 1987, for a total of 522 cases where the albedo estimates from equations (5.21) and (5.22) can be compared to the actual measurements. These 522 cases represent variations in plot topography, vegetative characteristics, and diurnal and seasonal effects. Therefore, the surface and time variations are expected to provide a good test for the albedo estimating algorithms.

Figures (5.12) and (5.13) are graphs of the estimated albedos versus the measured values for equations (5.21) and (5.22), respectively. When compared to the 1:1 line it is observed that most of the estimates from equation (5.21) are lower than the measured values, while those estimates from equation (5.22) are higher. Least squares regression was performed and the resulting predicting equations are noted on the graphs along with the regression line. In both instances, the slope of the line is positive indicating a positive linear relationship between the estimated and measured values. This slope value also indicates the increase in the estimate that is to be expected with a unit increase in the measurement (Yeates, 1974). Thus, for equation (5.21) a unit increase in the measured albedo produces an increase of 0.825 in the estimate. For equation (5.22) an increase of 1.082 is to be expected. It is also observed from the linear regression
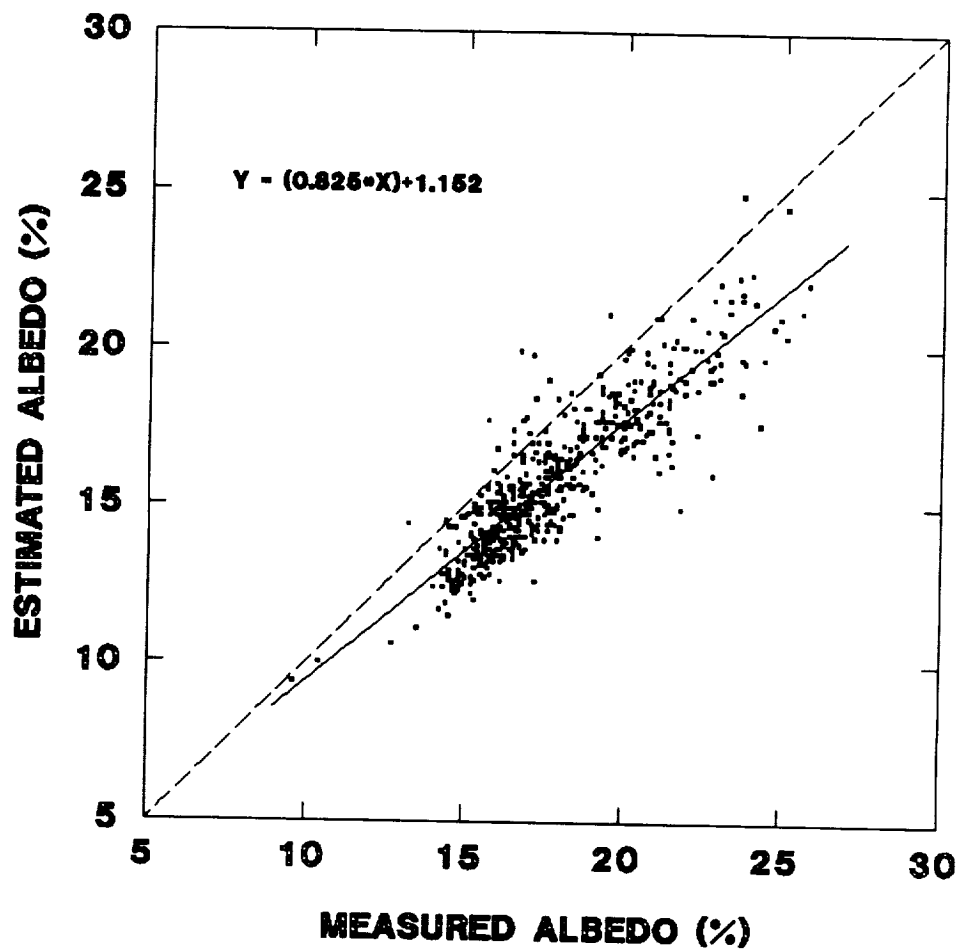
Figure 5.12 Comparison of measured albedo with albedo estimated from equation (5.21). 1987 data set (n = 522).
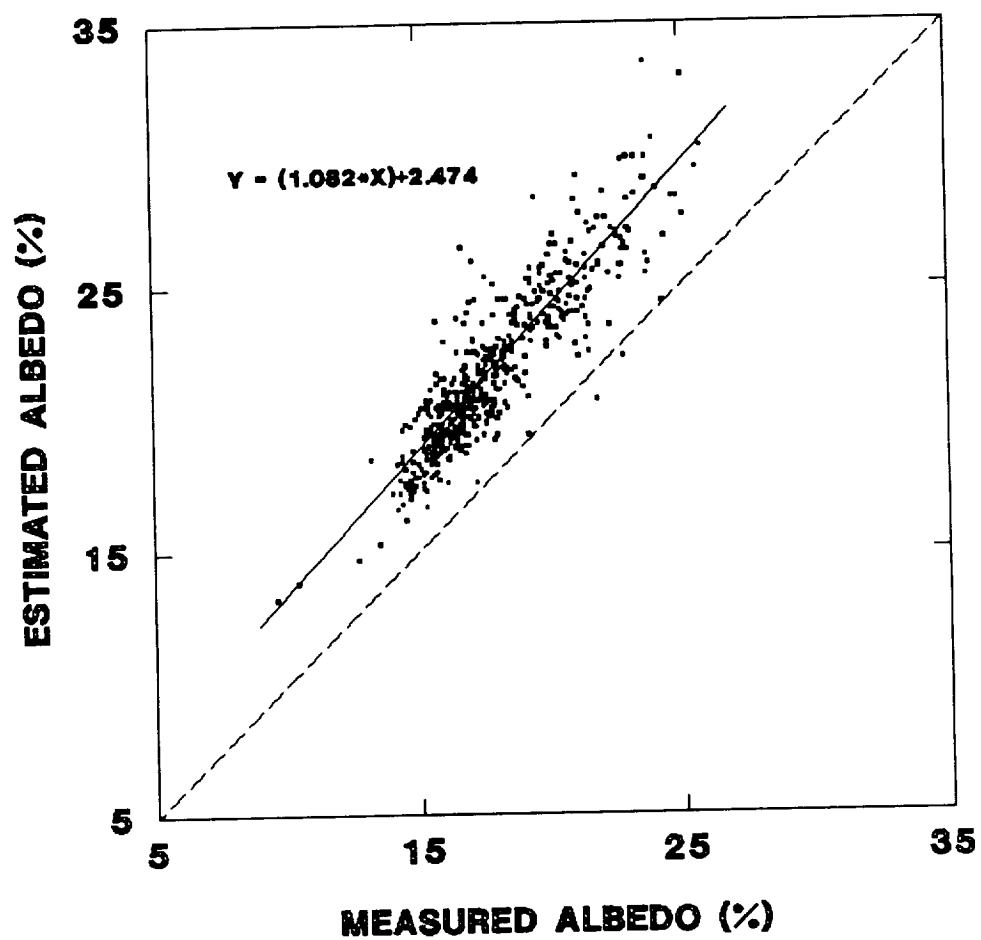
Figure 5.13 Comparison of measured albedo with albedo estimated from equation (5.22). 1987 data set (n = 522).

that the y-intercept for equation (5.21) is much lower than that for equation (5.22).

Table 5.2 contains the results of the statistical analysis for the two estimating equations. Pearson's product moment correlation coefficients for both equations are very similar and indicate a high degree of positive linear association between the estimates and measurements of albedo. The coefficients of determination suggest that both equations account for approximately 80 percent of the variance that occurs in the measured albedo. Although the r and r^2 values are similar

Table 5.2

Results of the statistical analysis
for equations (5.21) and (5.22)—
1987 data set.

Method	d	r	r^2	MBE	MRE	Q	s	cv	RMSE	Eu	Es
(5.21)	.806	.881	.776	-1.96	-10.88	15.9	2.36	0.15	2.3	1.1	2.0
(5.22)	.660	.894	.800	3.93	22.31	21.8	3.04	0.14	4.2	1.4	3.9
Meas.						17.8	2.51	0.14			

for both equations, the d index is not; corroborating Willmott's (1982) observation that r and r^2 do not always yield adequate information in regards to model performance. With a d index of 0.806 equation (5.21) is 14.6 percent more accurate than (5.22); but r suggests that (5.22) is slightly better than (5.21).

Further perusal of Table 5.2 indicates that the MBE for equation (5.21) is approximately -2 which means that the equation underestimates measured albedo, on average, by two percent. Equation (5.22) overestimates by four percent. Calculation of the

relative errors indicate that, on average, the values from equation (5.21) are approximately 11 percent too low relative to the measured value, and that those from (5.22) are 22 percent too high. Comparison of the cv's for the measured albedo and the two estimating equations show that the various methods account for approximately the same amount of variability. In regards to the RMSE, E_u, and E_s statistics we find that equation (5.21) exhibits a systematic error just a little larger than its unsystematic component and that the RMSE shows an average total error of approximately two percent. However, equation (5.22) displays a systematic error nearly twice the size of its unsystematic counterpart. Moreover, the systematic component makes up the largest part of the RMSE. Another way of visualizing the proportion of error attributed to the random and systematic components of error is to calculate the ratios MSE_u/MSE and MSE_s/MSE. For equation (5.21)

$$MSE_u/MSE = .238$$

$$MSE_s/MSE = .762$$

and for equation (5.22)

$$MSE_u/MSE = .106$$

$$MSE_s/MSE = .894$$

which indicates that systematic errors account for the largest proportion of the MSE in both models.

Willmott (1982) stated that differences described by E_s can be explained by a linear function, which implies that it should be relatively easy to reduce E_s by a new parameterization of the model. Without making significant changes to the structure of the model it should be possible to reduce E_s which implies that E_u can

90

be interpreted as a measure of potential accuracy. Applying this statement to the present circumstances, it appears that both estimating equations should be able to predict albedo to within approximately 1.5 percent of the measured value.

Table 5.3 is an enumeration of the relative errors calculated for each estimated albedo value for each equation. The table reinforces what the previous statistical analysis indicated; which is that equation (5.21) did a better job of predicting albedo and that the errors encountered with equations (5.22) are large.

Table 5.3

Tabulation of the number and percentage
of relative errors in a particular error
category for equations (5.21) and (5.22).

Method	≤5%	>5≤10%	>10≤15%	>15≤20%	>20≤25%	>25%	
(5.21)	66	138	180	118	15	5	#
	(12.6)	(26.4)	(34.5)	(22.6)	(2.9)	(1.0)	%
(5.22)	6	17	64	125	150	160	#
	(1.2)	(3.3)	(12.3)	(24.0)	(28.7)	(30.7)	%

5.3.7 Model Performances (1988 Data)

Bidirectional data were acquired at site 18 on seven days during the summer of 1988, yielding 64 cases for comparing estimates of albedo to measured values. During 1988 MMR #108 was used to collect the bidirectional data; during 1987 MMRs #103 and #128 were used. Unlike the MMRs employed during 1987, the spectral responses in each of the seven reflective wavebands were not available for MMR #108. These filter functions are necessary in order to determine the upper and lower limits of each band, which are required for the calculation of W'_j for use in equation (5.22).

91

Because the filter function information was not available for MMR #108, it was decided to use the weighting coefficients from MMR #103.

With the above in mind, albedos from MMR #108 data were calculated and compared to the measured values (Figs. 5.14 and 5.15). Equation (5.21) slightly underestimates while equation (5.22) overpredicts the measured value. Slopes from the linear regression indicate that both equations possess a positive linear relationship with the measured data. Equation (5.21) has a y-intercept close to zero while that from equation (5.22) is slightly greater than one.

Table 5.4 contains the results of the statistical analysis for the 1988 data set. As with the 1987 data set the r values seem to indicate that the models perform well. Additionally, r^2 indicates that both models account for 70 percent of the variability exhibited by the measured values.

Table 5.4
Results of the statistical analysis
for equations (5.21) and (5.22)—
1988 data set.

Method	d	r	r^2	MBE	MRE	Q	s	cv	RMSE	Eu	Es
(5.21)	.97	.84	.70	-.91	-5.74	14.9	1.88	.13	1.35	1.00	0.91
(5.22)	.78	.84	.71	4.35	27.55	20.2	2.38	.12	4.45	1.27	4.27
Meas.						15.8	1.68	.11			

The d values show that both models performed well. Inspection of the MBEs reveals that equation (5.21) underestimates by about one percent, and (5.22) overestimates by approximately four percent. Mean relative errors reveal that equation (5.22) overestimate 28
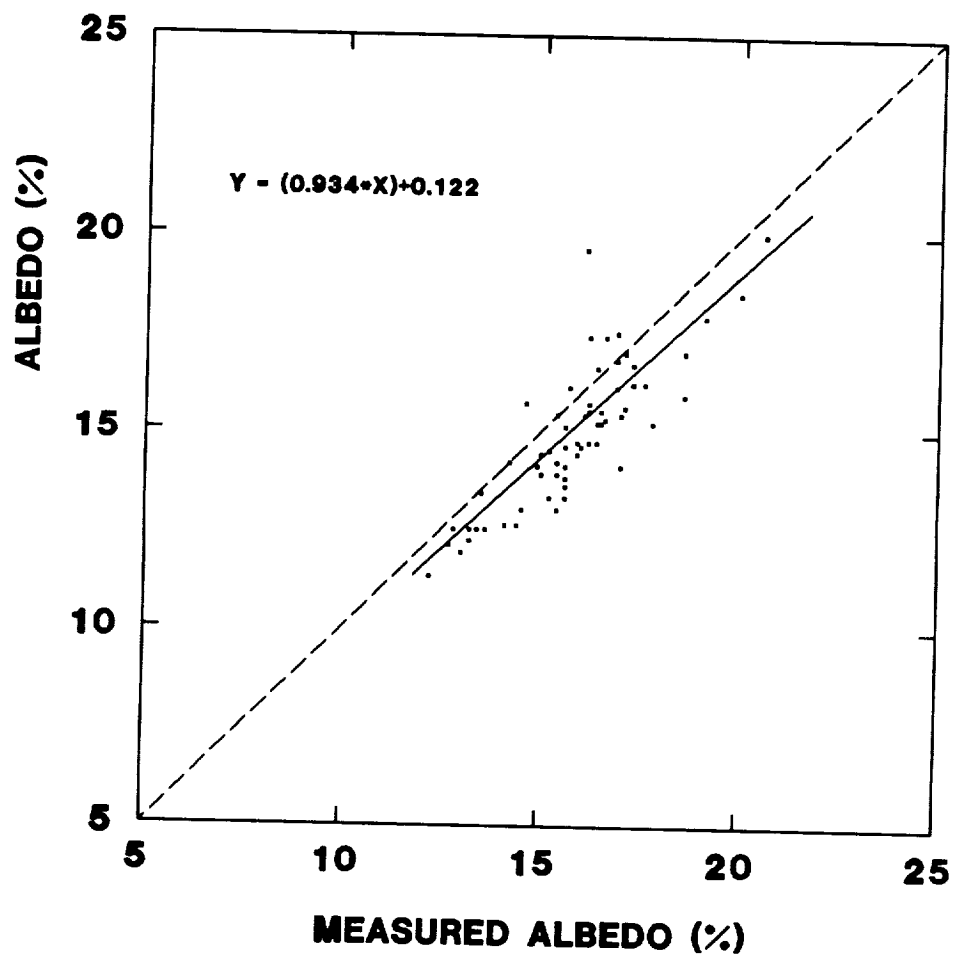
Figure 5.14 Comparison of measured albedo with albedo estimated from equation (5.21). 1988 data set (n = 64).
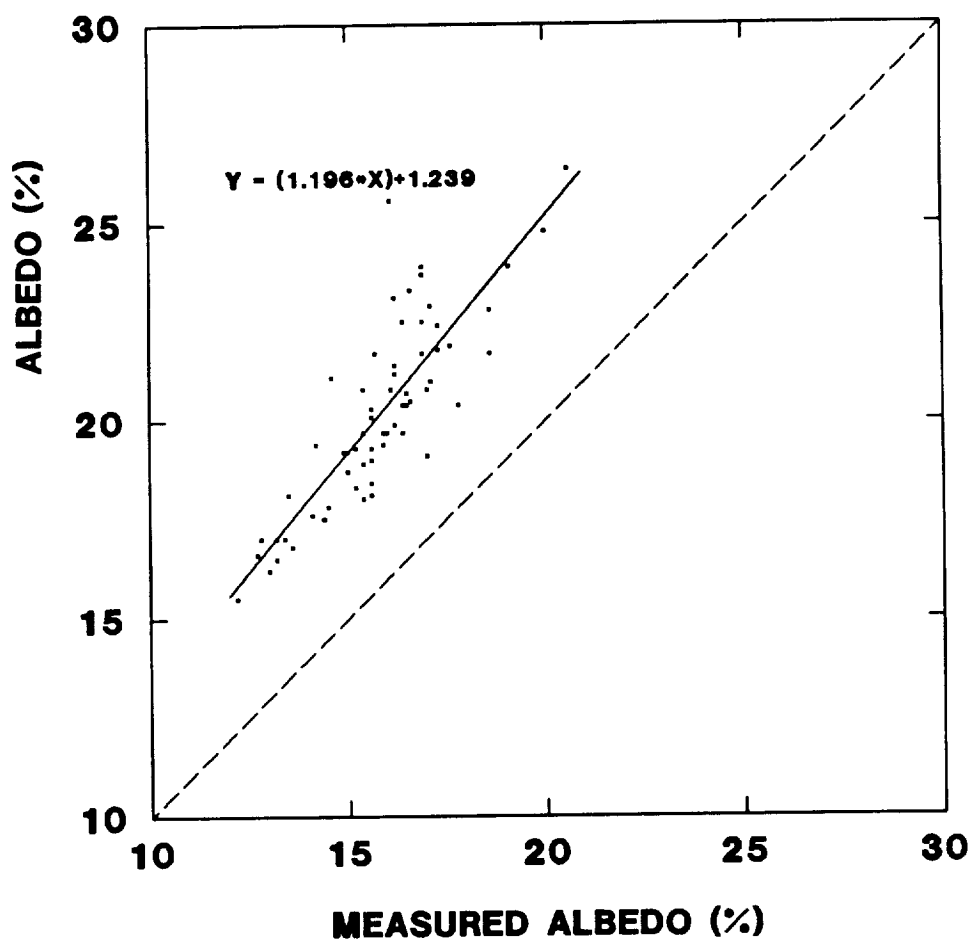
Figure 5.15 Comparison of measured albedo with albedo estimated from equation (5.22). 1988 data set (n = 64).

percent, while (5.21) underestimates by about 6 percent. The RMSE, E_u, and E_s from the 1988 data set are comparable to those of the 1987 data set.

5.3.8 Incoming Shortwave Radiation Models Performance (1987 Data)

Figures 5.16 and 5.17 are scatterplots of the measured values of incoming shortwave radiation versus the estimates computed from equations (5.17) and (5.19), respectively.

$$ISW_e - \pi \sum_{j-1}^{7} (Ref_j) (\Delta\lambda_j) / (P/T) \qquad (5.17)$$

$$ISW_e - \pi\Sigma (Ref_j) (\Delta\lambda_j) (W_j/W'_j) \qquad (5.19)$$

It is noted from the graphs that both equations produce similar estimates of incoming solar radiation. The linear regression equations exhibit comparable slopes and y-intercepts. Both slopes show a strong positive linear relationship between the measured and estimated values. For a unit change in the measured value there is a corresponding change of 0.91 in the estimated value. Additionally, both techniques show the y-intercept to be approximately 33 Wm^{-2}.

Table 5.5 contains the results from the statistical analysis of the two incoming solar radiation models.
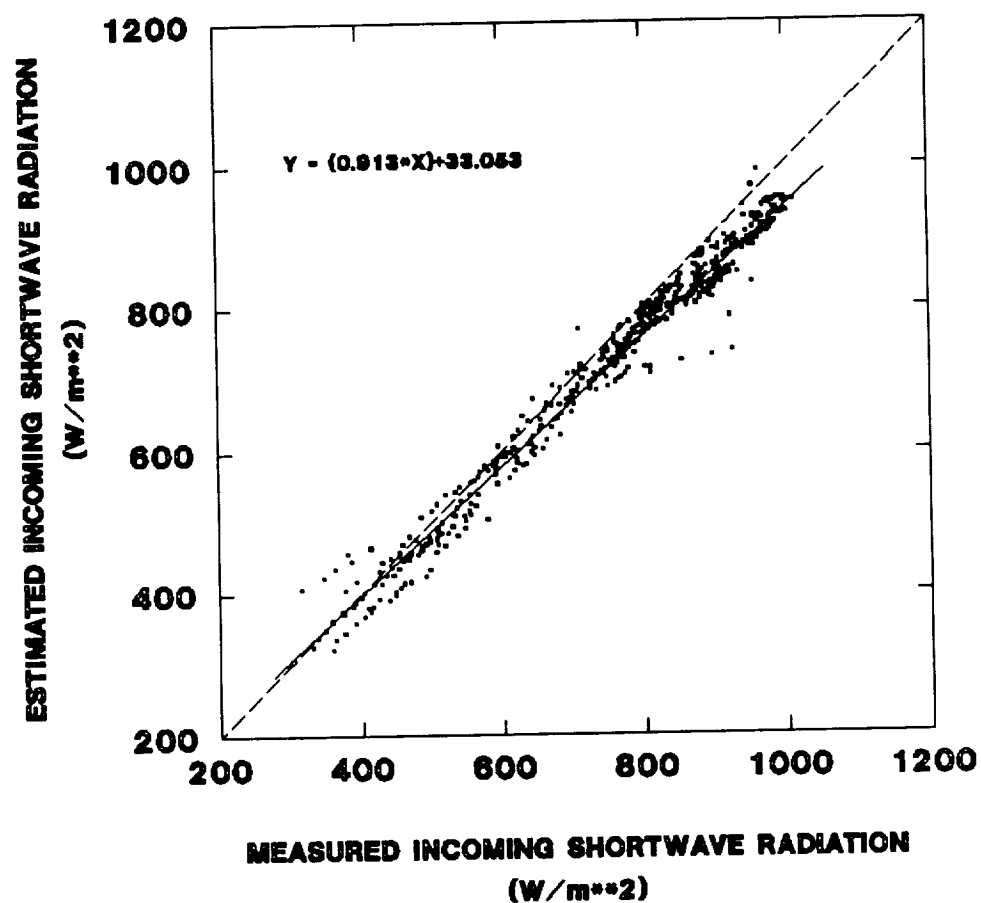
Figure 5.16   Comparison of measured incoming
shortwave radiation with incoming shortwave
radiation estimated from equation (5.17).   1987
data set (n = 522).
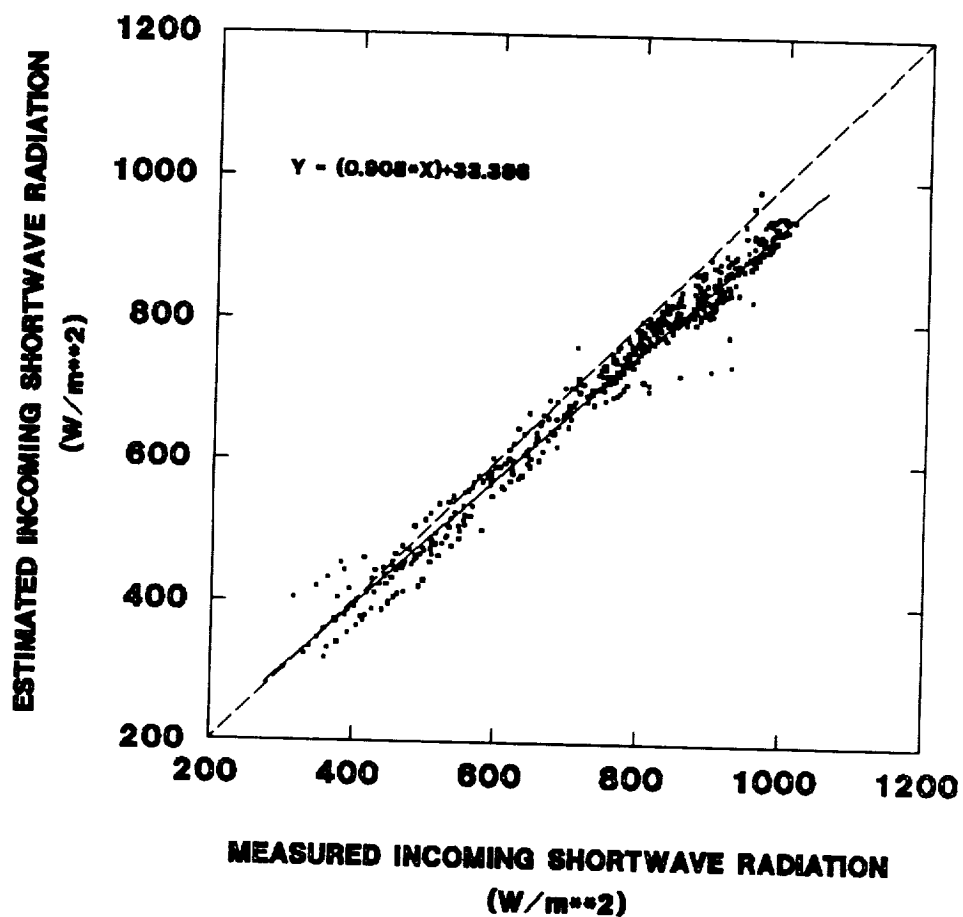
Figure 5.17 Comparison of measured incoming
shortwave radiation with shortwave radiation
estimated from equation (5.19). 1987 data set
(n = 522).

Table 5.5

Results of the statistical analysis
for equations (5.17) and (5.19)—
1987 data set.

Method	d	r	r^2	MBE	MRE	Q	s	cv	RMSE	Eu	Es
(5.17)	.980	.989	.978	−37.6	−4.6	730.3	161.47	.22	47.22	24.1	40.6
(5.19)	.983	.989	.978	−33.4	−4.0	734.5	162.51	.22	44.25	24.2	37.1
Meas.						767.9	175.92	.23			

The r value for both models are high and equal, which indicates that the estimates of incoming shortwave radiation have a positive linear association with the measured values. The r^2 values mean that both models account for 99 percent of the variation contained within the measurements. Values of d suggest that both models performed well for the 1987 data set and that equation (5.19) provides 0.3 percent more accuracy than the model of Jackson.

Measured incoming shortwave averaged 767.9 Wm^{-2} over the 522 cases, and the average value was 730.3 Wm^{-2} and 734.5 Wm^{-2} for equations (5.17) and (5.19), respectively. The MBE for Jackson's model was −37.6 Wm^{-2}, and for equation (5.19) it was −33.4 Wm^{-2}. This indicates that both methods underestimated the measured value. Mean relative errors (MRE) for both models were less than five percent. Standard deviations and coefficients of variation substantiate the fact that the models are not very different from each other in terms of the results each produces. RMSEs exhibit average total errors on the order of 44 to 48 Wm^{-2}. The systematic error component for the Jackson model is approximately 41 Wm^{-2}, while that for equation (5.19) is 37 Wm^{-2}. Random error accounts for 24 Wm^{-2} in both models. This information coupled with the systematic error suggests that both techniques can be improved so

that future estimates of incoming shortwave radiation may be within 25 Wm^{-2} of the measured value.

5.3.9 Incoming Shortwave Radiation Models Performance (1988 Data)

The 1988 data set had only 67 cases of measured incoming solar radiation available for comparison with the modeled results. Figures 5.18 and 5.19 are the scatterplots of the measured values versus the estimates from the model of Jackson and equation 5.19, respectively. From these graphs it is observed that both equations, in general, slightly overestimate the measured value.

Statistical analysis (Table 5.6) reveals that the r and r^2 values indicate that both models performed very well.

Table 5.6
Results of the statistical analysis
for equations (5.17) and (5.19)—
1988 data set.

Method	d	r	r^2	MBE	MRE	Q	s	cv	RMSE	Eu	Es
(5.17)	.98	.97	.95	9.9	1.6	828.2	95.39	.12	30.22	21.33	21.41
(5.19)	.98	.97	.95	8.1	1.4	826.4	95.39	.12	29.09	20.85	20.29
Meas.						818.3	112.01	.14			

The d statistic is also very high meaning that the models did perform as well as r and r^2 suggest. According to the MBE, both models overestimated the measured incoming solar radiation by 8 to 10 Wm^{-2}, and the MRE shows that the amount overestimated is approximately 1.5 percent of the measured value. Mean values of incoming shortwave radiation are nearly the same for both models. The RMSE is about 30 Wm^{-2} for both models. Systematic and unsystematic error are nearly the same for both equations.
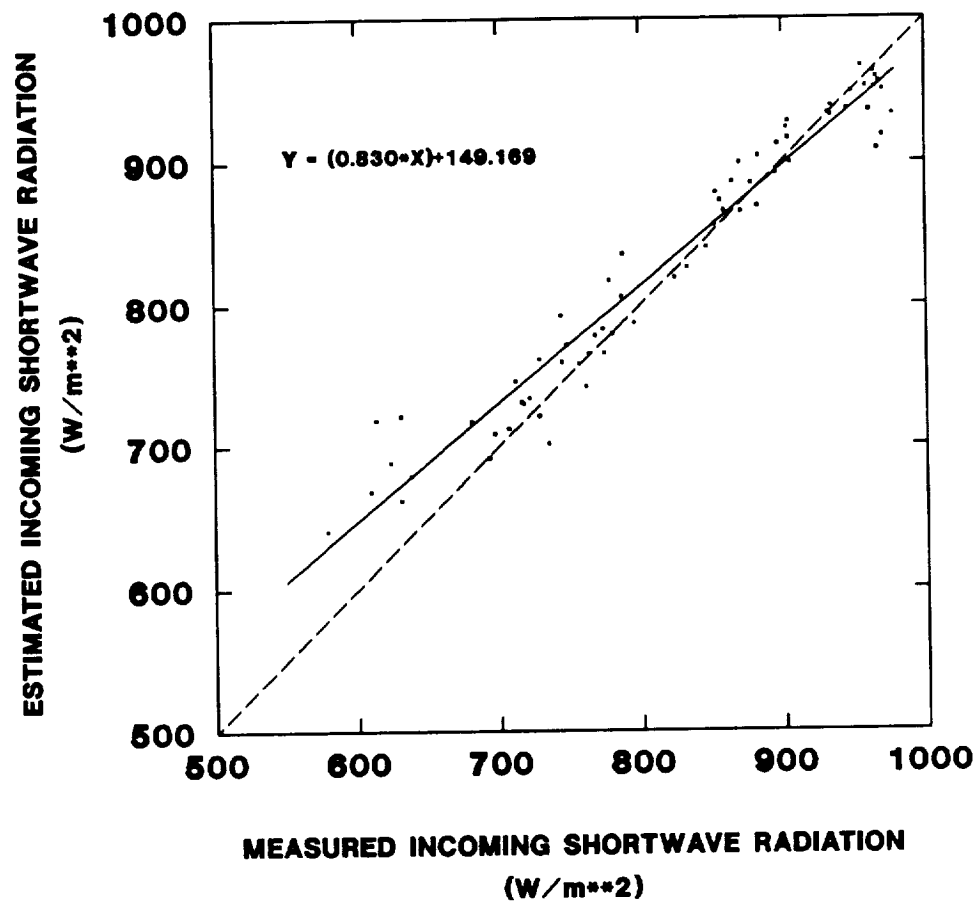
Figure 5.18 Comparison of measured incoming shortwave radiation with incoming shortwave radiation estimated from equation (5.17). 1988 data set (n = 67).

The plot shows ESTIMATED INCOMING SHORTWAVE RADIATION (W/m**2) on the y-axis (ranging 500 to 1000) versus MEASURED INCOMING SHORTWAVE RADIATION (W/m**2) on the x-axis (ranging 500 to 1000).

$Y = (0.833*X)+144.835$
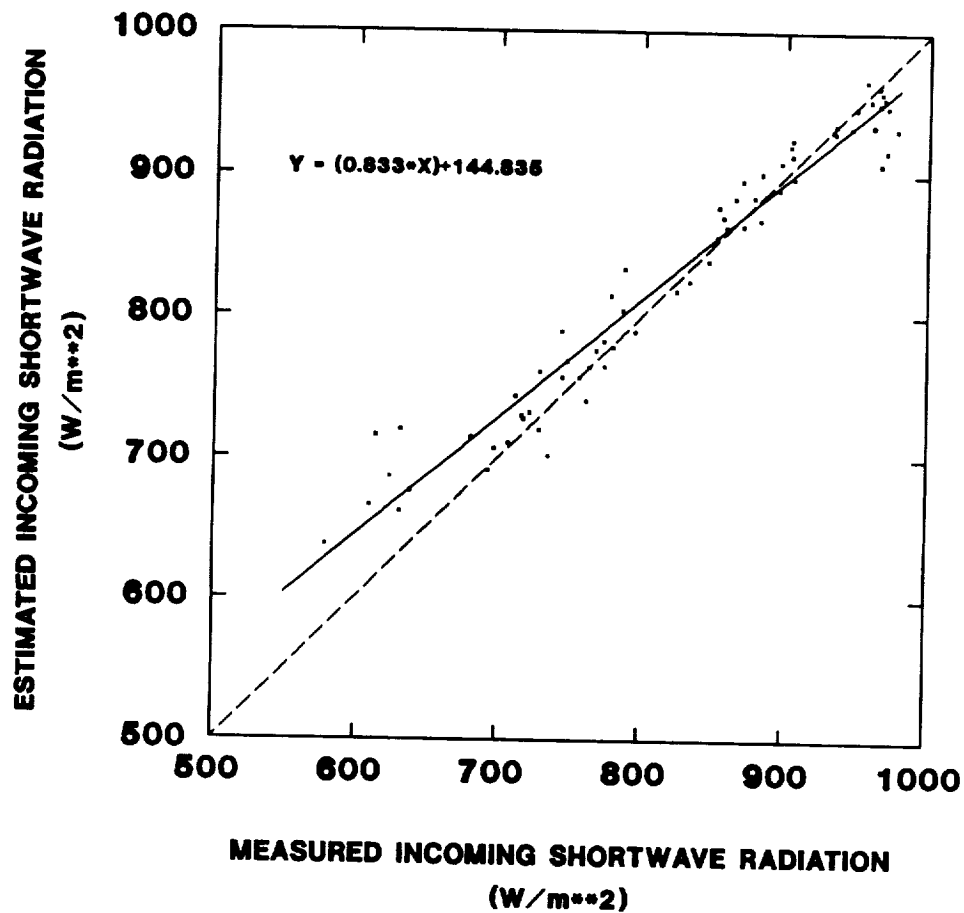
Figure 5.19 Comparison of measured incoming shortwave radiation with incoming shortwave radiation estimated from equation (5.19). 1988 data set (n = 67).

101

5.4 Summary and Conclusions

Estimates of albedo were produced from equations (5.21) and (5.22) using bidirectional reflectance data acquired during 1987 and 1988. Although statistical analyses reveal that equation (5.21) performed better in both years, its use is cautioned. This caution is based upon uncertainties that lie in the separate calculation of the numerator and denominator of equation (5.21). The values obtained from the calculation compare well to the pyranometer values. However, the pyranometer values have units of $[Wm^{-2}]$ whereas the units attached to the component parts of equation (5.21) are in units of $[Wm^{-2}\mu m^{-1}]$. It is not clear at this point why the values compare so well and yet the units are different. Therefore, it simply may be fortuitous that equation (5.21) works as well as it does.

Equation (5.22) accounts for the μm term, and it also estimates albedo reasonably well. Statistical analysis of the equation shows that there was a large systematic error associated with both the 1987 and 1988 data sets. This finding suggests that changes in the model should reduce the systematic error. It is probably inappropriate to use the weighting coefficients, developed above, in the numerator of equation (5.22) for they are computed from a solar irradiance curve at the earth's surface and not from reflectance curves. The albedo model should be improved through the use of weighting coefficients for the numerator of the equation based upon vegetative reflectance characteristics as Jackson (1984) had done for wheat and bare soil. A variety of vegetative surface types should be evaluated for their effects on the calculation of the weighting coefficients.

102

Systematic error may be induced from use of the hemispherical reflectance model of Walthall _et al._ (1985), which extrapolates the off-nadir reflectance data out to 90°. The extrapolation process may introduce errors not obvious to the user. It is not known at this point if there is a problem with the model, but it should be investigated.

An additional source of error in the albedo calculations may be induced by the so-called "hot-spot." The hot-spot is an anomalously bright region of reflectance located in the principal plane of the sun (Suits, 1972). It is possible that one of the viewing angles of the MMR is recording some of the hot-spot information yielding reflectance values that are too high, thereby increasing the albedo. Evaluation of the hot-spot contribution should be undertaken with reference to equation (5.22) by using data obtained out of the sun's principal plane, or by using data in the principal plane not near the hot-spot angle.

The approach of Jackson (1984) yields estimates of albedo to within approximately five percent of the measured value. However, Jackson's method uses data acquired at nadir only and does not account for surface anisotropy. It simply may be fortuitous that his method works as well as it does. The method proposed here takes into account known surface anisotropy. It is anticipated that by accounting for the other concerns mentioned above that equation (5.22) will be useful in producing reliable estimates of albedo.

Equation (5.21) produces reasonable estimates of albedo, but its use is discouraged owing to problems associated with the units attached to the numerator and denominator of the equation. Further

103

investigation into this equation and how it works may prove enlightening.

Incoming shortwave radiation models (eqs. 5.17 and 5.19) performed very well for both the 1987 and 1988 data sets. Statistical analysis indicates that the mean relative errors for both data sets is less than 5 percent, and that the average total error to be expected is less than 50 Wm^{-2}. Equation (5.19) was evaluated to be slightly better than the algorithm developed by Jackson (1984). However, either may be used to obtain reliable estimates.

6. ESTIMATION OF LONGWAVE RADIATION STREAMS

6.1 Introduction

The sun emits relatively little energy past 4.0μm. However, some of the solar energy which strikes the earth's surface is absorbed and converted into heat. Some of this heat is radiated to the atmosphere as longwave radiation. Some of the radiated longwave is lost directly to space, but a large portion is captured by water vapor, carbon dioxide, and ozone and reradiated to the earth. Atmospheric gases, then, provide a source of incoming longwave radiation (Rl↓) to the earth's surface. The surface is a source of emitted longwave radiation (Rl↑).

Several terms are used as synonyms for longwave radiation, of which Miller (1981) offered some comments:

> Longwave radiation is sometimes called "atmospheric" radiation because it is emitted by the atmosphere. At other times it is referred to as "terrestrial" radiation to contrast it with solar radiation; however, then it is likely to be confused with the upward flux of longwave from the earth's surface. The term "nocturnal" radiation is sometimes used because longwave is more easily measured at night, but it is also larger than the short-wave component during daylight hours. Longwave radiation is also termed "thermal" because its effects are primarily heating.

In this report the term longwave radiation will be used along with the direction of the flux.

Variations in the downward flux of longwave radiation occur both spatially and temporally. Miller (1981) lists five time scales over which these variations may occur: i) momentary variations which result from clouds passing over an area and thereby increasing the flux; ii) diurnal variations which run parallel to the input of solar radiation; iii) interdiurnal variations which result from changes in atmospheric warmth,

moisture, and cloud content; iv) annual variations which are due to differences in the heating and moistening of the lower troposphere in accordance with the march of the seasons; and v) year-to-year variations which occur along with synoptic weather systems which affect such parameters as cloud cover and air temperature.

Spatial variations in the incoming longwave also occur and may be observed on the micro-, meso-, altitudinal, and global scales. As an example of microscale variation, Miller (1981) related observations obtained by Reifsnyder in a red pine stand. At the top of the stand a longwave flux of 335 Wm^{-2} was observed, while within the pine stand, at ground level, a value of 395 Wm^{-2} was recorded. Differences in altitude also effect spatial variation due to the variations in air temperature and humidity.

Time and spatial variations in outgoing longwave radiation are affected by surface type and solar input. Differing surfaces may have differing emissivities which influence the ability of the surface to radiate longwave energy.

6.1.1 Outgoing Longwave

Some of the solar energy incident upon a surface is absorbed by that surface and converted into heat. When a thermometer is placed in contact with a surface, that surface's kinetic temperature is measured. Kinetic temperature is a manifestation of the average translational energy of the molecules comprising the object being measured. According to the Stefan-Boltzmann law, a surface will emit energy as a function of its emissivity (ϵ) and temperature. When this energy is measured remotely (e.g. by a thermal scanner) one measures the radiant or apparent temperature

(Lillesand and Kiefer, 1979). As Lillesand and Kiefer (1979) point out, because of emissivity differences, earth surface features can have the same temperature but have very different radiant emittances. Neglecting reflected longwave radiation, the radiant temperature (T_{rad}) of an object is related to its kinetic temperature (T_{kin}) by

$$T_{rad} = \epsilon^{1/4}T_{kin}$$ (6.1)

With the advent of thermal infrared scanners and handheld infrared thermometers, several studies have been conducted to measure plant canopy temperatures, surface emissivity, plant stress, and to map surface temperature (Fuchs and Tanner, 1966; Rao, 1972; Nixon et al., 1974; Blad and Rosenberg, 1976; Cogan and Willand, 1976; Idso et al., 1976; Pinter and Reginato, 1982; Jackson, 1983; Jackson et al., 1983b; Pinter, 1983; Hatfield et al., 1984; Reginato and Howe, 1985;). Canopy and soil surface temperatures have been utilized as inputs into models used to calculate evapotranspiration (Conaway and van Bavel, 1967; Wiegand and Bartholic, 1970; Heilman et al., 1976; Soer, 1980; Carlson et al., 1981; Walsh and Stadler, 1983; Klaassen and van den Berg, 1985; Reginato et al., 1985). Radiation at a particular wavelength impinging upon a surface may be absorbed and/or reflected and/or transmitted. The absorptivity of a surface at some temperature is equal to its emissivity (Elachi, 1987). For most remote sensing applications, earth surface features are assumed to be opaque to thermal radiation so that its transmissivity is equal to zero (Lillesand and Kiefer, 1979). Therefore, for thermal wavelengths we may write

$$\epsilon(\lambda) + r(\lambda) = 1$$ (6.2)

This equation indicates that there may be a reflected component of longwave energy from a surface. Thus, Fuchs and Tanner (1966) partitioned the upward flux of longwave radiation in the following way

$$Rl\!\uparrow = \epsilon\sigma T^4 + (1-\epsilon)B^* \qquad (6.3)$$

where B^* is equal to $Rl\!\downarrow$ (incoming longwave).

For the purposes of this report, the reflected and emitted component of outgoing longwave will not be separated from each other.

6.1.2 Incoming Longwave

Elsasser (1942) and Robinson (1950) provide examples of graphical techniques for acquiring the incoming flux of longwave radiation. Radiation charts produced by others may be found in Coulson (1975, p.270). Elsasser's chart requires that atmospheric profiles of humidity and temperature be known so that the longwave flux may be determined. Details on the use of radiation charts may be found in Sellers (1965), Sutton (1953), Goody (1964), Haltiner and Martin (1957), and Liou (1980). In general, these charts differ little from one another (Sellers, 1965), and are somewhat cumbersome to use even when the appropriate inputs are available.

Several researchers have developed empirical and/or theoretical formulae to calculate incoming longwave radiation. These formulae require that one or more of the following be known: i) fraction of cloud cover, ii) air temperature at shelter height, iii) vapor pressure at shelter height, iv) elevation of surface above mean sea level, and v) incident solar radiation. Because

data were only obtained under clear skies, the discussion here will be limited to clear sky models.

Brunt (1932) produced a simple algorithm whereby the downward flux of radiation is a function of the air temperature (T) in degrees Kelvin and the actual vapor pressure (e_0) in millibars [mb]

$$Rl\downarrow = \sigma T^4(a+be_0^{1/2}) \tag{6.4}$$

where "a" and "b" are constants. According to Hatfield et al. (1983), the coefficients in the Brunt formula are usually determined for local conditions. However, they used values found by Brunt for the northern hemisphere to give

$$Rl\downarrow = (\sigma T^4)(.51+0.06e_0^{1/2}) \tag{6.5}$$

Monteith (1961), in an effort to redefine the constants of the Brunt formula found that his value for emissivity was

$$\epsilon = 0.53 + 0.065e_0^{1/2} \tag{6.6}$$

which is a form of the Brunt equation and not very different than that of equation (6.5).

Brutsaert (1975) analytically derived an equation (6.7) for atmospheric emissivity which was used to estimate clear-sky incoming longwave radiation.

$$Rl\downarrow = (\sigma T^4)[1.24(e_0/T)^{1/7})] \tag{6.7}$$

Swinbank (1963) believed that the importance of water vapor's contribution to longwave radiation was exaggerated. With this premise in mind, he developed an equation to estimate incoming longwave radiation based only on temperature. This equation is

$$Rl\downarrow = (5.31 \times 10^{-14})(T^6) \tag{6.8}$$

Equation (6.8) was developed from approximately 100 observations obtained under clear skies on a total of 18 days in November/ December 1961 and June/July 1962. The observations of dry-bulb

temperature, vapor pressure, and measured incoming longwave were obtained soon after dark to ensure that the screen-level temperature was representative of the atmosphere. Swinbank's work has received some criticism for being too empirical and not taking into account a wider range of atmospheric conditions (Discussion, 1964), among other concerns.

Deacon (1970) showed that equation (6.8) could be derived from the knowledge of atmospheric emission. Additionally, Deacon suggested that the value obtained from equation (6.8) should be adjusted to account for atmospheric pressure at the point of observation. This correction takes the form

$$Rl\downarrow = R_s - 0.035(z/1000)\sigma T^4 \tag{6.9}$$

where R_s is the value obtained from equation (6.8) and z is the height of the station above mean sea level in meters.

Paltridge (1970) further suggested that the values obtained from the formula of Swinbank would be too high during the day because of a bias in Swinbank's model towards inversion conditions. Comparison of measured incoming longwave to values derived from equation (6.8) led Paltridge to state that it overestimated by about 30 Wm^{-2} for hourly averages.

Idso and Jackson (1969), like Swinbank, developed a procedure for calculating incoming longwave based only upon screen-level air temperatures. Their equation, however, was more theoretically based than that of Swinbank and was developed to accommodate a wider range of air temperatures. Idso and Jackson wrote their equation thusly,

$$Rl\downarrow = \sigma T^4[1-c(exp-d(273-T)^2)] \tag{6.10}$$

where c = 0.261 and d = 7.77 x 10^{-4}.

110

Aase and Idso (1978) compared equation (6.10) to the formula of Brutsaert for the purpose of evaluating the performance of each at temperatures lower than 0° C. Using daily averages of air temperature and humidity obtained at Sidney, Montana it was observed that the Brutsaert method always underestimated the true value while that of Idso and Jackson underestimated, matched, and then overestimated as the air temperature went from 0° to -37° C. These findings led Satterlund (1979) to suggest an equation for better prediction of incoming longwave with extremes in air temperature and humidity. Using the data sets of Aase and Idso (1978) and Stoll and Hardy (1955) he developed the following empirical equation

$$Rl{\downarrow} = (\sigma T^4)(1.08)[1-\exp(-e_o^{T/2016})] \qquad (6.11)$$

Satterlund compared results from equation (6.11), using the data sets of Aase and Idso (1978) and Stoll and Hardy (1955), to the results obtained from the algorithms supplied by Brutsaert (1975) and Idso and Jackson (1969). They found that equation (6.11) gave the best fit to the data.

Idso (1981) noted that several of the longwave equations (Brunt, Swinbank, Idso and Jackson, Brutsaert) did not compare well at all times, particularly when the air temperature fell below 273°K. He further noted that work on atmospheric water vapor dimers may explain why these particular longwave models do not compare well to measured values at all air temperatures. Therefore, Idso sought to provide a longwave model based upon existing knowledge of absorption/emission in the 8 to 14 μm waveband while incorporating the water dimer hypothesis. Actually, two equations emerged from his work

$$Rl\downarrow = (\sigma T^4)(0.179e_o^{1/7}\exp(350/T)) \qquad (6.12)$$

$$Rl\downarrow = (\sigma T^4)[0.70 + 5.95 \times 10^{-5}\ e_o\exp(1500/T)] \qquad (6.13)$$

Equations (6.4), (6.7), (6.8), (6.10), and (6.12) were evaluated by Hatfield et al. (1983). Data sets were obtained from several locations across the United States to provide a good range in temperature and humidity. Comparison of the data led Hatfield et al. (1983) to suggest that equations (6.4) and (6.7), with slightly different coefficients would provide estimates of incoming longwave within 5 percent of the measured value for most agricultural locations in the United States.

6.2 Materials and Methods

6.2.1 Instrumentation and Calibration

Outgoing longwave radiation was computed from the thermal data recorded by channel 8 of the MMR. Thermal calibration of the MMR was performed prior to and after data collection in 1987 at the U.S.D.A. Water Conservation Laboratory in Phoenix, Arizona. The procedure of Jackson et al. (1983a) was used.

Air temperature and vapor pressure data recorded by the Scheduler Plant Stress Monitor were used in calculating instantaneous values of the incoming longwave component. As this instrument was received from the factory just prior to the 1987 experimental period, no calibration of the various sensors were made. However, random checks, throughout the season, of the air temperature and humidity sensors were made against other sources and found to provide reasonable values.

Eppley pyrgeometers, which measure longwave radiation in the region 4.0 to 50.0 μm, were used to measure incoming longwave. These measurements provide a standard for comparison against the calculated (estimated) values of incoming longwave. Enz et al. (1975) noted that during clear days the dome of the pyrgeometers would absorb solar radiation and radiate longwave to the thermopile causing the pyrgeometer output to be too high. Albrecht et al. (1974) noted similar problems. Subsequently, Albrecht and Cox (1977) developed procedures for calibrating the pyrgeometer, thereby improving data quality. Their calibration equation was given as

$$\frac{E}{\eta} = L - \epsilon\sigma Ts^4 + k\sigma(Td^4 - Ts^4) \qquad (6.14)$$

where

E = sensor output
L = incident irradiance
σ = Stefan-Boltzmann constant
Ts = sink temperature
Td = dome temperature
ϵ = emissivity of the thermopile
η = instrument sensitivity
k = a constant

k is determined during the calibration, and η is supplied by the factory.

Attempts were made at calibrating the pyrgeometers using the procedures of Albrecht and Cox (1977). However, due to equipment and laboratory limitations the calculated values of k were found to be erroneous. Smith[1] suggested that for new pyrgeometers, such as ours, k should be very near to a value of 5. Therefore, the

---

[1]Smith, Eric. Department of Meteorology, Florida State University, Tallahassee, Florida, personal communication.

factory supplied value for η and a k of 5 were used in equation (3.15) to provide the measures of the incoming longwave.

6.2.2 Computational Method--Incoming Longwave

The equations of Brunt (1932), Brutsaert (1975), Idso and Jackson (1969), Swinbank (1963), Deacon (1970), Satterlund (1979), and two from Idso (1981) were used to compute estimates of incoming longwave radiation. Values of incoming longwave radiation estimated with the Swinbank (1963) and Deacon (1970) methods were reduced by 30 Wm^{-2} based upon the suggestion of Paltridge (1970). The results from the ten algorithms were compared to simultaneously measured values recorded by pyrgeometers, located nearby.

Air temperature and/or actual vapor pressure measurements are needed by the above equations. The Scheduler records air temperature and vapor pressure deficit (VPD). Vapor pressure deficit is the difference between saturation vapor pressure (e_s) and actual vapor pressure. If air temperature and VPD are known, then actual vapor pressure can be determined in the following way

$$e_o = (6.108)(10^{a/b}) - VPD \qquad (6.15)$$

where

e_o = actual vapor pressure [mb]
a = (7.5)(T)
b = 237.3 + T

and T is the air temperature in degrees C. The VPD as given by the Scheduler is in units of kiloPascals [kPa] and is converted into units of [mb] by multiplying by 10 before use in equation (6.15).

Equation (6.15) was used to estimate actual vapor pressure for the 1987 data set and for day numbers 180, 194, 195, and 224 of the 1988 data set. Due to equipment problems Scheduler data were not

114

available for days 145, 146, and 148 in 1988 so an alternate data
source was used. Dry (Td) and wet (Tw) bulb temperatures, at a
height of approximately two meters, were recorded by Portable
Automated Mesonet (PAM) stations located near the sites where data
were collected. These stations were managed by the National Center
for Atmospheric Research (NCAR), Boulder, Colorado. Data from the
PAMs were supplied upon request from NCAR. Wet and dry bulb
temperatures can be used to calculate estimates of e_0 from

$$e_0 = e_s - AP(Td-Tw) \tag{6.16}$$

where

$$e_s = 6.108(10^{a/b}) \tag{6.17}$$

$$A = 6.6*10^{-4}(1+1.15*10^{-3}*Tw) \tag{6.18}$$

"A" is in units of $°C^{-1}$ and "a" and "b" are defined in equation
(6.15). "P" is a pressure term, and for the Konza Prairie was set
equal to 966 [mb].

6.3   Results and Discussion

6.3.1   Outgoing Longwave Radiation

Typically, nadir derived thermal data are used to estimate
longwave radiation from the surface. Figure 6.1 is a plot of
emitted surface energy versus view zenith angle for two times of
day. In the morning there is little variation in emitted energy
with respect to the view zenith angle. However, in the mid-
afternoon there was a variation of approximately 30 Wm^{-2} relative
to the view angle used to sense the surface. The nadir temperature
was the highest for the mid-day plot, while the view angle of 50°
(looking towards the sun in its principal plane) was the lowest.
Because it is not known which angle best represents the surface
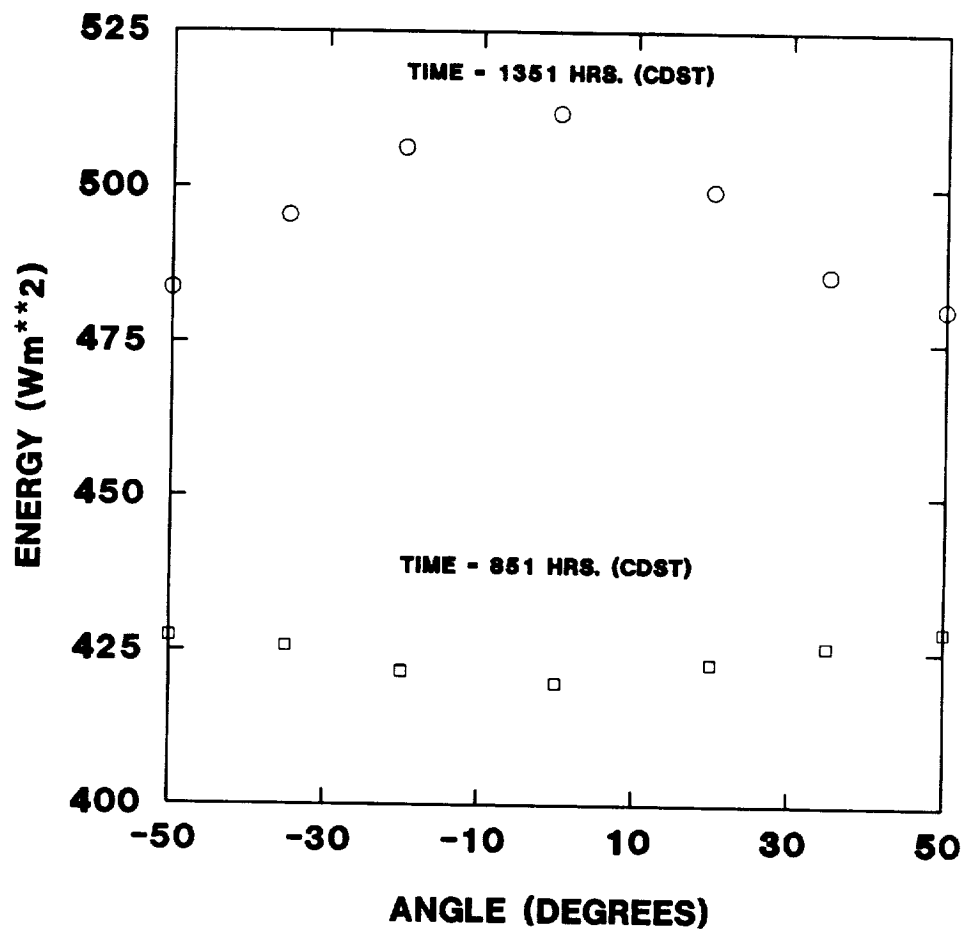
Figure 6.1 Energy emitted from a surface plotted against view zenith angle of the MMR at two times of day. Positive angles denote that the instrument was viewing towards the sun, negative angles denote viewing away from the sun.

emittance, nadir values of the MMR-derived radiant surface temperatures were converted into energy terms. During IFCs 3 and 4 the thermal channel did not function; therefore, no emitted longwave radiation was computed for days during those IFCs.

Independent measures of radiant surface temperature were made using infrared thermometers (i.e., an Everest infrared thermometer and the Scheduler). However, neither of these devices viewed the surface in a nadir position. The Scheduler was held approximately 1.5 meters above the surface at an angle of 20° from the horizontal. The Everest was mounted on a 2.5 meter pole with a view zenith angle of 30°. Because off-nadir radiant temperatures were found to differ from the nadir value, no attempt at computing the outgoing longwave from these instruments was made.

6.3.2 Incoming Longwave Radiation

6.3.2.2 1987 Data Set:

Due to equipment problems and data availability, only 12 days of pyrgeometer data were available for comparison. These 12 days furnish data taken at various times of day for dates between July 1 and August 20; thereby, providing a good test of the various algorithms. A total of 231 comparisons for each algorithm versus the pyrgeometer values were carried out. Relative errors for each of the 231 comparisons for each method were calculated and the results are listed in Table 6.1.

Table 6.1
Relative errors between estimated and measured incoming longwave radiation for 231 cases during the 1987 FIFE experimental period.

Method	Relative Error	Number of Cases	% of 231 Cases
Brunt	≤ 5%	190	82.3
	> 5% ≤ 10%	41	17.8
	> 10% ≤ 15%	0	0
	> 15% ≤ 20%	0	0
	> 20% ≤ 25%	0	0
	≥ 25%	0	0
Brutsaert	≤ 5%	11	4.8
	> 5% ≤ 10%	131	56.7
	> 10% ≤ 15%	86	37.2
	> 15% ≤ 20%	3	1.3
	> 20% ≤ 25%	0	0
	≥ 25%	0	0
Satterlund	≤ 5%	0	0
	> 5% ≤ 10%	56	24.1
	> 10% ≤ 15%	98	42.4
	> 15% ≤ 20%	35	15.2
	> 20% ≤ 25%	38	16.5
	≥ 25%	4	1.7
Idso-Jackson	≤ 5%	26	11.3
	> 5% ≤ 10%	72	31.2
	> 10% ≤ 15%	79	34.2
	> 15% ≤ 20%	30	13.0
	> 20% ≤ 25%	23	10.0
	≥ 25%	1	0.4
Idso 1	≤ 5%	30	13.0
	> 5% ≤ 10%	148	64.1
	> 10% ≤ 15%	53	22.9
	> 15% ≤ 20%	0	0
	> 20% ≤ 25%	0	0
	≥ 25%	0	0
Idso 2	≤ 5%	0	0
	> 5% ≤ 10%	22	9.5
	> 10% ≤ 15%	112	48.5
	> 15% ≤ 20%	96	41.6
	> 20% ≤ 25%	1	0.4
	≥ 25%	0	0
Swinbank	≤ 5%	43	18.6
	> 5% ≤ 10%	81	35.1
	> 10% ≤ 15%	63	27.3
	> 15% ≤ 20%	36	15.6
	> 20% ≤ 25%	8	3.5
	≥ 25%	0	0

Table 6.1
Continued

Method	Relative Error	Number of Cases	% of 231 Cases
Modified Swinbank[#]			
	≤ 5%	149	64.5
	> 5% ≤ 10%	75	32.5
	> 10% ≤ 15%	7	3.0
	> 15% ≤ 20%	0	0
	> 20% ≤ 25%	0	0
	≥ 25%	0	0
Deacon	≤ 5%	62	26.8
	> 5% ≤ 10%	85	38.5
	> 10% ≤ 15%	53	22.9
	> 15% ≤ 20%	30	13.0
	> 20% ≤ 25%	1	0.4
	≥ 25%	0	0
Modified Deacon[*]			
	≤ 5%	148	64.1
	> 5% ≤ 10%	79	34.2
	> 10% ≤ 15%	4	1.7
	> 15% ≤ 20%	0	0
	> 20% ≤ 25%	0	0
	≥ 25%	0	0

[#]Swinbank value minus 30 Wm^{-2}
[*]Deacon value minus 30 Wm^{-2}

Of the air temperature based models the modified Swinbank and modified Deacon methods yielded the most satisfactory results. Using the modified Swinbank method, 224 (97%) of the relative errors were less than or equal to 10 percent, and 149 (65%) of the cases were less than or equal to five percent. The modified Deacon method was slightly better with 227 (98%) of the cases having relative errors less than or equal to 10 percent, and 148 (64%) having less than or equal to five percent relative error. Of the algorithms that incorporate both actual vapor pressure and air temperature the Brunt equation performed the best, with 100% of the cases having relative errors less than or equal to ten percent.

Over 80% of the cases had relative errors less than or equal to five percent.

6.3.2.2 1988 Data Set:

Air temperature and vapor pressure data obtained using the Scheduler Plant Stress Monitor and the wet and dry bulb information from the PAMs provided 71 opportunities where the estimated incoming longwave radiation from the models could be compared to measured values. Relative errors for each of the 71 cases are listed in Table 6.2.

Table 6.2
Relative errors between estimated and measured incoming longwave radiation for 71 cases during the summer of 1988.

Method	Relative Error	Number of Cases	% of 71 Cases
Brunt	≤ 5%	37	52.1
	> 5% ≤ 10%	26	36.6
	> 10% ≤ 15%	8	11.3
	> 15% ≤ 20%	0	0
	> 20% ≤ 25%	0	0
	≥ 25%	0	0
Brutsaert	≤ 5%	4	5.6
	> 5% ≤ 10%	23	32.4
	> 10% ≤ 15%	27	38.0
	> 15% ≤ 20%	17	23.9
	> 20% ≤ 25%	0	0
	≥ 25%	0	0
Satterlund	≤ 5%	8	11.3
	> 5% ≤ 10%	35	49.3
	> 10% ≤ 15%	18	25.4
	> 15% ≤ 20%	10	14.1
	> 20% ≤ 25%	0	0
	≥ 25%	0	0
Idso-Jackson	≤ 5%	9	12.7
	> 5% ≤ 10%	22	31.0
	> 10% ≤ 15%	36	50.7
	> 15% ≤ 20%	4	5.6
	> 20% ≤ 25%	0	0
	≥ 25%	0	0

Table 6.2
Continued

Method	Relative Error	Number of Cases	% of 71 Cases
Idso 1	≤ 5%	12	16.9
	> 5% ≤ 10%	32	45.1
	> 10% ≤ 15%	19	26.8
	> 15% ≤ 20%	8	11.3
	> 20% ≤ 25%	0	0
	≥ 25%	0	0
Idso 2	≤ 5%	0	0
	> 5% ≤ 10%	4	5.6
	> 10% ≤ 15%	17	23.9
	> 15% ≤ 20%	22	31.0
	> 20% ≤ 25%	15	21.1
	≥ 25%	13	18.3
Swinbank	≤ 5%	11	15.5
	> 5% ≤ 10%	35	49.3
	> 10% ≤ 15%	25	35.2
	> 15% ≤ 20%	0	0
	> 20% ≤ 25%	0	0
	≥ 25%	0	0
Modified Swinbank[#]			
	≤ 5%	60	84.5
	> 5% ≤ 10%	11	15.5
	> 10% ≤ 15%	0	0
	> 15% ≤ 20%	0	0
	> 20% ≤ 25%	0	0
	≥ 25%	0	0
Deacon	≤ 5%	22	31.0
	> 5% ≤ 10%	40	56.3
	> 10% ≤ 15%	9	12.7
	> 15% ≤ 20%	0	0
	> 20% ≤ 25%	0	0
	≥ 25%	0	0
Modified Deacon[*]			
	≤ 5%	59	83.1
	> 5% ≤ 10%	12	16.9
	> 10% ≤ 15%	0	0
	> 15% ≤ 20%	0	0
	> 20% ≤ 25%	0	0
	≥ 25%	0	0

[#]Swinbank value $-30Wm^{-2}$
[*]Deacon value $-30Wm^{-2}$

As with the 1987 data set, both the modified Swinbank and modified Deacon methods yield the best results for models that use only air temperature as an input. The modified Swinbank method was only slightly better for this particular data set than the modified Deacon approach. Brunt's equation, again, provided the best results for those models that include both vapor pressure and air temperature.

6.4 Summary and Conclusions

Several incoming longwave models were evaluated for their ability to estimate incoming longwave radiation. Combining the results of the 1987 and 1988 data sets it is observed that, for air temperature based models, the modified Deacon equation works best overall; though only slightly better than the modified Swinbank method. The Deacon equation is simply the Swinbank method (equation 6.8) which has been adjusted for site elevation with the overall result being reduced by 30 Wm^{-2} according to a suggestion by Paltridge (1970). Of all models evaluated the Brunt equation performed best overall. For the purposes of this report the modified Deacon method and the Brunt method will be used to provide estimates of incoming longwave radiation. Both methods are used because they employ different meteorological inputs--Brunt's equation uses both actual vapor pressure and air temperature, and Deacon's uses only air temperature. If one only has access to air temperature data then the Deacon approach should be used, but if air temperature and vapor pressure are available the Brunt equation is better.

It has been noted in the literature that the various formulae available for computing incoming longwave perform well in some locations and not in others, and that they perform better for one part of the day than another. Although the incoming longwave radiations algorithms used in this research were not evaluated for seasonal or diurnal performance, it was observed that some did not work as well as others when compared to measured values. Due to the rather large data base acquired during FIFE, it is recommended that these data be used to further evaluate existing incoming longwave models or to create an alternative method for the computation of incoming longwave.

Outgoing longwave radiation was computed from nadir values of radiant temperatures obtained from the thermal channel of the MMR. Due to a problem with the thermal channel no temperature data were recorded during IFCs 3 and 4.

Off-nadir radiant temperatures differed from those obtained at nadir. As a thermal sensor is moved from a nadir position to a more oblique viewing angle, less soil and more canopy will be observed. Thus, the radiant temperature, as shown in Section 4 of this report, changes with viewing angle. Additionally, the effective canopy emissivity may change with viewing angle because i) the contribution from soil background changes, and ii) the proportion of sunlit and shaded canopy elements viewed by the sensor may change. There may also be effects produced by the sun itself. Palluconi et al. (1990) found that during nighttime the emissivity of prairie grasses was near unity and did not change with viewing angle. Appropriate procedures for estimating the outgoing longwave radiation stream from surface temperature

123

measurements made with thermal sensors still need further investigation.

7.0 ESTIMATION OF NET RADIATION

7.1 Introduction

Net radiation (R_n) is the balance of the shortwave and longwave radiation streams (equation 7.1).

$$R_n = Rsw\downarrow - Rsw\uparrow + Rlw\downarrow - Rlw\uparrow \qquad (7.1)$$

Rsw and Rlw are the shortwave and longwave components and the arrows denote the direction of the flux. It is the fundamental quantity of energy available at the earth's surface to drive the processes of photosynthesis (PS), heating of air (H) and soil (S), evaporation of water (LE), and miscellaneous processes (M) such as respiration (Rosenberg et al., 1983). Where there is adequate water, LE is generally the major consumer of energy. Energy is also consumed in PS, S, M, and H. Under conditions of sensible heat advection H becomes an energy supplier to the environment.

Variations in net radiation occur on a diurnal, seasonal, and spatial (horizontally and vertically) basis. Rosenberg et al. (1983) presented data on incoming solar radiation and net radiation for a cloudy and clear midsummer day over a soybean canopy (Fig. 7.1). During the day R_n is positive and reaches a maximum near solar noon. The cloudy sky case demonstrates the impact of incoming shortwave radiation on R_n. As the impinging solar beam is intercepted or attenuated by clouds, the surface receives less shortwave energy thereby reducing R_n. The diurnal course of R_n displayed in Fig. 7.1 is typical of a mid-latitude location in the Great Plains of the United States.

Blad and Baker (1971) presented results of a three year study in which R_n was measured over a sod surface at St. Paul, Minnesota. An example, from their work, of the seasonal course of R_n for a more northerly location is found in Figure 7.2 which represents the average monthly R_n for three years of data. The maximum R_n was reached during the middle part of the summer when the days are relatively long, while the lowest R_n was recorded during mid-winter when the days are relatively short. According to Blad and Baker (1971), the persistence of snow cover during the months of November-February was responsible for the duration of the negative R_n.

Implied in the discussion above is the notion of spatial variation. It should be obvious that the distribution and magnitude of R_n at the poles will be different than that observed at the equator. At the poles, the maximum R_n is reached during their respective summer months. However, at the equator the distribution of R_n is bimodal with the maxima occurring during the equinox months. Spatial variations of R_n also occur on smaller scales. Federer (1968) placed several net radiometers in a one hectare sized study site which had stands of hardwood, white pine, juniper, an open field, and a rock outcropping. He measured the albedo, surface temperature, and R_n and found them to be quite different for the various surfaces. Glover (1972) measured R_n over sugarcane and short lawn grass surfaces located fairly close to each other. When both were well watered there was little difference in R_n over the two sites. However, when the lawn grass experienced drought its albedo and radiative temperatures were affected and its R_n was lower than that of the sugarcane. Gay
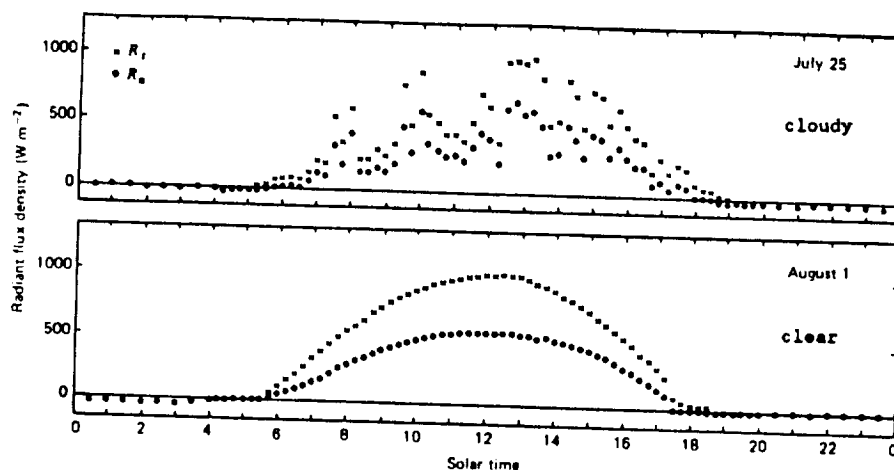
Figure 7.1 Solar (Rs) and net (Rn) radiation over soybeans at Mead, Nebraska, on cloudy and clear days in midsummer. (Adapted from Rosenberg et al., 1983.)
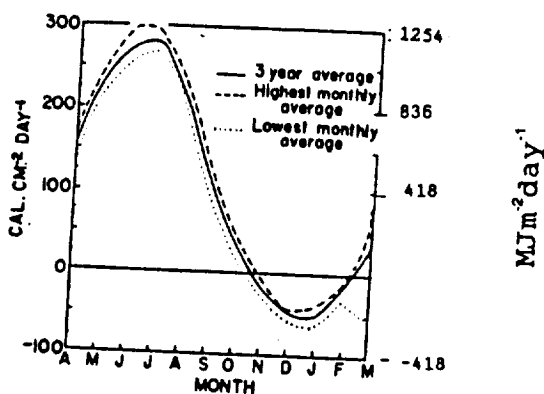
Figure 7.2 Average daily net radiation measured at St. Paul, Minnesota, showing the average, highest, and lowest values for each month, April 1964 - March 1967. (Adapted from Blad and Baker, 1971.)

(1979) measured the incoming, outgoing, and net shortwave, long-wave, and allwave radiation streams for desert, meadow, forest, and marsh in Oregon. The four cover types displayed different albedos, but because the various measurements were not made simultaneously over the sites the results were not strictly comparable. Nevertheless, Gay suggested that the surfaces partitioned the radiation streams differently thereby affecting the R_n.

Spatial variations of R_n may also occur over and within a homogeneous surface. Denmead et al. (1962) showed that 25 percent of the available R_n above a corn canopy reached ground level. Moreover, 73 percent of the available R_n was expended in the upper half of the canopy. Campbell et al. (1981) measured R_n above and within a corn canopy while inducing water stress upon certain plants. It was observed that the R_n received at ground level under the fully developed nonstressed plants was 32 percent of that above the canopy. For the stressed plants R_n received at the surface ranged from 46 percent to 51 percent in the later stages of drought.

Due to spatial variations in R_n, remotely sensed data have been evaluated for their capability in providing estimates of R_n at the spatial resolution of the sensor. Jackson et al. (1985) combined remotely sensed data with ground station meteorological data to estimate R_n. Reflected shortwave radiation was calculated from remotely sensed data acquired by a Barnes MMR using the method of Jackson (1984). Incoming solar radiation was measured with a pyranometer, the equation of Brutsaert (1975) was used to calculate incoming longwave radiation, and data from the thermal channel of the MMR were used to provide the emitted longwave radiation.

Results indicated that the combination of data types could be used to provide reasonable estimates of R_n. Vonder Haar and Suomi (1971), Raschke et al. (1973), Smith et al. (1977), and Jacobowitz et al. (1979) used data obtained from the polar orbiting TIROS, ESSA, and Nimbus satellites to estimate R_n. These particular satellites possess very coarse spatial resolution which limits their utility to large regions. The temporal resolution of 12 hours is also restrictive. Saunders and Hunt (1980) and Gube (1982) used the data from METEOSAT to estimate R_n. METEOSAT is a European geosynchronous orbiter that provides data for an earth disk every 30 minutes. Due to the geosynchronous orbit of METEOSAT only one part of the earth receives coverage, and the estimates of R_n are regional values.

Present satellite systems provide poor spatial and/or temporal resolution. As Sellers et al. (1988) stated, the results from FIFE thus far indicate a need for satellite systems that provide high-temporal resolution, a range of spatial resolutions, and pointable sensors.

7.2 Materials and Methods

7.2.1 Computational Methods

7.2.1.1 Estimated Component Technique:

Estimates of net radiation were calculated using estimated shortwave and longwave radiation values as inputs to equation (7.1). The Brunt method supplied the most accurate estimates of incoming longwave radiation and is used to calculate that component of R_n. Because actual vapor pressure measurements were sometimes lacking it was decided to use the modified Deacon values of

incoming longwave radiation as well. Thus, both the Brunt and modified Deacon values were incorporated into the estimates of R_n for comparison with measured values.

7.2.1.2 Measured Component Technique:

Measured components of the shortwave and longwave radiation streams were used to test the estimating algorithms in the previous chapters. These same data were used in equation (7.1) to compute an independent measure of R_n. R_n computed from equation (7.1) serves as a check, where possible, on the R_n values obtained from the net radiometers.

7.2.2 Instrumentation and Calibration

Single-dome net radiometers manufactured by Radiation Energy Balance Systems (REBS) were used in this study. The instruments were calibrated after the IFCs in 1987 using a shading technique described in Iqbal (1983). Values derived from the calibration procedure were used to convert the net radiometer voltages to energy units in $[Wm^{-2}]$. Calibration constants derived in 1987 for the net radiometers were used for the 1988 data set as well.

7.2.3 Experimental Procedure

During 1987 one net radiometer and one Eppley PSP were mounted onto a portable A-frame. In 1988 two net radiometers and two PSPs were used.

After the MMR recorded the bidirectional reflectance and surface temperature data of a given plot, the A-frame was placed over the MMR-viewed area and R_n and the shortwave radiation streams

were measured. The A-frame instrumentation recorded data as the MMR was moved from plot to plot. Generally, the A-frame measurements were acquired within five minutes following removal of the MMR from a given plot.

7.2.4 Measurement Error[1]

Every measurement is characterized by a numerical value, a dimension, and an error. Basically there are two types of error: i) determinate, which are of fixed magnitude and direction; and ii) indeterminate, which are variable and random. Indeterminate errors may result from random variations in the phenomenon being measured (sampling error) and/or the process of measurement (measurement error). Measurements that are combined to produce a calculated quantity give rise to propagated error.

Strictly speaking, true propagated error was not determined for R_n computed from the estimated components of the radiation streams. Measurement errors for the MMR and Scheduler Plant Stress Monitor were not given by the manufacturers. In spite of this, it is helpful to try assess the magnitude of error that may be associated with the R_n values calculated from the estimated components of the radiation streams. Therefore, an error of five percent was assigned to each of the estimated components of the radiation balance. An error of five percent appears to be reasonable in light of the statistical analysis performed above.

---

[1]Discussion on measurement error was taken from Soil Physics class notes by Professor Joe Skopp, Department of Agronomy, University of Nebraska-Lincoln.

131

Propagated error for R_n computed from the measured components is more readily determined. Components of the shortwave and longwave radiation streams were measured by Eppley PSPs, Eppley pyrgeometers, and the thermal channel of the Barnes MMR. A measurement error of two percent was assigned to the PSPs, five percent to the pyrgeometers, and five percent to the MMR thermal channel.

For a sum, such as that for the R_n calculated from the measured components, a value (A) and its propagated error (E) are determined by

$$A = a1 + a2 + a3 + \ldots \qquad (7.2)$$

$$E = [e1 + e2 + e3 + \ldots]^{1/2} \qquad (7.3)$$

where a1, a2, a3, etc. are the individual measures to be summed and e1, e2, e3, etc. are the respective measurement errors. When a product is involved A and E are found in the following way:

$$A = a1 * a2 * a3 * \ldots \qquad (7.4)$$

$$E^2/A^2 = e1^2/a1^2 + e2^2/a2^2 + \ldots \qquad (7.5)$$

Field[2] reported on intercomparison of net radiometers used during the 1987 portion of FIFE. He observed that REBS double-dome net radiometers behaved differently than single-dome types constructed by other manufacturers. Since the report of Field, much investigation into the performance of net radiometers has ensued, resulting in design and calibration modification. Most of the problems appear to be associated with the double-dome type net radiometers, but investigation is on-going and no definite conclusions have yet been published. Our net radiometers are of

---

[2]Field, Richard. University of Delaware, Newark, Delaware. Personal Communication.

the single-dome construct and a measurement error of ten percent was assumed.

7.3 Results and Discussion

7.3.1 1987 Data Set

The measured components of the shortwave and longwave radiation streams are used in equation (7.1) to produce values of R_n. Estimated albedo from equation (5.22), estimated incoming shortwave radiation from equation (5.19), incoming longwave radiation calculated from the modified Deacon and Brunt methods, and emitted longwave radiation derived from the thermal channel of the MMR are used in equation (7.1) to compute estimated R_n. These two calculation techniques have in common the same input values of emitted longwave radiation. Rather than refer to the two procedures as the measured component and estimated component techniques, they will be referred to as "method MC" and "method EC", where MC refers to the measured component method and EC refers to the estimated component method.

Due to a non-functioning thermal channel in the MMR no measure of emitted longwave radiation was available for the last two IFCs of 1987. Therefore, R_n could not be computed for either method. Intermittent equipment malfunction on the A-frame during the first two IFCs restricted calculation of R_n using method MC, to 67 cases where measured R_n could be compared to results from methods MC and EC. Comparisons of measured R_n with results from method EC were limited to 187 cases.

Values of R_n from the net radiometer are plotted against those computed from method MC (Fig. 7.3) for the 67 cases. It is
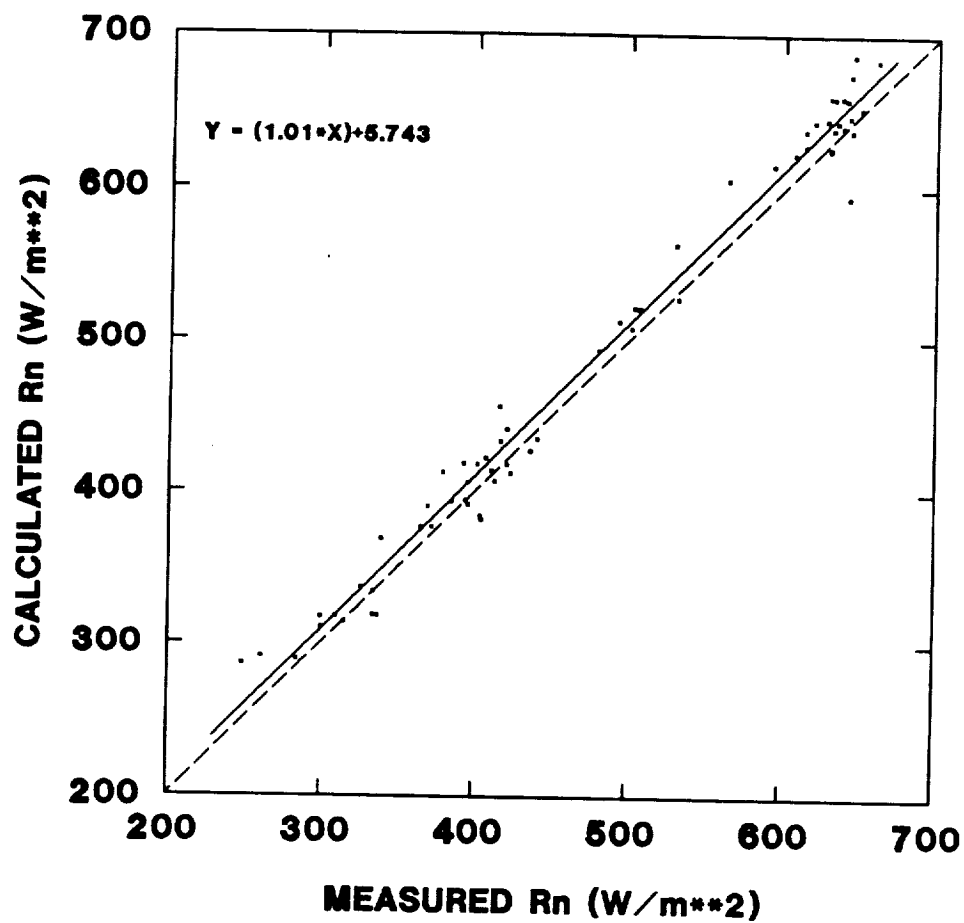
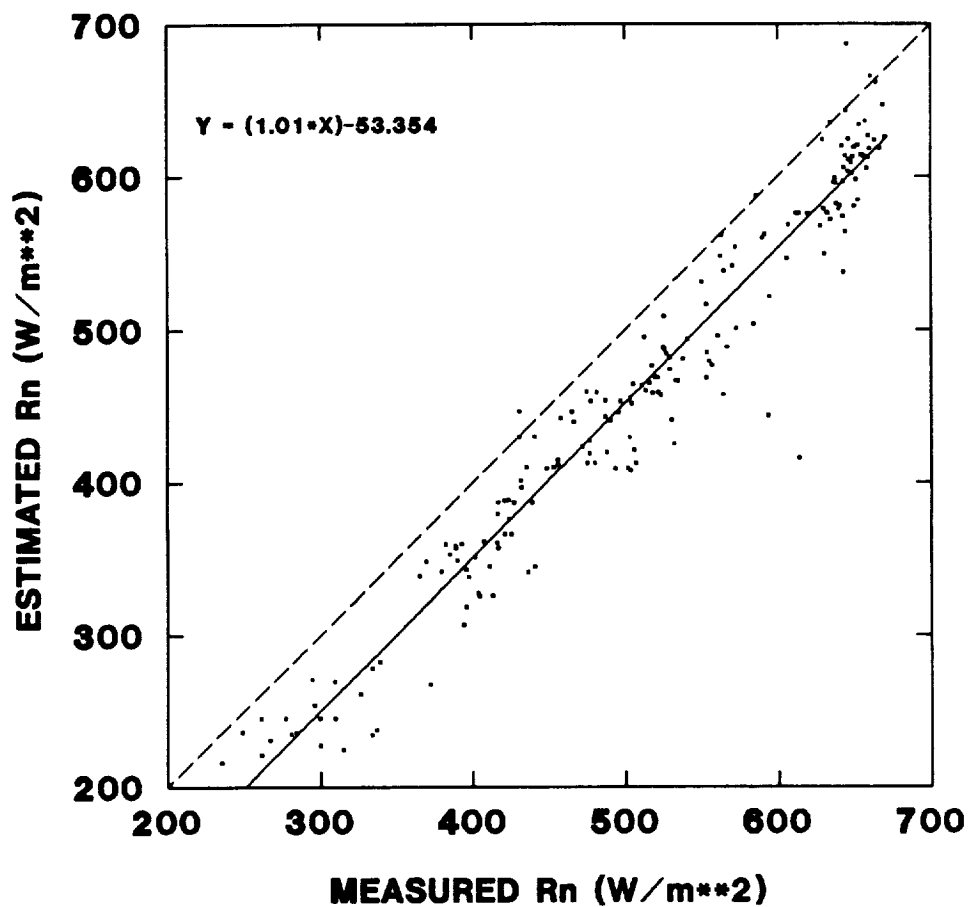**Figure 7.3** Comparison of measured net radiation to that calculated from measured components of the incoming and outgoing radiation streams. N = 67.

observed that the values from method MC are fairly close to those recorded by the net radiometer. The regression equation has a slope close to one and the y-intercept is approximately 6 Wm^{-2}. Values of r, r^2, and d are all high (Table 7.1) suggesting that R_n computed from method MC is very close to that of the net radiometer. Average total error in method MC is approximately 20 Wm^{-2}, and a large portion of this is random error. Thus, there is good agreement between net radiation measured by the net radiometers and the independent values of R_n calculated from the measured components of the incoming and outgoing radiation streams. The implication of this is that if R_n values calculated from method EC do not agree well with the net radiometer values then there is a problem with the estimating procedure (i.e., one or more of the estimated components) and not the net radiometers.

Table 7.1
Results of the statistical analysis
for method MC (67 cases)—
1987 data set.

Method	d	r	r^2	MBE	MRE	Q	s	cv	RMSE	Eu	Es
MC	.994	.992	.984	10.5	2.3	493.1	130.3	0.26	19.6	16.5	10.6
Meas.						482.6	128.0	0.27			

Graphical comparison of the values of Rn from method EC and the net radiometer for the 187 cases is found in Figure 7.4. Method EC here incorporates the estimate of incoming longwave radiation as provided by the modified Deacon equation. As with the comparison above, method EC underestimates the value of the net radiometer. It is noted that the average underestimation is 50 Wm^{-2} and the MRE is approximately 10 percent, which is the assumed

Figure 7.4 Comparison of measured net radiation to that calculated from estimated components of the incoming and outgoing radiation streams. Estimates of incoming longwave radiation used in the calculation from the modified Deacon equation.

measurement error of the net radiometer (Table 7.2). Values of r, r^2, and d are all high which implies that the method provides good estimates of R_n. The average total error in method EC for the 187 cases is about 56 Wm^{-2}, the systematic error is 48 Wm^{-2}, and the unsystematic error is approximately 28 Wm^{-2}. The large systematic error implies a modeling problem.

Table 7.2
Results of the statistical analysis
for method EC (187 cases)—
(Modified Deacon incoming longwave radiation as input)

Method	d	r	r^2	MBE	MRE	Q	s	cv	RMSE	Eu	Es
EC	.945	.971	.944	−50.3	−10.1	459.2	114.4	0.25	55.9	28.3	48.3
Meas.						509.5	115.3	0.23			

Net radiometers used in this study were assumed to have a measurement error of ± ten percent. Thus, if the measured net radiation is 350 Wm^{-2} the true value is somewhere between 315 Wm^{-2} and 385 Wm^{-2}. Of the 187 cases of estimated R_n 100 (53.5%) of the values fall within ± ten percent of the corresponding measurement. That is, over one-half of the estimates of R_n are within the measurement error of the net radiometer. When the estimated values of R_n, plus and minus their measurement error, were compared to measured R_n, plus and minus measurement error, an additional 73 cases of estimated R_n were found to be within the measurement error of the net radiometer. Hence, when propagated error for method EC is considered 173 (92.5%) cases of estimated R_n are found to be within the range of measurement error of the net radiometer.

Estimates of R_n were also computed using the Brunt values of incoming longwave radiation as inputs to method EC. Graphical

comparison of measured R_n with that estimated from method EC is found in Figure 7.5, and the results of the statistical analysis are found in Table 7.3. Comparison of the contents of Table 7.3 with those from Table 7.2 indicates that there is little difference between using the Brunt and modified Deacon values of incoming longwave radiation when estimating R_n from method EC. The d statistic, r, and r^2 indicate that method EC performs a little better when the modified Deacon values are used. Consideration of measurement and propagated error reveals that 97.3% of the estimates of R_n are within the measurement error of the net radiometer.

Table 7.3
Results of the statistical analysis
for method EC (187 cases)—
(Brunt incoming longwave radiation as input)

Method	d	r	r^2	MBE	MRE	Q	s	cv	RMSE	Eu	Es
EC	.940	.969	.940	−50.3	−10.1	459.2	114.4	0.25	57.7	28.1	50.4
Meas.						509.5	115.3	0.23			

7.3.2 **1988 Data Set**

No readings of emitted longwave radiation from the surface were available on two of the seven days of measurement in 1988 due to equipment malfunction. Comparisons of estimated (method EC) and calculated (method MC) R_n to measured values were, therefore, limited to 56 cases.

As in 1987, values of R_n computed using the measured components of the radiation streams are fairly close to those recorded by the net radiometers (Figure 7.6). Statistical analyses (Table 7.4) reveal that method MC underestimates by approximately
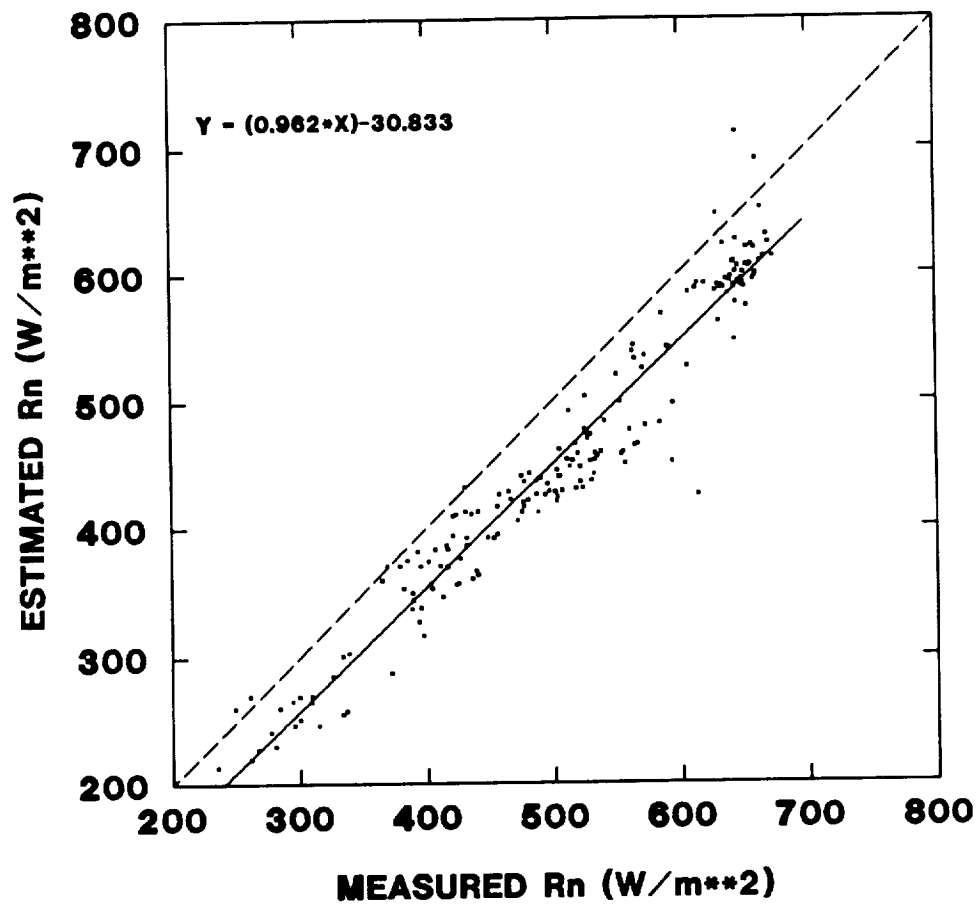
Figure 7.5 Comparison of measured net radiation to that calculated from estimated components of the incoming and outgoing radiation streams. Estimates of incoming longwave radiation used in the calculation from the Brunt equation.
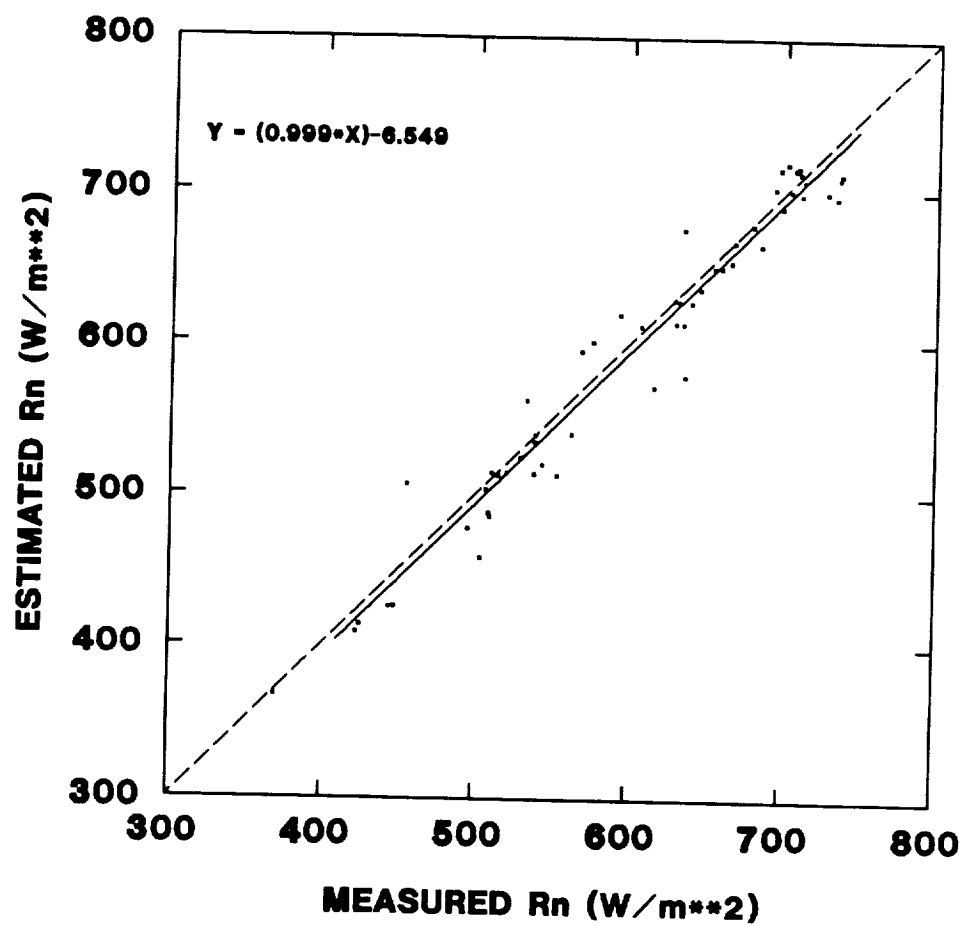
Figure 7.6 Comparison of measured net radiation to that calculated from measured components of the incoming and outgoing radiation streams.

7 Wm^{-2} and that the mean relative error is about 1%. The r and r^2 values indicate that there is a strong positive relationship between measured R_n and that approximately 96% of the variation in measured R_n is explained by method MC. A large d value (0.987) indicates good agreement with the measured values. Average total error in method MC is 22 Wm^{-2} with a large portion of this being an unsystematic error (21 Wm^{-2}).

Table 7.4
Results of the statistical analysis
for method MC (56 cases)—
1988 data set

Method	d	r	r^2	MBE	MRE	Q	s	cv	RMSE	Eu	Es
MC	.987	.977	.955	−7.1	−1.2	594.8	98.6	0.17	21.9	20.7	7.2
Meas.						601.9	96.5	0.16			

Net radiation was also estimated with method EC. Incoming longwave radiation values were supplied by the modified Deacon procedure. Comparison of estimated R_n and measured values is graphically depicted in Figure 7.7. It is observed that method EC underestimates the measured value and that this underestimation is, on average, approximately 40 Wm^{-2} (Table 7.5). The mean relative error indicates that method EC underestimates the measured value by approximately 6%. Values of d, r, and r^2 all suggest that method EC performs well. Forty nine (87.5%) of the estimates fell within the measurement error of the net radiometers. When propagated error of estimated R_n is considered an additional seven (12.5%) cases are found to be within the measurement error of the net radiometers.

Figure 7.7 Comparison of measured net radiation to that calculated from the estimated components of the incoming and outgoing radiation streams. Estimates of incoming longwave radiation used in the calculation from the modified Deacon equation.
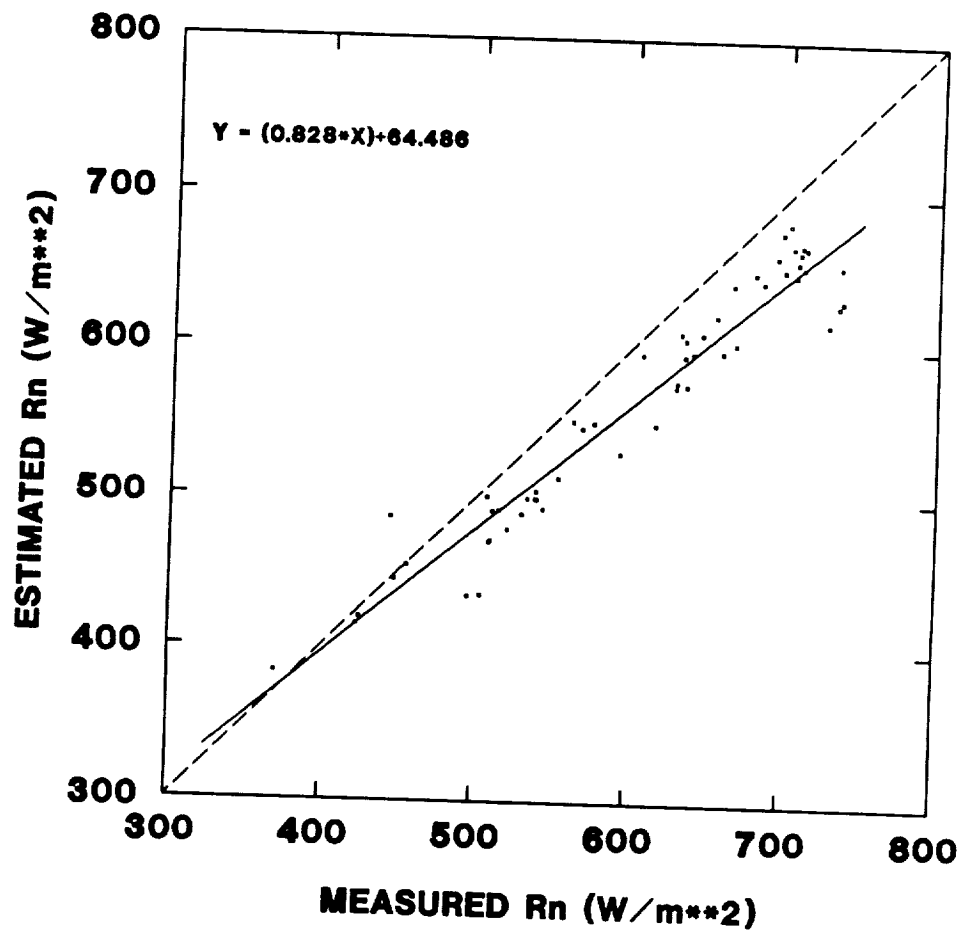
142

Table 7.5
Results of the statistical analysis
for method EC (56 cases)—
(Modified Deacon incoming longwave radiation as input)

Method	d	r	r^2	MBE	MRE	Q	s	cv	RMSE	Eu	Es
EC	.931	.965	.931	-39.1	-6.2	562.8	82.8	0.15	47.5	21.6	42.4
Meas.						601.9	96.5	0.16			

Values of incoming longwave radiation calculated from Brunt's equation were also utilized in method EC. In general, this method tends to underestimate measured values (Figure 7.8). The statistical analysis (Table 7.6) reveals that by using the Brunt values of incoming longwave radiation method EC produces a better estimate of R_n than if the modified Deacon values are used. Fifty one (91.1%) of the 56 estimates of net radiation are within measurement error of the net radiometers. Consideration of the propagated error places the remaining five cases within the measurement error as well.

Table 7.6
Results of the statistical analysis
for method EC (56 cases)—
(Brunt incoming longwave radiation as input)

Method	d	r	r^2	MBE	MRE	Q	s	cv	RMSE	Eu	Es
EC	.977	.971	.942	-15.2	-2.3	586.8	88.5	0.15	28.1	21.1	18.6
Meas.						601.9	96.5	0.16			

7.4 Summary and Conclusions

The 1988 estimates of R_n were marginally better than those in 1987 when the modified Deacon values of incoming longwave radiation were used. Large systematic errors were encountered in both 1987 and 1988 when the modified Deacon incoming longwave radiation values were used. Brunt longwave radiation values produced much
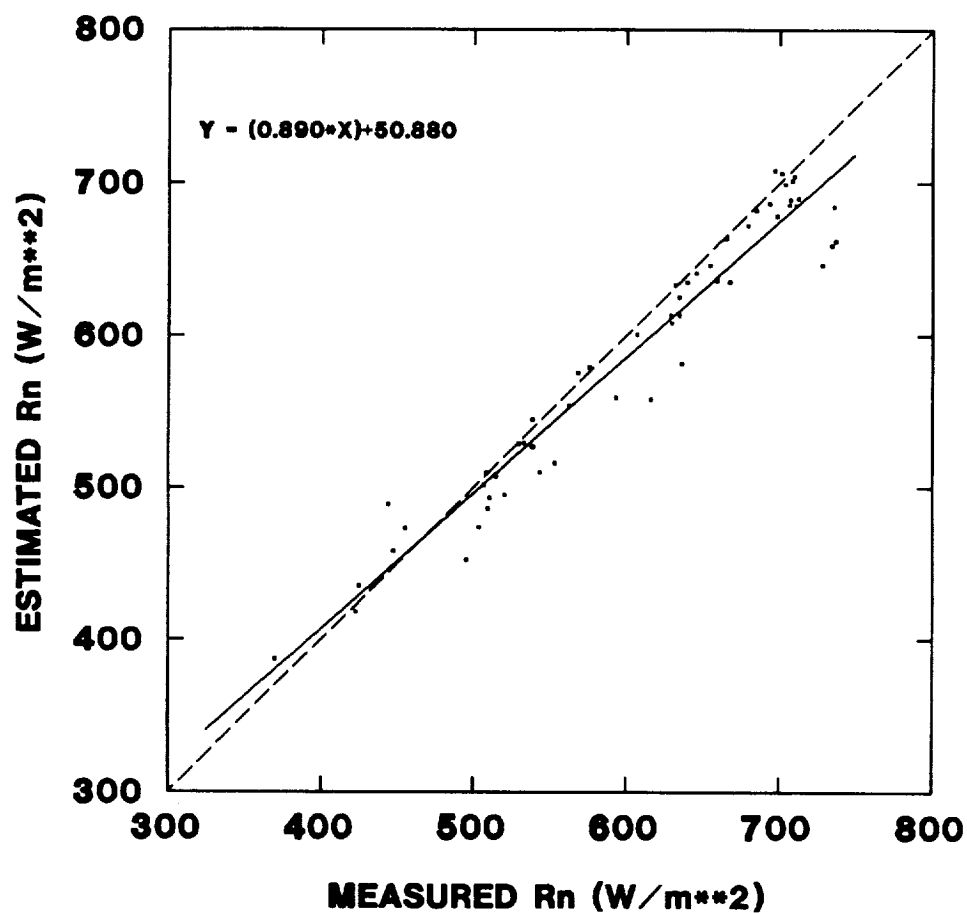
Figure 7.8 Comparison of measured net radiation to that calculated from estimated components of the incoming and outgoing radiation streams. Incoming longwave radiation values from the Brunt equation.

better estimates of R_n in 1988 than in 1987. This may be due to compensating errors in the estimates of the incoming and outgoing radiation streams. A large systematic error was observed in 1987 when the Brunt values were used. However, in 1988 the systematic error was smaller than that noted in 1987, and only slightly smaller than the unsystematic error.

Statistical results reveal that estimates of R_n are fairly accurate. Values of r, r^2, and d are all greater than 0.9 for both the 1987 and 1988 data sets. Perhaps the most important statistic to this discussion is the MRE. The largest MRE encountered was - 10% which means that, on average, estimates of R_n were within 10% of the measured value. It is also interesting to note that the value of 10% is the measurement error ascribed to the net radiometers used in this study.

Consideration of measurement and propagated error also reveals that estimates of R_n are very accurate. One hundred percent of the estimates of R_n were found to be within the measurement error of the net radiometers which were used in this study as the basis of comparison. Thus, it is concluded that net radiation can be accurately estimated using the model developed herein.

Net radiation was estimated using remotely sensed inputs of the type presently recorded by some satellite systems. Incoming longwave radiation was the only input parameter that was not determined by remote sensing means. Two meteorologically based algorithms (Brunt's equation and the modified Deacon method) were used to provide this input. These two algorithms represent two ways of obtaining reasonable estimates of incoming longwave radiation using air temperature and/or vapor pressure of the

atmosphere. Analysis of the 1987 results indicate that it makes little difference in R_n estimation if one chooses the Brunt longwave radiation value over that provided by the modified Deacon approach. For both methods of estimating R_n, measured R_n was underestimated by approximately 50 Wm^{-2}. The 1988 results showed that the estimates of R_n obtained when using the Deacon longwave radiation values underestimated measured values of R_n by about 42 Wm^{-2}. However, when using the Brunt values the underestimation of R_n was only 19 Wm^{-2}. Even though there is some discrepancy between the 1987 and 1988 results it appears that net radiation can be estimated within 50 Wm^{-2} of the actual value. Statistical analysis reveals that in most cases there is a large systematic error component. Therefore, by making the appropriate changes in the models that provide the estimates of the incoming and outgoing radiation streams, or in the experimental procedures, it should be possible to produce estimates of R_n that are in excellent agreement with measured results.

It is recommended that a closer look be taken at the models used for estimating the various components in the radiation balance which were discussed in the previous sections. Where possible these models should be refined to produce better estimates of R_n.

LITERATURE CITED

Aase, J.K. and Idso, S.B. (1978). A comparison of two formula types for calculating long-wave radiation from the atmosphere. Water Resources Research 14:623-625.

Albrecht, B., Poellet, M., and Cox, S.K. (1974). Pyrgeometer measurements from aircraft. Review of Scientific Instrumentation 45:33-38.

Albrecht, B. and Cox, S.K. (1977). Procedures for improving pyrgeometer performance. Journal of Applied Meteorology 16:188-197.

Barry, R.G. and Chambers, R.E. (1966). A preliminary map of summer albedo over England and Wales. Quarterly Journal of the Royal Meteorological Society 92:543-548.

Bartlett, D.S., Johnson, R.W., Hardisky, M.A., and Klemas, V. (1986). Assessing impacts of off-nadir observation on remote sensing of vegetation: use of the Suits model. International Journal of Remote Sensing 7:247-264.

Bauer, K.G. and Dutton, J.A. (1962). Albedo variations measured from an airplane over several types of surface. Journal of Geophysical Research 67:2367-2376.

Bird, R. and Riordan, C. (1984). Simple solar spectral model for direct and diffuse irradiance on horizontal and tilted planes at the earth's surface for cloudless atmospheres. Solar Energy Research TR-215-2436, Golden, CO., 29pp.

Bird, R. and Riordan, C. (1986). Simple solar spectral model or direct and diffuse irradiance on horizontal and tilted planes at the earth's surface for cloudless atmospheres. Journal of Climate and Applied Meteorology 25:87-97.

Blad, B. and Baker, D. (1971). A three-year study of net radiation at St. Paul, Minnesota. Journal of Applied Meteorology 10:820-824.

Blad, B.L., and Rosenberg, N.J. (1976). Measurements of crop temperature by leaf thermocouple, infrared thermometry and remotely sensed thermal imagery. Agronomy Journal 68:635-641.

Brest, C. (1987). Seasonal albedo of an urban/rural landscape from satellite observations. Journal of Climate and Applied Meteorology 26:1169-1187.

Brest, C. and Goward, S. (1987). Deriving surface albedo measurements from narrow band satellite data. International Journal of Remote Sensing 8:351-367.

147

Brunt, D. (1932). Notes on radiation in the atmosphere 1. *Quarterly Journal of the Royal Meteorological Society* 58:389-418.

Brutsaert, W. (1975). On a derivable formula for long-wave radiation from clear skies. *Water Resources Research* 11:742-744.

Campbell, R.B., Reicosky, D.C., and Doty, C.W. (1981). Net radiation within a canopy of sweet corn during drought. *Agricultural Meteorology* 23:143-150.

Carlson, T.N., Dodd, J.K., Benjamin, S.G., and Cooper, J.N. (1981). Satellite estimation of the surface energy balance, moisture availability and thermal inertia. *Journal of Applied Meteorology* 20:67-87.

Charney, J., Quirk, W.J., Chow, S., and Kornfield, J. (1977). A comparative study of the effects of albedo change on drought in semi-arid regions. *Journal of the Atmospheric Sciences* 34:1366-1385.

Choudhury, B.J., Reginato, R.J., and Idso, S.B. (1986). An analysis of infrared temperature observations over wheat and calculation of latent heat flux. *Agric. For. Meteorol.* 37:75-88.

Cogan, J.L. and Willand, J.H. (1976). Measurement of sea surface temperature by the NOAA 2 satellite. *Journal of Applied Meteorology* 15:173-180.

Colwell, J.E. (1974). Vegetation canopy reflectance. *Remote Sensing of Environment* 3:175-183.

Conaway, J. and van Bavel, C.H.M. (1967). Evaporation from a wet soil surface calculated from radiometrically determined surface temperatures. *Journal of Applied Meteorology* 6:650-655.

Coulson, K.L. (1975). *Solar and Terrestrial Radiation*, Academic Press: New York, New York, 322 pp.

Dave, J., Halpern, P., and Braslau, N. (1975). Spectral distribution of the direct and diffuse solar energy received at sea-level of a model atmosphere. *Report G320-3332*, IBM Palo Alto Scientific Center.

Deacon, E.L. (1970). The derivation of Swinbank's long-wave radiation formula. *Quarterly Journal of the Royal Meteorological Society* 96:313-319.

Deering, D.W. (1989). Field measurements of bidirectional reflectance. In: *Theory and Applications of Optical Remote Sensing*, G. Asrar (ed.). John Wiley and Sons, NY. pp. 14-65.

Deering, D.W. and Middleton, E.M. (1990). Spectral bidirectional reflectance and effects on vegetation indices for a prairie grassland. _Proceedings of Symposium on FIFE_. American Meteorological Society, Anaheim, CA. pp. 71-76.

Denmead, O., Fritschen, L., and Shaw, R. (1962). Spatial distribution of net radiation in a corn field. _Agronomy Journal_ 54:505-510.

Diak, G. and Gautier, C. (1983). Improvements to a simple physical model to estimate incident solar radiation at the surface from GOES satellite data. _Journal of Applied Meteorology_ 22:505-508.

Diner, D.J., Bruegge, C.J., Martonchik, J.V., Ackerman, T.P., Davies, R., Gerstl, S.A.W., Gordon, H.R., Sellers, P.J., Clark, J., Daniels, J.A., Danielson, E.D., Duval, V.G., Klaasen, K.P., Lilienthal, G.W., Nakamoto, D.I., Pagano, R.J., and Reilly, T.H. (1989). MISR: A multiangle imaging spectro-radiometer for geophysical and climatological research from EOS. _IEEE Trans. Geosci. Remote Sens._ 27(2):200-211.

Discussion. (1964). Discussion: Long-wave radiation from clear skies by W.C. Swinbank, _Quarterly Journal of the Royal Meteorological Society_ 90:488-493.

Duggin, M.J. (1977). Likely effects of solar elevation on the quantification of changes in vegetation with maturity using sequential Landsat imagery. _Applied Optics_ 16:521-523.

Eaton, F.D. and Dirmhirn, I. (1979). Reflected irradiance indicatrices of natural surfaces and their effect on albedo. _Appl. Optics_ 18:994-1008.

Egbert, D.D. and Ulaby, F.T. (1972). Effects of angles on reflectivity. _Photogrammetric Engineering_ 556-564.

El-Adawi, M., El-Niklawi, M., Kutub, A., and Al-Barakati, G. (1986). Estimation of the hourly solar irradiance on a horizontal surface. _Solar Energy_ 19:179-184.

Elachi, C. (1987). _Introduction to the Physics and Techniques of Remote Sensing_, John Wiley and Sons: New York, New York, 413 pp.

Elsasser, W.M. (1942). _Heat Transfer by Infrared Radiation in the Atmosphere_, Harvard Meteorological Studies No. 6, Harvard University.

Enz, J.W., Klink, J.C., and Baker, D.G. (1975). Solar radiation effects on pyrgeometer performance. _Journal of Applied Meteorology_ 14:1297-1302.

Federer, C. (1968). Spatial variation of net radiation, albedo, and surface temperature of forests. _Journal of Applied Meteorology_ 7:789-795.

Fuchs, M. and Tanner, C.B. (1966). Infrared thermometry of vegetation. _Agronomy Journal_ 58:597-601.

Fuchs, M., Kanemasu, E.T., Kerr, J.P., and Tanner, C.B. (1967). Effect of viewing angle on canopy temperature measurements with infrared thermometers. _Agron. J._ 59:494-496.

Gates, D.M., Keegan, H.J., Schleter, J.C., and Weidner, V.R. (1965). Spectral properties of plants. _Appl. Optics_ 4:11-20.

Gausman, H.W., Allen, W.A., Cardenas, R., and Richardson, A.J. (1970). Relation of light reflectance to histological and physical evaluations of cotton leaf maturity. _Appl. Optics_ 9:545-552.

Gausman, H.W., Allen, W.A., Cardenas, R., and Richardson, A.J. (1971a). Effects of leaf nodal position on absorption and scattering coefficients and infinite reflectance of cotton leaves, _Gossypium hirsutum_ L. _Agron. J._ 63:87-91.

Gausman, H.W., Allen, W.A., Escobar, D.E., Rodiguez, R.R., and Cardenas, R. (1971b). Age effects of cotton leaves on light reflectance, transmittance, and absorptance and on water content and thickness. _Agron. J._ 63:465-469.

Gausman, H.W. and Allen, W.A. (1973). Optical parameters of leaves of 30 plant species. _Plant Physiol._ 52:57-62.

Gausman, H.W. (1977). Reflectance of leaf components. _Remote Sens. Environ._ 6:1-9.

Gausman, H.W. (1982). Visible light reflectance, transmittance, and absorptance of differently pigmented cotton leaves. _Remote Sens. Environ._ 13:233-238.

Gautier, G., Diak, G., and Masse, S. (1980). A simple physical model to estimate incident solar radiation at the surface from GOES satellite data. _Journal of Applied Meteorology_ 19:1005-1012.

Gay, L. (1979). Radiation budgets of desert, meadow, forest, and marsh sites. _Archiv Fur Meteorologie Geophysik und Biolklimatologie_ Ser. B 27:349-359.

Gillespie, A.R. and Kahle, A.B. (1977). Construction and interpretation of a digital thermal inertia image. _Photogrammetric Engineering and Remote Sensing_ 43:983-1000.

Glover, J. (1972). Net radiation over tall and short grasses. _Agricultural Meteorology_ 10:455-459.

Goody, R.M. (1964). Atmospheric Radiation I: Theoretical Basis, Oxford University Press: London, 436 pp.

Grant, L., Daughtry, C.S.T., and Vanderbilt, V.C. (1987). Polarized and nonpolarized leaf reflectances of Coleus blumei. Environ. and Exper. 27:139-145.

Gube, M. (1982). Radiation budget parameters at the top of earth's atmosphere derived from METEOSAT data. Journal of Applied Meteorology 21:1907-1921.

Hall, F.G., Sellers, P.J., McPherson, I., Kelly, R.D., Verma, S.B., Markham, B., Blad, B., Wang, J., and Strebel, D.E. (1989). FIFE: Analysis and results - a review. Advances in Space Research 9:275-293.

Haltiner, G.J. and Martin, F.L. (1957). Dynamical and Physical Meteorology, McGraw-Hill Book Company: New York, New York, 470 pp.

Hanson, K. (1971). Studies of cloud and satellite parametrization of solar irradiation at the earth's surface. Proceedings of the Miami Workshop on Remote Sensing, U.S. Department of Commerce, 133-148.

Hatfield, J.L., Reginato, R.J. and Idso, S.B. (1983). Comparison of long-wave radiation calculation methods over the United States. Water Resources Research 19:285-288.

Hatfield, J.L., Reginato, R.J. and Idso, S.B. (1984). Evaluation of canopy temperature-evapotranspiration models over various crops. Agricultural and Forest Meteorology, 32:41-53.

Heilman, J.L., Kanemasu, E.T., Rosenberg, N.J. and Blad, B.L. (1976). Thermal scanner measurement of canopy temperatures to estimate evapotranspiration. Remote Sensing of Environment, 5:137-145.

Holben, B. and Fraser, R.S. (1984). Red and near-infrared sensor response to off-nadir viewing. International Journal of Remote Sensing 5:145-160.

Holm, R.G., Jackson, R.D., Yuan, B., Moran, M.S., Slater, P.N., and Biggar, S.F. (1989). Surface reflectance factor retrieval from Thematic Mapper Data. Remote Sensing of Environment 27:47-57.

Huband, N.D.S. and Monteith, J.L. (1986). Radiative surface temperature and energy balance of a wheat canopy. Boundary-Layer Meteorology 36:1-17.

Huschke, R.E. (ed.), (1959). Glossary of Meteorology. American Meteorological Society: Boston, Mass., 638 pp.

Idso, S.B. and Jackson, R.D. (1969). Thermal radiation from the atmosphere. _Journal of Geophysical Research_, 74:5397-5403.

Idso, S.B., Jackson, R.D., and Reginato, R.J. (1976). Determining emittances for use in infrared thermometry: a simple technique for expanding the utility of exisiting methods. _Journal of Applied Meteorology_, __:16-20.

Idso, S.B. (1981). A set of equations for full spectrum and 8- to 14-μm and 10.5- to 12.5 μm thermal radiation from cloudless skies. _Water Resources Research_, 17:295-304.

Iqbal, M. (1983). _An Introduction to Solar Radiation_. Academic Press: Toronto, Canada, 390pp.

Irons, J., Ranson, K., and Daughtry, C. (1988). Estimating Big Bluestem albedo from directional reflectance measurements. _Remote Sensing of Environment_ 25:185-199.

Isard, S. (1986). Evaluation of models for predicting insolation on slopes within the Colorado alpine tundra. _Solar Energy_ 36:333-344.

Jackson, R.D., Pinter, P.J., Idso, S.B., and Reginato, R.J. (1979). Wheat spectral reflectance: interactions between crop configuration, sun elevation, and azimuth angle. _Applied Optics_ 18:3730-3732.

Jackson, R.D. (1983). Assessing moisture stress in wheat with hand-held radiometers. _SPIE_, 356:138-142.

Jackson, R.D., Dusek, D.A. and Ezra, C.E. (1983a). Calibration of the thermal channel on four Barnes Model 12-1000 multi-band radiometers. _United States Water Conservation Laboratory Report 12_, Phoenix, Arizona.

Jackson, R.D., Hatfield, J.L., Reginato, R.J., Idso, S.B., and Pinter, P.J. (1983b). Estimation of daily evapotranspiration from one time-of-day measurements. _Agricultural Water Management_ 7:351-362.

Jackson, R.D. (1984). Total reflected solar radiation calculated from multi-band sensor data. _Agricultural and Forest Meteorology_ 33:163-175.

Jackson, R.D., Pinter, P.J., and Reginato, R.J. (1985). Net radiation calculated from remote multispectral and ground station meteorological data. _Agricultural and Forest Meteorology_ 35:153-164.

Jackson, R.D. and Robinson, B.F. (1985). Field evaluation of the temperature stability of a multispectral radiometer. _Remote Sensing of Environment_ 17:103-108.

Jackson, R.D., Moran, S.M., Slater, P.N., and Biggar, S.F. (1987). Field calibration of reference reflectance panels. <u>Remote Sensing of Environment</u> 22:145-158.

Jacobowitz, H., Smith, W., Howell, H., Nagle, F., and Hickory, J. (1979). The first 18 months of planetary radiation budget measurements from the Nimbus 6 ERB experiment. <u>Journal of the Atmospheric Sciences</u> 36:501-507.

Kamada, R. and Flocchini, R. (1986). Gaussian solar flux model. <u>Solar Energy</u> 36:73-87.

Kimes, D.S., Smith, J.A., and Ranson, K.J. (1980). Vegetation reflectance measurements as a function of solar zenith angle. <u>Photogrammetric Engineering and Remote Sensing</u> 46:1563-1573.

Kimes, D.S., Idso, S.B., Pinter, Jr., P.J., Reginato, R.J., and Jackson, R.D. (1980). View angle effects in the radiometric measurement of plant canopy temperatures. <u>Remote Sens. Environ.</u> 10:273-284.

Kimes, D.S. and Kirchner, J.A. (1982). Irradiance measurement errors due to the assumption of a Lambertian reference panel. <u>Remote Sensing of Environment</u> 12:141-149.

Kimes, D.S. (1983). Dynamics of directional reflectance factor distributions for vegetation canopies. <u>Appl. Optics</u> 22:1364-1372.

Kimes, D.S., Holben, B.N., Tucker, C.J., and Newcomb, W.W. (1984). Optimal directional view angles for remote sensing missions. <u>International Journal of Remote Sensing</u> 5:1-22.

Kimes, D.S. and Sellers, P.J. (1985). Inferring hemispherical reflectance of the earth's surface for global energy budgets from remotely sensed nadir or directional radiance values. <u>Remote Sensing of Environment</u> 18:205-223.

Kimes, D.S., Norman, J.M., and Walthall, C.L. (1985). Modelling the radiant transfers of sparse vegetation canopies. <u>IEEE Transactions on Geoscience and Remote Sensing</u> GE-23:695-704.

Kimes, D.S., Sellers, P.J., and Diner, D.J. (1987). Extraction of spectral hemispherical reflectance (albedo) of surfaces from nadir and directional reflectance data. <u>International Journal of Remote Sensing</u> 8:1727-1746.

Klaassen, W. and van den Berg, W. (1985). Evapotranspiration derived from satellite observed surface temperatures. <u>Journal of Climate and Applied Meteorology</u>, 24:412-424.

Klucher, T. (1979). Evaluation of models to predict insolation on tilted surfaces. <u>Solar Energy</u> 23:111-114.

Kneizys, F.X., Shettle, E.P., Gallery, W.O., Chetwynd, J.H., Abreu, L.W., Selby, J., Fenn, R., and McClatchey, R. (1980). Atmospheric transmittance/radiance: computer code Lowtran 5. AFGL-TR-80-0067 ERP 697, Air Force Cambridge Research Laboratories.

Kriebel, K.T. (1976). On the variability of the reflected radiation field due to differing distributions of the irradiation. Remote Sensing of Environment 4:257-264.

Kriebel, K.T. (1978). Measured spectral bidirectional reflectance properties of four vegetated surfaces. Appl. Optics 17:253-259.

Kriebel, K.T. (1979). Albedo of vegetated surfaces: its variability with differing irradiances. Remote Sensing of Environment 8:283-290.

Kung, E.C., Bryson, R.A., and Lenschow, D.H. (1964). Study of a continental surface albedo on the basis of flight measurements and structure of the earth's surface cover over North America. Monthly Weather Review 92:543-564.

Lillesand, T.M. and Kiefer, R.W. (1979). Remote Sensing and Image Interpretation, John Wiley and Sons: New York, New York, 612pp.

Liou, K. (1980). An Introduction to Atmospheric Radiation, Academic Press: New York, 392 pp.

Maas, S.J. and Dunlap, J.R. (1989). Reflectance, transmittance, and absorptance of light by normal, etiolated, and albino corn leaves. Agron. J. 81:105-110.

Markham, B.L., Wood, F.M., and Ahmad, S.P. (1988). Radiometric calibration of the reflective bands of NS-001 thematic mapper simulator (TMS) and modular multispectral radiometer (MMR). Presented at the 1988 SPIE Technical Symposium, April 4-8, 1988, Orlando, Florida.

Middleton, E.M., Deering, D.W., and Ahmad, S.P. (1987). Surface anisotropy and hemispheric reflectance for a semiarid ecosystem. Remote Sens. Environ. 23:193-212.

Miller, D.H. (1981). Energy at the Surface of the Earth, Academic Press: New York, 518 pp.

Mintz, Y. (1984). The sensitivity of numerically simulated climates to land-surface boundary conditions. In: J.T. Houghton (ed.), The Global Climate, Cambridge University Press: Cambridge, 233pp.

Monteith, J.L. (1961). An empirical method for estimating longwave radiation exchanges in the British Isles. Quarterly Journal of the Royal Meteorological Society 87:171-179.

154

Monteith, J.L. (1973). <u>Principles of Environmental Physics</u>. American Elsevier Publishing Company, Inc.: New York, N.Y., 241pp.

Nicodemus, F.E., Richmond, J.C., Ginsberg, I.W., and Limperis, T. (1977). <u>Geometrical Considerations and Nomenclature for Reflectance, NBS Mongraph 160</u>, National Bureau of Standards, U.S. Dept. of Commerce.

Nixon, P.R., Phinney, D.E., Arp, G.K. and Wiegand, C.L. (1974). Mapping cold-night surface temperatures of the lower Rio Grande valley. <u>Journal of the Rio Grande Valley Horticultural Society</u>, 28:86-90.

Norman, J. and Walthall, C. (1985). Analysis of an empirical model for hemispherical albedo. Final Report, NASA contract #S-19583-D.

Norman, J., Welles, J., and Walter, E. (1985). Contrasts among bidirectional reflectance of leaves, canopies, and soils. <u>IEEE Transactions on Geoscience and Remote Sensing</u> GE-23:659-667.

Otterman, J. (1974). Baring high-albedo soils by overgrazing: a hypothesized desertification mechanism. <u>Science</u> 186:531-533.

Otterman, J., Strebel, D.E., and Ranson, K.J. (1987). Inferring spectral reflectances of plant elements by simple inversion of bidirectional reflectance measurements. <u>Remote Sensing of Environment</u> 21:215-228.

Palluconi, F., Kahle, A., Hoover, G., and Conel, J. (1990). The spectral emissivity of prairie and pasture grasses at Konza Prairie, Kansas. Symposium on FIFE, American Meteorological Society, February 4-9, 1990, Anaheim, California.

Paltridge, G.W. (1970). Day-time long-wave radiation from the sky. <u>Quarterly Journal of the Royal Meteorological Society</u>, 96:645-653.

Pease, R.W., Lewis, J.E., and Outcalt, S.I. (1976). Urban terrain climatology and remote sensing. <u>Annals of the Association of American Geographers</u> 66:557-569.

Pease, R.W. and Nichols, D.A. (1976). Energy balance maps from remotely sensed imagery. <u>Photogrammetric Engineering and Remote Sensing</u> 42:1367-1373.

Pease, S.R. and Pease, R.W. (1972). Photographic films as remote sensors for measuring albedos of terrestrial surfaces. Technical Report V, U.S.G.S. Contract 14-08-0001-11914.

Perez, R., Stewart, R., Arbogast, C., Seals, R., and Scott, J. (1986). An anisotropic hourly diffuse radiation model for sloping surfaces: description, performance validation, site dependency evaluation. <u>Solar Energy</u> 36:481-497.

Pinter, P.J. and Reginato, R.J. (1982). A thermal infrared technique for monitoring cotton water stress and scheduling irrigations. <u>Transactions of the American Society of Agricultural Engineers</u> 25:1651-1655.

Pinter, P.J. (1983). Monitoring the effect of water stress on the growth of alfalfa via remotely sensed observations of canopy reflectance and temperature. <u>Sixth Conference on Biometeorology and Aerobiology, April 25, and Sixteenth Conference on Agriculture and Forest Meteorology, April 26-28</u>, Fort Collins, CO., American Meteorological Society.

Pinter, P.J., Jackson, R.D., Idso, S.B., and Reginato, R.J. (1983). Diurnal patterns of wheat spectral reflectances. <u>IEEE Transactions on Geoscience and Remote Sensing</u> GE-21:156-163.

Ranson, K.J., Daughtry, C.S.T., and Biehl, L.L. (1986). Sun angle, view angle, and background effects on spectral response of simulated Balsam fir canopies. <u>Photogrammetric Engineering and Remote Sensing</u> 52:649-658.

Rao, P.K. (1972). Remote sensing of urban "heat islands" from an environmental satellite. <u>Bulletin of the American Meteorological Society</u> 53:647-648.

Raschke, E., Vonder Haar, T., Bandeen, W., and Pasternak, M. (1973). The annual radiation balance of the earth-atmosphere system during 1969-1970 from Nimbus 3 measurements. <u>Journal of the Atmospheric Sciences</u> 30:341-364.

Reginato, R.J. and Howe, J. (1985). Irrigation scheduling using crop indicators. <u>Journal of Irrigation and Drainage Engineering</u> 111:125-133.

Reginato, R.J., Jackson, R.D., and Pinter, P.J. (1985). Evapo-transpiration calculated from remote multispectral and ground station meteorological data. <u>Remote Sensing of Environment</u> 18:75-89.

Robinove, C.J., Chavez, P.S., Gehring, D., and Holmgren, R. (1981). Arid land monitoring using Landsat albedo difference images. <u>Remote Sensing of Environment</u> 11:133-156.

Robinson, B.F. and Biehl, L.L. (1979). Calibration procedures for measurement of reflectance factor in remote sensing field research. <u>SPIE</u> 196:16-26.

156

Robinson, B.F., Buckley, R.E., and Burgess, J.A. (1982). Performance evaluation and calibration of a modular multiband radiometer for remote sensing field research. _Agristars Technical Report SR-P2-04318_, Purdue University, Laboratory for Applications of Remote Sensing, West Lafayette, IN.

Robinson, G.D. (1950). Notes on the measurement and estimation of atmospheric radiation--2. _Quarterly Journal of the Royal Meteorological Society_ 76:37-51.

Rosenberg, N., Blad, B., and Verma, S. (1983). _Microclimate: The Biological Environment_, John Wiley and Sons: New York, New York, 495pp.

Ross, J.K. and Marshak, A.L. (1988). Calculation of canopy bidirectional reflectance using the Monte Carlo method. _Remote Sensing of Environment_ 24:213-225.

Salomonson, V.V. and Marlatt, W.E. (1971). Airborne measurements of reflected solar radiation. _Remote Sens. Environ._ 2:1-8.

Satterlund, D.R. (1979). An improved equation for estimating longwave radiation from the atmosphere. _Water Resources Research_ 15:1649-1650.

Saunders, R. and Hunt, G. (1980). METEOSAT observations of diurnal variation of radiation budget parameters. _Nature_ 283:645-647.

Sellers, P.J. and Hall, F.G. (1987). FIFE Experiment Plan. NASA Goddard Space Flight Center, Greenbelt, Maryland, 157 pp.

Sellers, P., Hall, F., Asrar, G., Strebel, D., and Murphy, R. (1988). The first ISLSCP field experiment (FIFE). _Bulletin of the American Meteorological Society_ 69:22-27.

Sellers, W.D. (1965). _Physical Climatology_, University of Chicago Press: Chicago.

Skartveit, A. and Olseth, J. (1986). Modelling slope irradiance at high latitudes. _Solar Energy_ 36:333-344.

Slater, P.N. (1980). _Remote Sensing: Optics and Optical Systems_. Addison-Wesley Publishing Company: Reading, Mass., 575pp.

Slater, P.N. and Jackson, R.D. (1982). Atmospheric effects on radiation reflected from soil and vegetation as measured by orbital sensors using various scanning directions. _Applied Optics_ 21:3923-3931.

Smith, J.A., Lin, T.L., and Ranson, K.J. (1980). The Lambertian assumption and Landsat data. _Photogrammetric Engineering and Remote Sensing_ 46:1183-1189.

Smith, W., Hickey, H., Howell, H., Jacobowitz, H., Hilleary, D., and Drummond, A. (1977). Nimbus-6 earth radiation budget experiment. _Applied Optics_ 16:306-318.

Soer, G.J.R. (1980). Estimation of regional evapotranspiration and soil moisture conditions using remotely sensed crop surface temperatures. _Remote Sensing of Environment_ 9:27-45.

Stoll, A.M. and Hardy, J.D. (1955). Thermal radiation measurements in summer and winter Alaskan climates. _EOS Transactions of the American Geophysical Union_ 36:213- 225.

Suits, G.H. (1972). The calculation of the directional reflectance of a vegetative canopy. _Remote Sensing of Environment_ 2:117-125.

Sutton, O.G. (1953). _Micrometeorology_, McGraw-Hill Book Company, Inc.: New York, New York.

Swain, P.H. and Davis, S.M. (1978). _Remote Sensing: The Quantitative Approach_. McGraw-Hill Book Company: New York, New York.

Swinbank, W.C. (1963). Long-wave radiation from clear skies. _Quarterly Journal of the Royal Meteorological Society_ 89:339-348.

Tarpley, J. (1979). Estimating incident solar radiation at the surface from geostationary satellite data. _Journal of Applied Meteorology_ 18:1172-1181.

Temps, R. and Coulson, K. (1977). Solar radiation incident upon slopes of different orientations. _Solar Energy_ 19:179-184.

Vonder Haar, T. and Suomi, V. (1971). Measurements of the earth's radiation budget from satellites during a five-year period. Part I: Extended time and space means. _Journal of the Atmospheric Sciences_ 28:305-314.

Walsh, S.J. and Stadler, S.J. (1983). Regional evapotranspiration modeling of Oklahoma's Little Washita drainage basin. _Machine Processing of Remotely Sensed Data_, Purdue University Laboratory for Applied Remote Sensing.

Walter-Shea, E.A., Blad, B.L., Starks, P.J., and Norman, J.M. (1988). Leaf reflectance and transmittance of prairie vegetation in selected visible and infrared wavebands. _Agron. Abstracts_, pg. 29.

Walter-Shea, E.A., Norman, J.M., and Blad, B.L. (1989). Leaf bidirectional reflectance and transmittance in corn and soybean. _Remote Sens. Environ._ 29:161-174.

Walter-Shea, E.A., Norman, J.M., Blad, B.L., and Robinson, B.F. (1990a). Leaf reflectance and transmittance in soybean and corn. <u>Agron. J.</u> 82: (in press).

Walter-Shea, E.A., Blad, B.L., Starks, P.J., Hays, C.J., Mesarch, M.A., and Middleton, E.M. (1990). <u>Proceedings of Symposium on FIFE</u>. American Meteorological Society, Anaheim, CA. pg. 70.

Walthall, C.L., Norman, J.M., Welles, J.M., Campbell, G., and Blad, B.L. (1985). Simple equation to approximate the bidirectional reflectance from vegetative canopies and bare soil surfaces. <u>Applied Optics</u> 24:383-387.

Wiegand, C.L. and Bartholic, J.F. (1970). Remote sending in evapo-transpiration research on the Great Plains. Evapotrans-piration in the Great Plains Research Committee. <u>Great Plains Agricultural Council Publication</u> 50:137-180.

Willmott, C.J. and Wicks, D.E. (1980). An empirical method for the spatial interpolation of monthly precipitation within California. <u>Physical Geographer</u> 1:59-73.

Willmott, C.J. (1981). On the validation of models. <u>Physical Geographer</u> 2:184-194.

Willmott, C.J. (1982). Some comments on the evaluation of model performance. <u>Bulletin of the American of the Meteorological Society</u>. 63:1309-1313.

Woolley, J.T. (1971). Reflectance and transmittance of light by leaves. <u>Plant Physiol.</u> 47:656-662.

Yeates, M. (1974). <u>An Introduction to Quantitative Analysis in Human Geography</u>, McGraw-Hill: New York, 300 pp.